

Anomalous relaxation in colloidal systems

by

Avinash Kumar

BS-MS, Indian Institute of Science Education and Research Kolkata, 2015

Thesis Submitted in Partial Fulfillment of the
Requirements for the Degree of
Doctor of Philosophy

in the
Department of Physics
Faculty of Science

© **Avinash Kumar 2021**
SIMON FRASER UNIVERSITY
Spring 2021

Copyright in this work is held by the author. Please ensure that any reproduction or re-use is done in accordance with the relevant national copyright legislation.

Declaration of Committee

Name: Avinash Kumar
Degree: Doctor of Philosophy
Thesis title: Anomalous relaxation in colloidal systems
Committee: **Chair:** Malcolm Kennett
Associate Professor, Physics

John Bechhoefer
Supervisor
Professor, Physics

David Sivak
Committee Member
Associate Professor, Physics

Nancy Forde
Committee Member
Professor, Physics

Steven Dodge
Examiner
Associate Professor, Physics

Marija Vucelja
External Examiner
Assistant Professor
Department of Physics, University of Virginia

Abstract

The *Mpemba effect* refers to a phenomenon where a sample of hot water may cool and begin to freeze more quickly than a cool or warm water sample prepared under identical conditions. Although the effect has been known since the time of Aristotle, it is named after the Tanzanian teenager Erasto Mpemba, who discovered the effect in the 1960s. Although Mpemba and Osborne showed the effect in laboratory experiments, it has always been mysterious, its underlying mechanism a topic of hot debate.

In this thesis, we experimentally show the Mpemba effect in a colloidal system with a micron-sized silica bead diffusing in a bath. The bead is subjected to an external double-well potential created by a feedback-based optical tweezer. When a system is quenched from an initially hot equilibrium state to a cold equilibrium state, the evolution of the system between the initial and the final state is a strongly nonequilibrium process. As a nonequilibrium state cannot, in general, be characterized by a single temperature, we adopt the notion of a “distance” measure as a proxy for temperature. We show Mpemba effects in an asymmetric double-well potential. Our experimental results agree quantitatively with predictions based on the Fokker-Planck equation. Using understanding gained from the Mpemba effect, we design an experiment to investigate the opposite effect and present the first experimental evidence for this *inverse* Mpemba effect. Contrary to the cooling effect, the inverse effect is related to a phenomenon where a system that is initially cold heats up faster than an initially warm system. By understanding the underlying mechanism of these anomalous effects, we demonstrate strong Mpemba and inverse Mpemba effects, where a system can cool or heat exponentially faster to the bath temperature than under typical conditions. Finally, we ask whether asymmetry in the potential is necessary and show experimentally that an anomalous cooling effect can be observed in a *symmetric* potential, leading to a higher-order Mpemba effect.

Keywords: Mpemba effect; inverse Mpemba effect; Fokker-Planck equation; thermal relaxation; metastability; free-energy landscape; nonequilibrium; feedback traps; optical tweezers; virtual potentials

Acknowledgements

The last five years have been a long journey. It was full of challenges, excitement, and fun. I am grateful to the wonderful people I have interacted with during these years. Here, I give an incomplete list of people without whom my Ph.D. journey would have been impossible.

First of all, I would like to thank my adviser Dr. John Bechhoefer for providing me the opportunity to work in his group. John is a fantastic supervisor in many ways. He is a perfect mentor for training young minds. His way of perceiving a problem and framing it in a big picture has always amazed me. He is always enthusiastic about new ideas and helps put them in a broader context with immense encouragement and, of course, with criticism. Throughout my Ph.D., he was very supportive in all kinds of situations. I owe it all to him.

I thank other supervisory committee members, Dr. David Sivak and Dr. Nancy Forde, who always gave me valuable feedback and ideas for my research in the committee meetings. My special thanks to Nancy Forde, who entertained my unscheduled visits to her office and advised me when I faced technical issues in my experiments.

I thank David Lee for lending me an uncountable amount of optical components from his lab whenever I needed them. He is always there to help people as an all-rounder. While setting up my experiment, I used the machine shop a lot. I thank Bryan Gormann, Kenneth Myrtle, and Chang Min Kim for training me to build parts independently. I also thank James Lang for providing IT support.

I extend my gratitude to the members in John's lab who overlapped with me at different parts of the journey. I want to thank Momčilo, Matse, Emma, Lisa, Jomar, Matthias, Tushar, Ronja, Xiao-Yi, Denesh, Wen-dong, Luis, Prithviraj, Karel, and Jannik. I extend special thanks to Dr. Raphaël Chérite for his valuable help and discussions in developing the theory of the Mpemba effect. Outside the lab, I often spent many hours bugging Lavisha and Sujit for silly theoretical questions. Thank you!

I also appreciate the assistance from staff members of the physics department: Rose, Ayako, Maegan, Ben, and Eva. I thank the Department of Physics for giving me several scholarships, including Billy Jones Grad award, Graduate Entrance scholarship, and travel awards.

I convey my utmost regards to my family, who were the constant support throughout my life. Lastly, I thank my girlfriend, Rima Majumdar, who had been extremely patient and understanding, even in a long-distance relationship.

Table of Contents

Declaration of Committee	ii
Abstract	iii
Acknowledgements	iv
Table of Contents	v
List of Tables	viii
List of Figures	ix
1 Introduction	1
1.1 Relaxation in physical systems	1
1.2 History of the Mpemba effect	2
1.3 Explanations for the Mpemba effect	3
1.4 Mpemba effect in other systems	6
1.4.1 Experiments	6
1.4.2 Numerical studies	8
1.5 Mpemba effect in colloidal systems	10
1.6 Particle manipulation techniques	11
1.6.1 Passive trapping	11
1.6.2 Active trapping	15
1.7 Combining feedback traps and optical tweezers	20
1.8 Overview of the thesis	20
2 Particle dynamics	22
2.1 The Langevin equation	22
2.1.1 A free particle	22
2.1.2 A trapped particle	23
2.2 Fokker-Planck equation	25
2.2.1 Adjoint of the Fokker-Planck operator	27
2.2.2 Eigenfunctions and eigenvalues of the Fokker-Planck operator	28

2.2.3	Fokker-Planck equation with no drift	29
2.3	Heat equation	30
2.4	Supplemental information	33
2.4.1	A Similarity transformation of the Fokker-Planck operator	33
3	Optical Feedback traps	37
3.1	Feedback traps	37
3.2	Principles of optical tweezers	38
3.3	Optical tweezers setup	41
3.3.1	Faraday isolator	43
3.3.2	Acousto-optic deflector	44
3.3.3	Detection scheme	46
3.3.4	Control and data acquisition	47
3.4	Sample preparation	48
3.5	Calibration	48
3.5.1	Position calibration	49
3.5.2	Trap-stiffness calibration	51
3.6	Virtual harmonic potential	55
3.7	Isotropic traps	56
3.8	Virtual double-well potential	57
3.9	Discussion	60
4	Mpemba effect	62
4.1	Definition of the Mpemba effect	62
4.2	Energy landscape for the Mpemba effect	63
4.2.1	Choice of potential energy landscape	64
4.3	Imposing an instantaneous quench via initial conditions	66
4.4	Measuring the distance to equilibrium	67
4.4.1	L_1 distance	69
4.4.2	Kullback-Leibler (KL) divergence.	70
4.5	Observation of the Mpemba effect in asymmetric domains	72
4.6	Analysis based on eigenfunction expansion	73
4.6.1	Calculation of the a_2 coefficient	75
4.6.2	Relationship between $\Delta\mathcal{D}$ and the a_2 coefficient	76
4.7	Strong Mpemba effect	77
4.8	Geometric interpretation of the Mpemba effect	80
4.8.1	Thermalization in a double-well potential with metastability	80
4.8.2	Metastable Mpemba effect	82
4.8.3	Metastable Mpemba effect in terms of extractable work	85
4.9	Discussion	87

4.10	Supplementary information	88
4.10.1	Infinite potential vs. finite potential	88
4.10.2	Calculation of equilibration time	89
4.10.3	Equilibration time versus the a_2 coefficient	90
4.10.4	Barrier height vs. discontinuity in local equilibrium	91
5	Inverse Mpemba effect	92
5.1	Energy landscape for the inverse Mpemba effect	93
5.2	Inverse Mpemba effect in an asymmetric potential	94
5.3	Analysis based on eigenfunction expansion	96
5.4	Discussion	99
6	Higher-order Mpemba effect	101
6.1	Experiment	101
6.2	Eigenfunction analysis	103
6.3	Mpemba effect in a potential with one local minimum	104
6.4	Discussion	105
7	Conclusions	106
7.1	Summary of the results obtained	106
7.2	Final remarks	108
	Bibliography	110

List of Tables

Table 5.1	Comparison between the Leidenfrost and inverse Mpemba effects. . .	93
-----------	--	----

List of Figures

Figure 1.1	Energy landscape for the Mpemba effect	10
Figure 1.2	Working principle of optical tweezers	12
Figure 1.3	Working principle of magnetic tweezers	13
Figure 1.4	Working principle of holographic optical tweezers	14
Figure 1.5	Working principle of electrokinetic tweezers	16
Figure 1.6	Working principle of hydrodynamic tweezers	17
Figure 1.7	Working principle of acoustic tweezers	18
Figure 1.8	Working principle of thermal tweezers	19
Figure 2.1	Heat transfer in a one-dimensional thin rod	30
Figure 3.1	One cycle of the feedback trap	38
Figure 3.2	Working principle of optical tweezers based on ray optics	39
Figure 3.3	Schematic diagram of the feedback-trap setup	42
Figure 3.4	Schematic diagram of the Faraday isolator	44
Figure 3.5	Schematic diagram of an acousto-optic deflector	45
Figure 3.6	Diffraction efficiency of the acousto-optic deflector	46
Figure 3.7	Interferometry-based detection scheme	47
Figure 3.8	Schematic of the sample chamber	49
Figure 3.9	Calibration of the AOD	50
Figure 3.10	Calibration of the QPD signals	50
Figure 3.11	Expected displacement vs. measured displacement	51
Figure 3.12	Calibration of trap stiffness	53
Figure 3.13	Potential and equipartition analysis	54
Figure 3.14	PSD for different values of proportional feedback gain.	56
Figure 3.15	Power spectrum density of the isotropic trap	57
Figure 3.16	Virtual double-well potentials	59
Figure 3.17	Virtual double-well potential with wells separated by ≈ 10 nm . . .	59
Figure 4.1	Energy landscape and Boltzmann distribution for the Mpemba effect	63
Figure 4.2	Schematic of potential energy landscape	65
Figure 4.3	Cumulative probability distribution at the bath temperature	67
Figure 4.4	Dynamics of system relaxation to equilibrium	68

Figure 4.5	L_1 distance shows the Mpemba effect	71
Figure 4.6	KL divergence shows the Mpemba effect	72
Figure 4.7	Equilibration time as a function of initial system temperature . . .	73
Figure 4.8	Controlling relaxation times	74
Figure 4.9	Eigenfunctions of the FP operator	76
Figure 4.10	Measurements of $\Delta\mathcal{D}$ at fixed α	78
Figure 4.11	Measurements of $\Delta\mathcal{D}$ at fixed initial temperatures	79
Figure 4.12	Two-stage dynamics in a tilted double-well potential	81
Figure 4.13	Dynamics of a_2 , a_3 , and a_4 coefficients	83
Figure 4.14	Extractable work as a function of initial temperature	87
Figure 4.15	Finite maximum slope of the bath potential and the Mpemba effect	88
Figure 4.16	Different noise levels do not affect the difference in equilibration time	90
Figure 5.1	Energy landscape of the inverse Mpemba effect	94
Figure 5.2	Dynamic trajectories relaxing to equilibrium at a hot temperature .	95
Figure 5.3	Measurements of t_{eq} and $\Delta\mathcal{D}$ in a bath at finite temperature	96
Figure 5.4	Equilibration time and $\mathcal{D}(t)$ for the inverse Mpemba effect	97
Figure 5.5	Eigenfunction for the FP operator for a flat potential	98
Figure 5.6	Measurements of $\Delta\mathcal{D}$ for a bath at an effectively infinite temperature	98
Figure 5.7	Ratio Λ of eigenvalues λ_3 to λ_2 of the FP operator as a function of E_b	100
Figure 6.1	Schematic of the energy landscape for the higher-order Mpemba effect	102
Figure 6.2	Equilibration in a symmetric potential.	102
Figure 6.3	Eigenfunctions of the FP operator for a symmetric potential	103
Figure 6.4	Relaxation in a symmetric potential	104
Figure 6.5	Mpemba effect in a potential with one local minimum	105

Chapter 1

Introduction

1.1 Relaxation in physical systems

When a system is perturbed, it tends to relax back to equilibrium. The simplest theoretical description of relaxation as a function of time t after a perturbation is an exponential law $\propto \exp(-t/\tau)$ with a characteristic time τ . Indeed, the decaying motion of damped harmonic oscillators, thermal relaxation of a typical body to its ambient temperature, and discharging of a capacitor all exhibit exponential relaxation, with decay rates independent of the time at which the systems are perturbed from equilibrium.

However, in many cases, the relaxation of systems is far from exponential and may depend on their history of perturbation [1]. The dynamics of disordered systems, starting from an initial perturbed state towards its equilibrium, can often be slow and involve a number of different relaxation mechanisms in parallel. For example, logarithmic relaxation has been experimentally observed in compaction of sand in a tube [2], the current decay in superconductors [3], volume relaxation in crumpling paper [4], mechanical relaxation of plant roots [5], and frictional strength [6]. In solid-state physics, *glassy* systems show extremely slow dynamics below and just above the glass transition. In a variety of systems, at short times (less than the time t_w during which an external force has been applied), the relaxation dynamics are logarithmic ($\propto \ln(t_w/t)$), whereas a power-law ($\propto t_w/t$) is observed at long times [7]. These relaxations are much slower than exponential or stretched exponential decay, and their equilibration times are often experimentally unreachable. Similar to glasses, proteins display a slow relaxation process best described by a stretched exponential when perturbed by temperature and pressure [8]. Stretched exponential behaviors are also observed in systems such as molecular and electronic glasses [9], metallic glass-forming melts [10], and granular systems [11]. The relaxation dynamics governed by these laws are anomalously slow and can take longer than usual to relax. Generally, when such systems are perturbed, relaxation to equilibrium involves the relaxation of a spectrum of modes. Each of the modes relaxes independently and exponentially to its equilibrium, but with a

different relaxation rate. In some cases, some of these modes may get trapped in metastable states and relax with long equilibration times.

Although the best-known relaxation anomalies involve very slow relaxations, there is another class where relaxation can be much faster than expected. The best-known of these investigations concerns an anomalous cooling effect in water, known as the *Mpemba effect* [12]. Under certain conditions, an initially hot sample of water can freeze faster than an initially warm sample of water. The effect may appear counterintuitive, as our intuitions are set by systems that remain at or near equilibrium; in that case, a system starting at a higher temperature cannot reach equilibrium without passing through all the intermediate temperatures. However, in a thermal quench, systems do not remain in equilibrium. Thus, the state of the system at any instant is not described by a single temperature. A large temperature gradient can be set up by convective currents within the volume and may be represented by a temperature field $T(\mathbf{x}, t)$. One can calculate the spatial average of $T(\mathbf{x}, t)$ as the water cools, but the average temperature does not represent the water that had been initially prepared at the same temperature. Thus, the system does not necessarily have to pass through all the intermediate states to reach equilibrium and can sometimes cool faster. After their discovery in water, these anomalous cooling effects were observed in other physical systems, suggesting that such behavior may be a general phenomenon in nature.

1.2 History of the Mpemba effect

In 1963, a Tanzanian boy, Erasto Mpemba, made an accidental discovery that a container of hot water could cool faster than a container of warm water when placed in the same environment. When he was in Form 3 in Magamba Secondary School, Tanzania, he made ice cream with his fellow students. While he was boiling the milk, another student mixed his milk with sugar and poured it into the ice tray without boiling it. The fear of losing the last available ice tray led Mpemba to decide to risk ruining the refrigerator by putting hot milk into its freezer. After an hour and a half, he and his friend found that the boiled milk had frozen into ice cream while the cold milk was still a thick liquid. He was ridiculed by his physics teacher when he asked about his observation. Later he asked the same question to Dr. Denis G. Osborne, who assured him that he would redo the experiment at his university. When his technician found that Mpemba was correct, they ran more experiments and published the first systematic study of the effect in 1969 [12]. They argued that the hot liquid's top surface cooled rapidly due to convection, leading to faster cooling of the hot liquid. We will discuss this and other mechanisms for the Mpemba effect below, in Sec. 1.3.

Although the current interest in understanding the Mpemba effect gained momentum after Mpemba's discovery, its history stretches back 2300 years. Around 350 B.C., Aristotle wrote, "if water has been previously heated, this contributes to the rapidity with which it

freezes: for it cools more quickly [13, 14].” The effect was also discussed by Roger Bacon in the 13th century [15], Giovanni Marliani in the 15th century [16], Francis Bacon [17] and Descartes in the 17th century. These historical discussions provide evidence that people were aware of the effect, but no explanations were given to support the observation. At present, many explanations have been proposed for the effect, but none has been generally accepted. We will discuss recent progress in the next section.

1.3 Explanations for the Mpemba effect

Mpemba explained his observation about hot water freezing faster than cold water as arising from thermal convection. The rapid mixing of liquid in a hot sample of water led to a faster cooling from the liquid’s top surface, and thus a faster cooling overall. However, this is not the only possible mechanism. The effect was reproduced when the system was subjected to variations in parameters that control the heat transfer rate. Possible mechanisms for the Mpemba effect include

- *Evaporation:* If equal masses of water are taken at two starting temperatures, more rapid evaporation from the hotter one may diminish its mass enough to compensate for the greater temperature range it must cover to reach freezing. Kell, in 1968, argued that mass loss due to evaporation could explain the Mpemba effect [18]. Advancing Kell’s work, Vynnycky et al. modeled more precise geometry in which the experiment was carried out to understand the potential role of evaporative cooling [19]. A recent numerical study considered evaporation, radiation, and convection in a single droplet of water and suggested that evaporation is the main reason behind the effect [20]. However, other observations indicate that the amount of water lost to evaporation is insufficient to produce the effect and might be simply a contributory factor [12, 21, 22]. In particular, Wojciechowski et al. observed the effect in a closed container, where evaporation was reduced [23].
- *Convection:* As the water cools, temperature gradients and convection currents develop. For most temperatures, the water density decreases as the temperature is increased, creating a “hot top” [24], where the top surface is warmer than the average temperature of the water. Because the rate of cooling depends on the surface temperature of the liquid and not on its mean temperature, the heat loss is greater for the more inhomogeneous temperature distribution. Since a strong convective flow is created in initially hot water, it cools faster than initially warm water. The temperature gradient set by convection also suggests that the initially hot system never passes through a state equivalent to the starting point for the cooling of the initially warm system [22].

Although a hot water sample initially cools faster, it does not necessarily freeze first [21]. Vynnycky et al. did not observe the Mpemba effect while considering natural convection alone, both experimentally and theoretically [25]. However, they suggested that the large deviation in the measured freezing times of systems from theoretical predictions at a given temperature could allow the Mpemba effect to be observed. They concluded that although the general timescale for freezing is determined by natural convection, the actual time period is adjusted by supercooling.

- *Supercooling:* Supercooling occurs when water remains in the liquid phase below its melting temperature. For situations where initially hot water supercools less, it may freeze faster than initially warm water. Auerbach observed that hot water spontaneously froze faster with probability 0.53 (19 times out of 36 runs) and 0.24 (7 times out of 29 runs) when the ambient temperature T_a was $-8\text{ }^{\circ}\text{C} < T_a < -5\text{ }^{\circ}\text{C}$ and $-11\text{ }^{\circ}\text{C} < T_a < -8\text{ }^{\circ}\text{C}$, respectively [26]. He pointed out that the initially hotter water should have a greater temperature gradient and that a gradient is known to trigger crystallization. However, the argument connecting temperature gradient and rapid crystallization contradicted his experimental results. Jeng noted that the low probability of finding the Mpemba effect and the limited number of trials in Auerbach’s experiments could explain the results by statistical coincidence [14]. Esposito et al. pointed out that the statistical nature of the Mpemba effect can be explained in terms of the transition between differently ordered phases in water and supercooling [27]. When a liquid is cooled below $0\text{ }^{\circ}\text{C}$, supercooling is followed by nucleation. To initiate the ice formation, some liquid molecules should arrange in a well-defined order to form a minimum crystal (or nucleus). Nucleation and crystal growth processes are both favored below $0\text{ }^{\circ}\text{C}$, and their onset time is stochastic.
- *Dissolved gases:* Warm water contains more dissolved gases than hot water. In an attempt to argue that degassing leads to quicker freezing, Wojciechowski et al. noted that water molecules surrounding solute gas molecules are more ordered than elsewhere in the liquid [23]. Thus, the dissolved gas molecules significantly increase the viscosity of the water and inhibit convective heat transport during the cooling process. Contrary to Deeson [24], Freeman also observed that the increased amount of CO_2 in warm water results in slow cooling [21]. Nonetheless, Osborne disagreed with the hypothesis by saying that the faster cooling in Mpemba’s experiment was achieved with recently heated water for both hot and warm systems, and the effect of dissolved CO_2 may be similar to the lost water mass through evaporation. Brownridge also did not find any correlation between the amounts of dissolved CO_2 and the cooling rate or the time to freeze [28].
- *Hydrogen bonds:* Molecular-dynamics studies of water molecules have shown the significance of the hydrogen bond (H-bond) interaction for understanding the atomistic

behavior of water exhibiting the Mpemba effect. Zhang et al. proposed that the relaxation dynamics of the hydrogen bond (O:H–O) plays a primary role in heat conduction [29]. Unlike other materials that lengthen and soften when they absorb energy, water behaves abnormally under heating, lengthening the O:H bond and shortening the H–O covalent bond through inter-oxygen Coulomb coupling between electron pairs on adjacent oxygen ions [30]. This process turns the skin of water (a monolayer at water-air interface) into a “supersolid” phase, where the water molecules form a rigid, ordered structure and flow with zero viscosity [31, 32]. Zhang et al. argued that skin-supersolidity is necessary to understand thermal-fluid transport in liquid water. Thus, in their model, they partitioned a one-dimensional tube cell containing water into a *bulk* region and a *skin* region to study thermal relaxation. They observed the Mpemba-like cooling only when the thermal diffusivity α_S of the skin was greater than the thermal diffusivity α_B of the bulk. Based on their numerical results, they also observed that the liquid temperature decayed exponentially with cooling time with a relaxation time τ_r that decreased exponentially with the increase of the initial temperature or the initial energy storage of the liquid.

Tao et al. [33] modeled liquid water as a cluster of 1000 water molecules and observed that increasing the temperature from 283 to 363 K leads to a decrease in the average number of H-bonds per water molecule. They proposed that the weaker H-bonds with predominantly electrostatic contributions were broken in hot water, and smaller water clusters with strong H-bonding arrangements existed that accelerated the nucleation process leading to a hexagonal lattice of solid ice. In contrast, the weaker hydrogen bonds in warm water constantly reshuffle during cooling until there is insufficient thermal energy to overcome their movement. Therefore, hot water freezes faster than warm water in which the transformation from randomly arranged water clusters to solid structure of ice costs time and energy.

- *Dissolved solutes:* The Mpemba effect can arise from the freezing-point depression induced by solutes such as calcium or magnesium carbonates, whose solubility decreases with increasing temperature [34]. Such solutes precipitate out in the pre-heated water¹ and do not lower the freezing point as much as they would do in never-heated water. Besides, lowering the freezing point reduces the temperature difference between the liquid and the subfreezing environment. Hence, the never-heated water starts to freeze later.

¹Hard water mostly contains $\text{Ca}(\text{HCO}_3)_2$ introduced by the reaction between atmospheric carbon dioxide and limestone rock: $\text{CaCO}_3 + \text{CO}_2 + \text{H}_2\text{O} \longleftrightarrow \text{Ca}(\text{HCO}_3)_2$. Since the solubility of gases in liquids decreases rapidly with increasing temperature, heating removes the dissolved CO_2 from water. As a consequence, the depletion of CO_2 favors the backward reaction to compensate for the change in concentration of CO_2 obeying Le Chatelier’s principle and results in the precipitation of limestone, CaCO_3 [34].

- *Environment:* The cooling rate is influenced by the surrounding environment of the experiment. Several factors such as frost, thermal conductivity, and cooling chamber can affect the heat transfer between two bodies. For example, if water containers sit on a layer of frost that conducts heat poorly, the hot sample would melt the layer establishing a better thermal contact with the refrigerator floor. However, Mpemba's experiment was done with an insulated layer of styrofoam between the container and the refrigerator surface. To study the effect of air circulation on the cooling rates, Firth measured the freezing time of water samples initially in the temperature range 273–363 K [35]. He observed that the freezing time was maximum at 323 K when cooled in a domestic refrigerator instead of 363 K in a minifridge, the latter being four times smaller in size than the former².

1.4 Mpemba effect in other systems

Although mainly observed in water, the Mpemba effect has been observed in other systems. In this section, we summarize observations of the Mpemba effect in both experimental systems and numerical simulations.

1.4.1 Experiments

- *Magnetoresistance manganites:* Chaddah et al. observed the Mpemba effect in half-doped manganites $\text{La}_{0.5}\text{Ca}_{0.5}\text{MnO}_3$ cooling in a magnetic field [36]. Generally, during the cooling of a manganite in a magnetic field, both equilibrium (antiferromagnetic) and kinetically arrested nonequilibrium (ferromagnetic) phases coexist. The fraction of the nonequilibrium state f_{NE} is a measure of how much a system is initially arrested in a metastable nonequilibrium state. Chaddah et al. observed that a state with initially higher magnetization M (and thus farther from equilibrium) overtakes a state with initially lower M as they approach equilibrium ($f_{\text{NE}} = M = 0$). While warming, they measured the nucleation time for the system, starting at different M values at a chosen measurement field, which dictates the nucleation size. They observed that when nucleation starts at a lower temperature, the regions of the antiferromagnetic phase have a large number of smaller nuclei with radii R_C , where $R_C = 2\sigma/\Delta f$ is the critical radius for the nuclei formation with σ the surface tension and Δf the difference in the bulk free energies of the antiferromagnetic and ferromagnetic phases [37]. A lower R_C is observed when the initial f_{NE} is higher. The authors argued that since a state with high f_{NE} has many smaller nuclei and a higher interface area, a

²The cooling time of a water sample is affected by air convection currents induced inside the cooling environment. These currents can persist for much longer in a large domestic refrigerator than a small minifridge.

higher isothermal relaxation rate will be observed than the relaxation rate observed in a lower magnetization state.

- *Clathrate hydrate:* Ahn et al. observed the Mpemba effect experimentally in clathrate hydrates consisting of hydrogen-bonded water frameworks and enclathrated tetrahydrofuran (THF) molecules [38]. They observed that THF solutions display Mpemba-like behavior in the temperature range 278–318 K, where warmer solutions form hydrates faster than colder solutions. At an initial temperature above 318 K, the formation time was delayed as some THF molecules in gas form at high temperature must liquefy before they can form hydrates. They defined the freezing temperature as the temperature at which the THF solution structurally transforms into THF hydrates. They then measured the average freezing time of water and observed a non-monotonic, quadratic dependence on the initial temperature of the solution. Further, Ahn et al. studied the cooperative relationship between the intramolecular polar-covalent bonds (O–H) and intermolecular hydrogen bonds (O:H) for the THF system. Using Raman spectra, they observed that O:H stretching phonons of water in THF showed a blue shift, and O–H stretching mode showed a redshift. The fact that such cooperative relationships of the two bonds are also found in water may be the leading cause of the Mpemba-like behavior in forming the THF hydrate [29].
- *Polymers:* Hu et al. studied crystallization in polylactide (PLA), an environmentally friendly polymer produced from renewable resources [39]. Generally, cold polymers crystallize faster than hot polymers due to self-nucleation (production of self-seeds or self-nuclei within a polymer melt) originating from the residual orientation of the chains that are inside the crystal [40]. However, quenched PLA crystallizes faster when initially held at a higher temperature (T_h) and annealed isothermally at a lower temperature. The unusual Mpemba effect in PLA crystallization may arise from the microscopic differences produced during sample preparation. Hu et al. argued that the size of these local structures is large at higher T_h , and thus the PLA chain mobility increases with T_h . Thus, during the crystallization process, the local structures with larger sizes have better mobility and complete the adjustments or corrections of PLA chain conformations. On the contrary, local structures with smaller sizes developed at low T_h diffuse less that, in return, delays the chain adjustment process, leading to a Mpemba-like behavior during the formation of crystals.
- *Water in rough-walled container:* A recent experiment by Hallstadius, a high-school student in Sweden, in collaboration with Burrridge, indicates that hot water can super-cool less if the number of nucleation sites within the cooling environment is increased [41]. In their case, they increased the number of nucleation sites by roughening the container walls. For sample preparation, they chose three identical plastic beakers

with reasonably smooth interior walls. The inside of one of the beakers was roughened with sandpaper, while the other two were roughened on the outside, making sure that the mass of the three remained identical after roughening. For a pair of beakers with smooth insides, they observed normal cooling. However, for a beaker with rough inside, the freezing occurred faster than the water in an identical beaker with smooth insides. They concluded that increased nucleation sites reduced the occurrence of supercooling by the formation of ice crystals.

1.4.2 Numerical studies

- *Carbon nanotube resonators:* Greaney et al. observed an anomalous and transient process of intrinsic dissipation in simulations of the ring-down of flexural modes in single-walled carbon nanotube (CNT) resonators [42]. An anti-correlation observed between the excitation energy in the resonator and the decay time of the excited modes is similar to the Mpemba effect. The anomalous dissipation is understood by examining how the dissipated energy from the flexural modes is distributed into the background modes of the tube. The authors developed a phenomenological model that divided the background modes into two classes: (i) low-frequency background modes, which interacted strongly with the flexural modes, and (ii) weakly interacting high-frequency modes [42]. The model could predict the simulated CNT ring-down data qualitatively but could not capture the expected attenuation profile. Nonetheless, the study did emphasize that the origin of the anomalous dissipation is the internal degrees of freedom, which are not in equilibrium and have different effective temperatures.
- *Granular fluids:* Lasanta et al. studied the Mpemba effect in granular fluids in settings that did not involve a phase transition [43]. Contrary to a hard-spheres fluid where energy and momentum are conserved, a granular fluid is a set of microscopic particles with inelastic collisions that do not preserve energy and is intrinsically an out-of-equilibrium system. They showed that the Mpemba effect results from the coupling of the granular temperature and the kurtosis, which measures the lowest-order deviation of the velocity distribution function from the Maxwellian shape. Initially, they studied the granular fluid of smooth, hard spheres where the kurtosis is small. The non-Gaussianities of the time evolution of temperature lead to not only the Mpemba effect but also predict an *inverse* Mpemba effect, where an initially cooler system heats faster. However, the smallness of the kurtosis limits the magnitude of these effects, both in the homogeneously heated and freely cooled systems. By contrast, Torrente et al. observed a giant Mpemba effect in a uniformly heated gas of inelastic rough hard spheres where a sample with its initial temperature higher by more than one order of magnitude compared to another sample can cool faster. [44]. Unlike the case of smooth, hard spheres, rough spheres have a strong coupling between the translational

and rotational degrees of freedom. Their study showed that the initially hotter system must have its kinetic energy more concentrated in the translational modes than the initially cooler one to facilitate the Mpemba effect.

- *Spin glasses:* Baity-Jesi et al. studied the nonequilibrium memory effect, encoded in the glassy coherence length, responsible for the Mpemba effect in spin glasses [45]. They used energy density E (i.e., the instantaneous energy per spin) to measure the nonequilibrium temperature. They prepared two systems at $T_A = 1.3$ and $T_B = 1.2$, which were then left to evolve to reach an initial energy $E_A \approx E_B$. When both the systems were quenched in a thermal reservoir at $T = 0.7$ (below the critical temperature T_c), the hotter preparation relaxed to low energies faster than the colder preparation. Although the initial preparation of the systems had similar energies (and temperatures), a clear distinction between the relaxation rates suggested that that relaxation processes are not completely governed by the initial temperatures. They observed the role of coherence length $\xi(t) \propto t^{1/z(T)}$ in controlling the spin-glass dynamics, where $z(T < T_c) \approx 9.6 T_c/T$. They argued that systems prepared at identical temperatures could have different ξ depending on their heating histories. Thus, the necessary condition for the Mpemba effect imposes that $\xi_A > \xi_B$ for a system with $T_A > T_B$. Similar to the cooling effect, the heating effect was observed to be symmetric, facilitating the inverse Mpemba effect in spin-glass systems.

Focusing on the particular case of water, numerical studies have also been done in other model systems such as molecular gases [46], driven molecular gas mixtures [47], inertial suspensions [48], cold gases [49], and quantum systems [50]. Gijón et al. studied the Mpemba-like effect in atomistic models of bulk water [51]. They modeled liquid water with the rigid TIP4P model [52], where the kinetic energy was distributed equally between the translational and rotational degrees of freedom at equilibrium, obeying the equipartition theorem. For cases where the total kinetic energy was placed only in either the translational modes or the rotational modes, the breaking of equipartition resulted in lowering of the system's temperature by a few degrees. They argue that placing a water sample in a colder environment creates a similar breaking of thermal equilibrium that could lead to the anomalous cooling in Mpemba's experiment.

Turning to granular systems, Santos et al. showed the Mpemba effect in homogeneous and isotropic states of molecular gases driven by an external drag force with a velocity-dependent friction coefficient [46]. Based on the kinetic theory framework used in this system, González et al. predicted the Mpemba effect in a binary mixture of two gases [47]. The mechanism stems from different amounts of heat transferred from the reservoir to different components. Contrary to granular fluids, neither kurtosis nor nonlinear drag forces were required for the emergence of the effect. Takada et al. report on sheared inertial suspensions and distinguish the generic normal Mpemba effect (where an initially hotter suspension cools

down faster than an initially colder suspension) from the nontrivial anomalous Mpemba effect (where an initially hotter suspension that cools slowly initially eventually catches up to an initially cooler suspension) [48]. Analogously, normal and anomalous inverse Mpemba effects and mixed Mpemba effects (where both cooling and heating are present) are also observed in these systems.

1.5 Mpemba effect in colloidal systems

In Sections 1.3 and 1.4, we have seen that the Mpemba effect has been observed not only in water but also in a variety of other experimental and simulated systems. However, these anomalous relaxations have proved difficult to explain clearly, and different mechanisms may be at play. In an effort to simplify both the system and the relevant physics, we design a simple experiment with a colloidal particle that diffuses in water and is subjected to an external potential. The particle is confined in a tilted double-well potential, situated asymmetrically in a box $[x_{\min}, x_{\max}]$ (Fig. 1.1). The barrier height can be chosen in such a way that there are two coarse-grained states (left and right domains in Fig. 1.1) with dynamics as fast as 1–10 ms between them. The advantage of using such a simple setup with a small timescale is that we can easily observe the Mpemba effect and obtain results with high reproducibility.

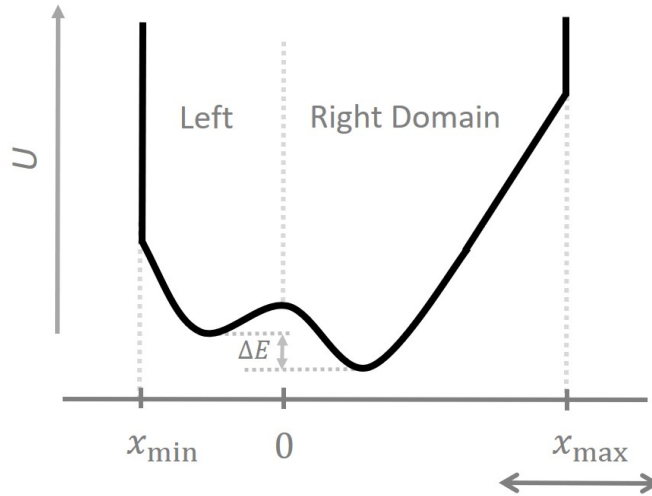


Figure 1.1: Energy landscape for the Mpemba effect.

Thus, instead of being just able to trap the particle, we need to create a potential whose shape is at least accurately known (to at least $0.1 k_B T$) and can preferably be specified as desired. In our experiment, the external potential imposed on the particle is a tilted double well. To understand our experimental approach, which was developed specifically for these experiments, we review methods for trapping and manipulation of particles in the next section.

1.6 Particle manipulation techniques

There has been an increasing interest in developing techniques to manipulate particles at micro- and nano-scales [53–55]. Manipulation can be done either on an individual particle or on a collection of particles. These techniques can be classified into active and passive methods. We will briefly review some of the widely used techniques and discuss their suitability for creating the potentials desired in our experiment.

1.6.1 Passive trapping

Passive trapping requires an inherent local minimum in the potential. The simplest example is a harmonic potential where a linear restoring force is exerted on a particle near the potential minimum. The trapping force can arise from the interaction of a particle with external inhomogeneous electric, magnetic, or temperature fields.

Optical tweezers

Light’s ability to exert forces has been known since 1619, when Kepler recognized that the Sun’s rays deflect comet tails [56]. These optical forces are extremely small in magnitude and proportional to the intensity of light [57]. This force, transferred to the illuminated objects, results in the radiation pressure pushing the object along the beam’s propagation direction. Light is composed of photons, a particle representing a quantum of light and carrying energy $u = hc/\lambda$, where h is the Planck constant, c the speed of light, and λ the wavelength of light. It carries a momentum $\mathbf{p} = \hat{\mathbf{p}} h/\lambda$, where $\hat{\mathbf{p}}$ is the unit vector along the propagation of light. For a normal incidence on a mirror, the change in momentum per unit time is $-2N\mathbf{p} = -\hat{\mathbf{p}} 2P/c$, where N is the total number of photons in an incident light of power P . The force $F = 2P/c$ is so small and difficult to detect that it had no practical application until Arthur Ashkin reported that one could use focused light to accelerate and trap micrometer-sized particles [58]. In 1986, Ashkin et al. showed the first demonstration of a single-beam optical tweezer (OT) to trap dielectric particles [59].

In a typical optical tweezers setup, a highly focused Gaussian beam is used to trap dielectric particles. When the beam interacts with the particle, *scattering* and *gradient* forces are exerted on the particle (Sec. 3.2). The scattering force pushes the particle in the direction of the beam propagation, and the gradient force exerts a restoring force towards the center of the beam (Fig. 1.2). If the contribution from the gradient forces is larger than that of the scattering forces, a restoring force is also created in the axial direction, and a stable trap is created. A description of the working principle of OT can be found in Sec. 3.2.

Although designed as an atom trap initially [60], optical tweezers were used in a variety of experiments such as trapping of silica beads [59], the study of the orientation of tobacco mosaic virus in the trap [61], damage-free trapping of *E. coli* using IR light to study its reproduction [62], the study of the elastic and viscoelastic properties of cytoplasm [63], and

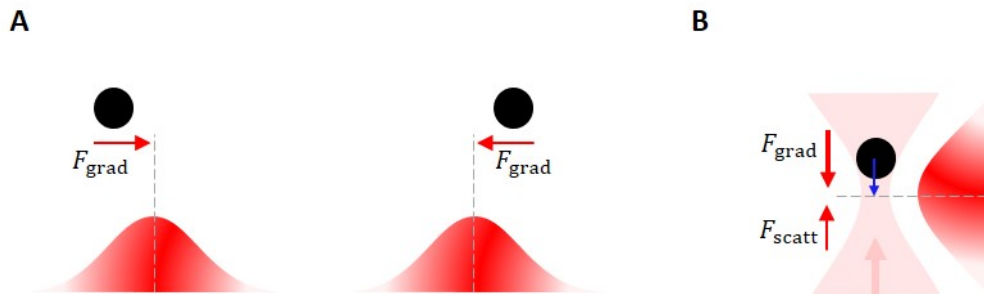


Figure 1.2: Working principle of optical tweezers. **A.** Transverse trapping: When a particle is displaced transversely from the focus of the beam, a restoring force pulls the particle towards the region of the laser beam with maximum intensity. The shaded red region represents the intensity profile of the trapping laser. **B.** Axial trapping: The resultant of the gradient force and the scattering force (blue arrow) creates a restoring force that pulls the particle towards the focus of the beam, yielding a stable trap.

so on. Since then, it has become a standard tool to exert piconewton forces on mesoscopic particles and detect their motion for physical [64–67], chemical [68, 69], and biological applications [63, 70–72]. OTs can manipulate particles with spatial resolution on the order of 0.1–1 nm and measure dynamics on millisecond-to-microsecond time scales [73].

Magnetic tweezers

Magnetic tweezers are a versatile single-molecule tool for applying both force and torque to tethered molecules, from individual molecules [74] to inter-molecular bonds [75] to whole cells [76]. In 1950, Crick and Hughes first demonstrated magnetic tweezers, using magnets to drag, twist, and prod magnetic particles within the cytoplasm of cells [77]. Later Smith et al., and Strick et al., used magnetic tweezers to stretch and coil an individual molecule of DNA tethered between a flow cell surface and a microscopic magnetic particle [78, 79]. In a typical setup, a light microscope is used to track the position of a magnetic (superparamagnetic or weakly ferromagnetic) particle in an external magnetic field. An external magnetic field \mathbf{H} results in a magnetic induction $\mathbf{B} = \mu_0(\mathbf{H} + \mathbf{m}/V)$, where \mathbf{m} is the dipole moment of the magnetic particle, μ_0 the vacuum permeability, and V the volume of the magnetic particle. The torque $\boldsymbol{\tau} = \mathbf{m} \times \mathbf{B}$ aligns the particle along the field. If the field has a gradient, the particle experiences a force $\mathbf{F} = (\mathbf{m} \cdot \nabla)\mathbf{B}$ towards the region with higher field density (Fig. 1.3).

Single-molecule manipulations such as optical tweezers and atomic force microscopes address one molecule in an individual experiment; as a result, they suffer low experimental throughput. Magnetic-force-based manipulation can facilitate parallel measurements of an ensemble of particles [80, 81]. Since magnetic tweezers do not produce an energy potential landscape that can restrict the motion of a particle in three dimensions, it is sometimes combined with optical tweezers for manipulation and interaction [82, 83]. You et al. combined

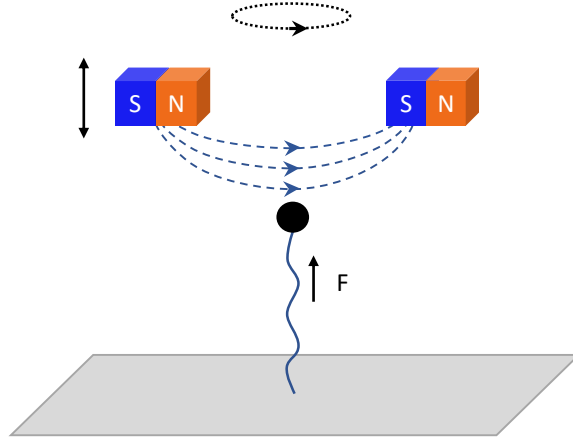


Figure 1.3: Working principle of magnetic tweezers. A pair of magnets produces a magnetic field gradient along the axial direction, which exerts a force on the super-paramagnetic beads in the upward direction. The force is controlled by moving the magnets in a vertical direction. The rotating magnets induce rotation of the magnetic beads.

these two techniques to use F_1 -ATPase to rotate single-molecule double-stranded DNA and thereby calculate the bending stiffness of DNA from the winding tension [84]. Magnetic tweezers with fluorescence microscopy have also been used to measure the distance of two fluorophores attached to single-stranded DNA as a function of the force applied by the magnetic field [85], probe the rotational motion of the fluorescent probe attached to a rotary motor [86], study the energetics of the conformational transitions in supercoiled DNA [87], and count the number of proteins bound to a single DNA molecule [88].

Magnetic tweezers are highly specific to the magnetic microparticles and do not interact with other particles of the sample. However, unlike OTs, magnetic tweezers do not create a three-dimensional trapping potential and require the attachment of the magnetic particles through a tether to the surface. Nonetheless, active feedback control can be used to create an effective trapping potential [89]. Passive magnetic tweezers have a typical spatial resolution of 5–10 nm and temporal resolution on the order of 10^{-1} – 10^{-2} s [90]. Compared to OTs and atomic force microscopes (AFMs), magnetic tweezers have low trap stiffness $\approx 10^{-3}$ – 10^{-6} pN/nm [90]. Note that the effective stiffness can be improved in feedback-based magnetic tweezers with better detection techniques and data-acquisition systems [89].

Holographic tweezers

Holographic optical tweezers (HOTs) use a computer-controlled diffractive optical element (DOE) to create arbitrary three-dimensional configurations of single-beam traps to capture and manipulate mesoscopic objects [91, 92]. These optical traps can be made dynamic and displaced in three dimensions by projecting a sequence of holograms [93–95]. Originally

demonstrated with microfabricated DOEs [96, 97], holographic tweezers have since been implemented with computer-controlled, liquid-crystal, spatial light modulators (SLMs) [95]. Holograms are placed on the DOE to shape the profile of an incoming optical beam. The DOE is positioned at the front focal plane of the Fourier lens, which collects the first-order diffracted beam so that the complex amplitude in the back focal plane of the Fourier lens (microscope objective in a tweezer setup) is the Fourier transform of the complex amplitude at the DOE plane (Fig. 1.4). Thus, to get a desired intensity pattern in the front focal plane, it is sufficient to take its inverse Fourier transform to determine the appropriate hologram to place on the DOE. Employing such holograms requires modulating both the amplitude and phase of the incoming beam. Generally, amplitude modulations are undesirable as they reduce the trapping efficiency of the beam. Thus, phase-only holograms, also known as kinoforms [98], are employed to shape the wavefronts of the light beams. There are several algorithms proposed to create holograms that most accurately and most rapidly approximate desired trapping patterns [99].

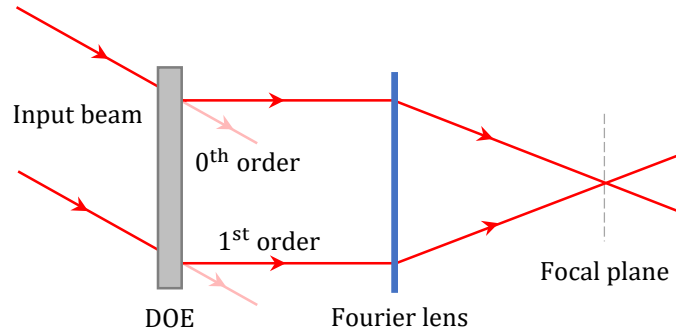


Figure 1.4: Working principle of holographic optical tweezers. A diffractive optical element placed at the front focal length of the Fourier lens modifies the beam profile of the incoming beam. The complex amplitude in the back focal plane of the Fourier lens is the Fourier transform of the complex amplitude in the DOE plane. Adapted from [99].

Holographic tweezers can move particles precisely in three dimensions without any mechanically moving parts. Other applications of HOTs include trapping of multiple particles [94, 100–103], light-field engineering [104, 105], and shaping arbitrary optical potentials [106, 107]. Manipulation of soft biomaterials requires a proper characterization of HOTs [108, 109]. An advantage of HOTs over conventional optical tweezers is that the trapping stiffness of the holographic tweezers can be constant within $\pm 3\%$ over a range of 3 to 4 μm [109].

The temporal resolution of the holographic tweezers is limited by refresh rate of the SLM (≈ 100 Hz). Moreover, since the spatial scale of the holographic traps is diffraction-limited, the requirement of designing a potential shape on sub-diffraction length scales becomes

impossible. The electronic jitter during the transfer of the kinoform from the computer to the SLM can create noisy, undesirable external forces on the trapped particles.

1.6.2 Active trapping

Active traps use dynamically controlled forces to create potentials, which are a discrete approximation of a real potential. In a real potential, the force exerted by a potential changes as soon as the particle changes. However, in an active trap, the forces are applied once per feedback cycle. Since active traps just require forces to manipulate particles, the source of these forces can be anything. Based on the type of interaction between a particle and an external force-field, active traps can be electrokinetic, hydrodynamic, acoustic, or thermal. We will now briefly discuss their working principles, applications, and the possibility of being used in our experiment.

Electrokinetic traps

In 2005, Cohen and Moerner constructed an Anti-Brownian ELectrokinetic (ABEL) trap based on active feedback using electrophoretic forces to trap nanoparticles as small as 20 nm in water [110]. The ABEL trap monitors the Brownian motion of a particle and applies a feedback voltage in a microfluidic cell to create electrokinetic (electrophoresis and electroosmotic) forces that cancel the Brownian motion (Fig. 1.5). Electrokinetic traps use both electrophoretic and dielectrophoretic forces to apply an electric field to trap and manipulate nanometer-to-millimeter-sized particles [111, 112]. Electrophoretic forces arise from the interaction of the object’s fixed charge and the electric field, whereas dielectrophoretic forces arise from the polarizability in a spatially inhomogeneous electric field. The restoring force in an optical trap is a second-order interaction with the applied electric field and proportional to the polarizability of the object, which scales as d^3 (where d is the diameter of the particle). Thus, it becomes extremely difficult to trap sub-50 nm particles. Electrokinetic traps, on the other hand, use a first-order ($\sim d$) effect and that can impose velocities on the trapped particles that are approximately $100 \times$ greater than those applied by typical optical tweezers [113].

ABEL traps have been used to study individual protein molecules without any attachment to beads or surfaces, single virus particles, lipid vesicles, fluorescently labeled DNA, single fluorophores, and semiconductor nanocrystals [114–116]. Cohen used the ABEL traps to create more complicated arbitrary potentials based on feedback in 2D space [117]. Jun et al. extended the technique to make more quantitative measurements in potentials created by electrokinetic feedback, also known as *virtual* potentials [118]. Gavrilov et al. [119] used virtual double-well potentials to test Landauer’s principle [120] in the context of stochastic thermodynamics and information theory. These applications involved two-dimensional manipulation of the trapped particle where the axial confinement is provided by the geometry of the trapping chamber. A further extension to a three-dimensional ABEL trap

has been done using four electrodes in a tetrahedral arrangement to trap 40-nm fluorescent nanoparticle in solution [121] and employing microfluidics [122].

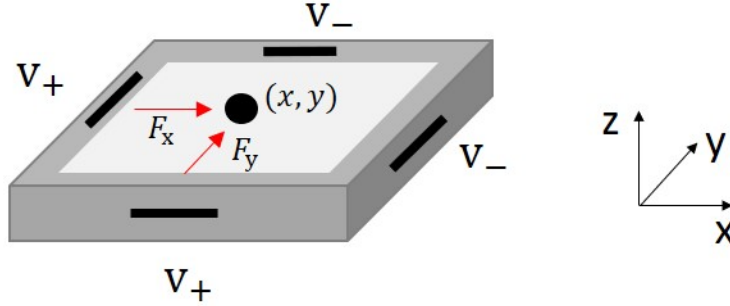


Figure 1.5: Working principle of electrokinetic tweezers. Voltages V_{\pm} are applied across a pair of electrodes (e.g., platinum wires) to exert electrical forces on a particle. In a typical setup, the forces (F_x, F_y) are applied in two dimensions. The position (x, y) of an object is tracked in real time, and appropriate forces are exerted to approximately cancel the Brownian motion.

It is possible to use electrokinetic forces to create potentials on nanometer scales with fast dynamics. But these traps introduce drifts due to chemical reactions at the electrodes. Thus, continuous measurement and correction are required to compensate for drifts in real time [123].

Hydrodynamic traps

Hydrodynamic trapping is a method that utilizes fluid flow or microstructures in the channels to trap small particles in an aqueous solution [124]. Hydrodynamic trapping can be contactless or involve contact [125, 126]. Contactless methods rely on the stagnation point flows [127, 128] or microeddies [129] in microchannels. Figure 1.6A shows a system where a particle is naturally trapped at the stagnation point of a flow along the input flow axis (compression axis) but requires an active feedback control along the output flow axis (extension axis), thereby forming a feedback-stabilized potential well [127]. Figure 1.6B shows a hydrodynamic trap based on eddy currents. When an oscillating fluid (≤ 1 kHz) interacts with a fixed cylinder inside a microfluidic chamber, steady eddies are generated around the solid boundaries. The number of eddies generated depends on the geometry of the solid boundary and the oscillation conditions. Each eddy center can trap a particle, precisely at the channel midplane, away from the surface. Tanyeri et al. used an active flow control to trap and manipulate particles of sizes 100 nm to 15 μm at the intersection of two flow channels [127, 128]. Johnson-Chavarria et al. used a microfluidic-based single-cell microbioreactor (SCM) to investigate the growth over successive generations of cells grown in free solution, gene expression, and intracellular diffusion of repressor proteins while precisely tuning the cell growth environment [130].

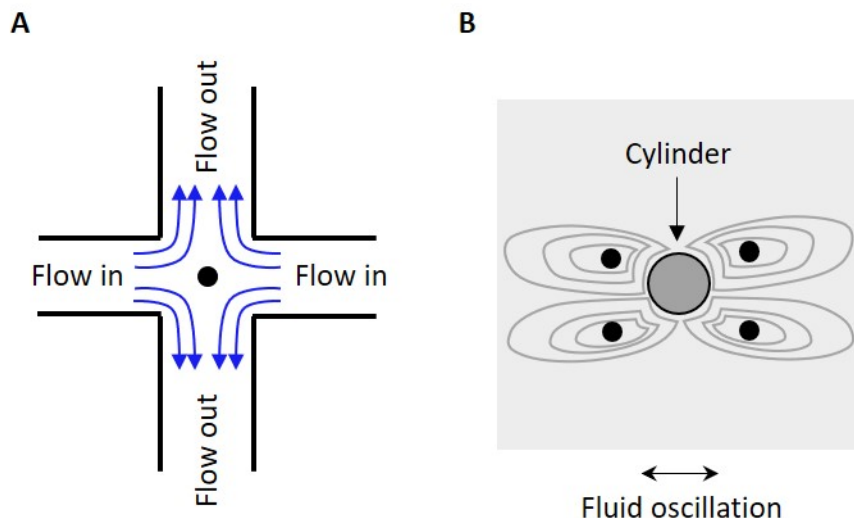


Figure 1.6: Working principle of hydrodynamics traps. **A.** Two opposite laminar flow fields create a stagnation at the junction of two perpendicular microchannels. A particle can be trapped at a position where the local fluid velocity is zero. **B.** The interaction of an oscillating flow field with a cylinder (center) creates eddies around it. Each eddy can trap a particle near its center without contacting any solid surface. The black discs are trapped particles (not drawn to scale). Adapted from [127, 129].

Contact-based methods are efficient in trapping a very large number of particles to form dynamic arrays for high-throughput studies [131–135]. Chen et al. used U-shaped micro-wells for *in situ* culture of laterally trapped single cells and observed that the population doubling time of both single HDF and K562 cells was larger than that of cells cultured as bulk populations in static plates [136]. Lateral-trapping techniques have also enabled gene-expression analysis [137], single-cell tumor apoptosis analysis [138], isolation of single cells from an ensemble of suspended cells [139], and super-resolution imaging of specimens [140, 141].

In general, hydrodynamic traps can easily trap and manipulate any objects with micro- to nano-scale dimensions with no requirement on their material compositions. Contrary to trapping with optical, acoustic, magnetic, or dielectrophoretic forces, where the force exerted scales with the particle volume, hydrodynamic forces scale linearly with particle radius. Despite these advantages, the low spatial resolution (1–10 μm) will limit the potential to larger length scales, with slower characteristic time scales [127] and thus fewer repetitions of the experiment.

Acoustic traps

Acoustic tweezers manipulate matter both spatially and temporally by using the interaction of sound with solids, liquids, and gases. Because acoustic waves with frequencies in the

kilohertz-to-megahertz range can be easily generated, acoustic traps can directly manipulate particles across length scales from 10^{-7} – 10^{-2} m [142]. In 1991, Wu first showed that latex particles and frog eggs could be manipulated by acoustic tweezers using two collimated focused ultrasonic transducers [143]. Acoustic tweezers provide unique characteristics com-

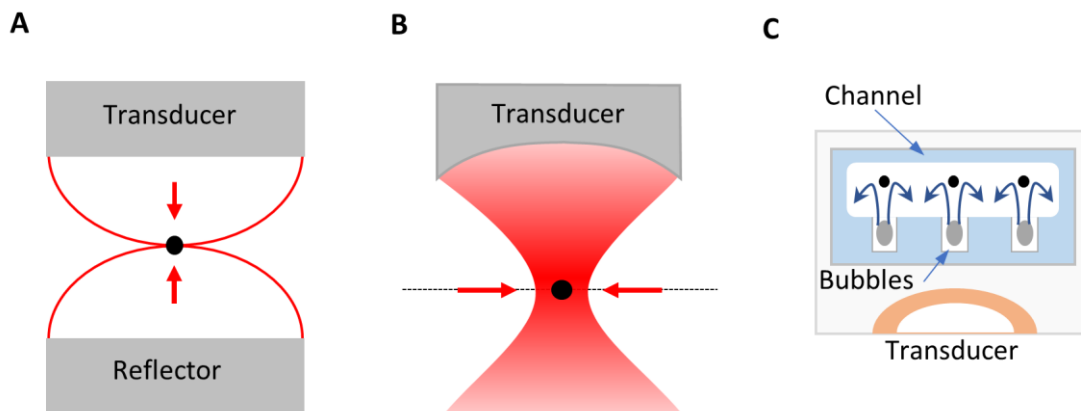


Figure 1.7: Working principle of acoustic tweezers. **A.** Standing-wave tweezers are formed by interference between an incident and a reflected wave. Particles trapped at the pressure nodes of a standing wave can be manipulated by changing the acoustic resonant frequency. **B.** Using a high-frequency ultrasound transducer, a strong acoustic gradient in a focused acoustic wave can trap a particle in three dimensions. **C.** Acoustic-streaming tweezers use oscillation microbubbles inside a microfluidic channel to induce acoustic flows. Adapted from [144, 145].

pared to other trapping techniques, such as high trapping forces per unit input power and the ability to manipulate particles of sizes ranging from centimeter to micrometer [144, 145]. The primary types of acoustic tweezers are standing-wave tweezers, traveling-wave tweezers, and acoustic-streaming tweezers. Standing-wave tweezers are formed by the interference of incident and reflected waves establishing a pressure distribution in a fluid (Fig. 1.7A). The pressure gradient, in return, produces the acoustic radiation force that assists in trapping [146, 147]. Compared to standing-wave acoustic tweezers, the acoustic field strength of a traveling-wave acoustic field is small [148]. Thus, manipulation in 3D space is achieved by focusing the acoustic field in a small region and controlling its phase (Fig. 1.7B) [149]. Based on Gor'kov's theory, an axisymmetric focused beam can transversely trap relatively light and soft particles such as droplets at the central pressure maximum, but a relatively dense and stiff particle would be repelled away from the beam axis [150]. Sometimes the manipulation is done via acoustically induced fluid flows, also known as acoustic-streaming tweezers [151, 152]. Such streaming is generated using oscillating microbubbles or oscillating solid structures (Fig. 1.7C). These microbubbles can produce sufficient acoustic radiation forces to trap and rotate particles at a fixed position. By gradually rotating *C. elegans*, green fluorescent protein-expressing cells that appear to overlap in a single view can be

resolved and clearly imaged [153]. Other applications include cell patterning [146], material manufacture [154], cell transportation [155], and particle separation and sorting [156–158].

Acoustic tweezers have a diffraction-limited spatial resolution (1–10 μm), which is still larger than we would prefer. Another issue is that the trapping force in an acoustic field depends on the size and compressibility of the particle and cannot differentiate between cells of different types with the same size. These issues can be addressed by combining acoustic tweezers with other techniques such as magnetic [159], optical [160], and electrical forces [161].

Thermal traps

Heating due to laser beams may affect the performance of trapping due to increased thermal energy of the particle and damage biological samples [162–165]. However, the same effect has been used to trap dielectric particles and bacteria and is known as opto-thermoelectric nanotweezers (OTENT) [166]. When a temperature gradient is imposed in an electrolytic solution, ions migrate directionally because of thermophoresis. The difference in Soret coefficients between oppositely charged ions separates the charges, generating an electric field [167]. The dependence of thermoelectricity on temperature gradients rather than absolute temperature change allows trapping at a significantly lower laser power (0.05–0.4 $\text{mW}/\mu\text{m}^2$). Thermophoresis and the convection current induced by illuminating a highly absorbent hydrogenated amorphous silicon-coated surface is observed to reduce the trapping optical power required and create stiffer traps [168]. For strongly absorbing particles, the induced thermal gradient repels the temporarily trapped particles away from the laser center. Upon being slowed down by the viscous drag of the medium, the repelled particles are attracted towards the optical trap (Fig. 1.8). An interplay between thermophoretic and optical forces sets up an opto-thermal oscillation during three-dimensional manipulation [169].

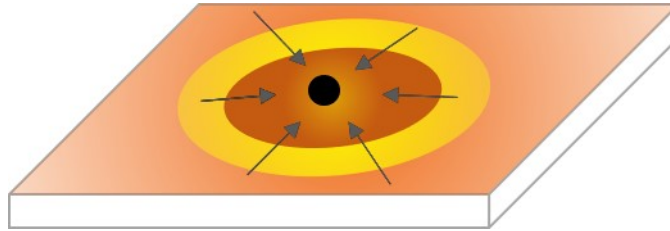


Figure 1.8: Working principle of thermal tweezers. A radial temperature gradient is produced when light is directed on a thermo-plasmonic substrate. The temperature gradient can trap positively charged metal nanoparticles at the center of the induced field or the laser spot. Adapted from [166].

Since thermal trapping methods are inherently limited to 2D manipulation and exert forces near the surface, it may be difficult to characterize the potential acting on a particle due to hydrodynamic interactions with the surface [170].

1.7 Combining feedback traps and optical tweezers

In Sec. 1.6, we discussed different trapping techniques and their applications. The requirement of any specific technique would depend upon the goal of an experiment. For the work reported on in this thesis, we require a technique to create potentials on nanometer length scales, with features that can provide fast dynamics on the order of milliseconds. Thus, trapping techniques such as holographic tweezers, hydrodynamic and acoustic trapping cannot be used because their spatial and temporal resolutions are too low. Although magnetic tweezers have high resolution, their low trapping stiffness and sophisticated feedback control for three-dimensional confinement make them less desirable for our purpose. The electrokinetic trap is a strong candidate to meet these demands and can arbitrarily shape a potential at sub-diffraction length scales. However, the complex calibration procedures required to compensate for chemical drifts in forces can be inconvenient [123]. Thus, we decided to use optical tweezers in our experiments. They have high spatial and temporal resolutions and provide inherent three-dimensional confinement of a dielectric particle in space. However, creating a potential shown in Fig. 1.1 is still challenging with conventional optical tweezers. Time-shared OTs have been used to create static double-well potentials by rapidly scanning the trap center between two positions [171]. But controlling independently parameters such as well separation, barrier height, tilt, and outer curvatures is impossible by time-sharing the trap positions. In addition, optical tweezers based on time-shared and holographic tweezers can create potentials that have micrometer-scaled features, limited by diffraction (wavelength of light used for the tweezer). Thus, we require a new technique to create arbitrary energy landscapes on sub-diffraction length scales with OTs. To meet these requirements, we have developed a new apparatus based on feedback control with optical tweezers. Using feedback-based optical tweezers, we can create double-well potentials on the length scale of $\lesssim 100$ nm. The approximately tenfold decrease in length scales of feedback tweezers implies a 100-fold decrease in time scales. Not only are measurements at comparable statistics 100 times faster, but also the effects of temperature drifts on the equilibrium trap positions become negligible.

1.8 Overview of the thesis

In this thesis, I will present the work and ideas developed by myself and Dr. John Bechhoefer during my Ph.D. project.

Chapter 2 presents the theory of Brownian motion in overdamped systems. The motion of a Brownian particle in an external potential is discussed in the context of both Langevin and Fokker-Planck dynamics. The theoretical background laid in this chapter lays the foundation of analysis for the Mpemba effect.

Chapter 3 presents the development of our new feedback-based optical tweezers. The experimental setup to design such traps and step-by-step calibration methods for OTs are

discussed in detail. We also demonstrate arbitrary shapes of potentials designed using our apparatus.

Chapter 4 presents the work on the Mpemba effect. We demonstrate that we can experimentally observe the Mpemba effect in colloidal systems with high reproducibility and quantitative agreement with the existing theory for Markov systems. We demonstrate that, with the nanoscale potentials created by our feedback trap, we can perform an instantaneous quench in a bath and achieve an equilibration time of ≈ 100 ms, allowing us to do many repetitions of the experiment. We also demonstrate the strong Mpemba effect and present a geometrical interpretation of the conditions required for an exponential speedup of a cooling process. The theory for the geometric interpretation is developed with Raphaël Chétrite.

Chapter 5 discusses the experimental observation of the inverse Mpemba effect in colloidal systems. We also demonstrate the first experimental observation of the strong inverse Mpemba effect.

Chapter 6 summarizes the work done in the thesis and discusses the future scope of this work.

Chapter 2

Particle dynamics

The rapid oscillatory motion of pollen grains in the ovulum of a plant was the first microscopic observation of Brownian motion, named after a Scottish botanist Robert Brown [172]. In 1905, Albert Einstein helped initiate the modern study of random processes with his groundbreaking paper on Brownian motion [173], which led to a fully probabilistic formulation of statistical mechanics and a well-established subject of physical investigation. Einstein also showed that the mean-squared displacement of the Brownian particles is related to a diffusion coefficient and so was able to derive a diffusion equation for the probability density of the Brownian particles. In 1908, Langevin showed that a random Markov force could model the random collisions and interaction between the particle and its surrounding fluid. The resulting dynamics were described by a stochastic differential equation [174]. Fokker in 1914 [175] and Planck in 1917 [176] introduced a partial differential equation that governs the evolution of the probability density for the velocity of the Brownian particle under the influence of a drift generated by the friction in the fluid. By solving the Fokker-Planck equation, one obtains probability distribution functions, from which single-point averages of macroscopic variables can be obtained.

In this chapter, we will briefly discuss the Langevin and Fokker-Planck approaches in the context of a Brownian particle in a potential. The discussion here will lay the foundations for the analysis in Chapter 4.

2.1 The Langevin equation

2.1.1 A free particle

If a small particle of mass m is immersed in a large container of fluid, friction or damping forces act on the particle, and the equation of motion is given by [174, 177–179]

$$m \frac{d^2 x}{dt^2} + \gamma \frac{dx}{dt} = \sqrt{2k_B T \gamma} \zeta(t), \quad (2.1)$$

where $\gamma \approx 6\pi\eta R$ is the Stokes friction coefficient for a sphere of radius R infinitely deep inside a fluid with viscosity η , k_B the Boltzmann constant, and $\zeta(t)$ Gaussian white noise modeling thermal fluctuations of the bath at temperature T . Note that we have ignored the frequency dependence of the frictional force due to the hydrodynamic interaction with the surrounding fluid [170], as it is relevant only at frequencies f_ν higher than those relevant for our experiment, where $f_\nu \equiv \eta/(\pi\rho R^2) = 550$ kHz with $\rho = 1$ gm/cm³ the density of the fluid. Equation 2.1 is a stochastic differential equation that is known as the Langevin equation. The mean of $\zeta(t)$, at a given time t , over an ensemble of particles is zero

$$\langle \zeta(t) \rangle = 0. \quad (2.2)$$

The autocorrelation between the values of ζ at different times t_1 and t_2 is assumed to be zero unless $|t_1 - t_2|$ is very small; i.e.,

$$\langle \zeta(t_1)\zeta(t_2) \rangle = \delta(t_1 - t_2), \quad (2.3)$$

where $\delta(t_1 - t_2)$ is the Dirac delta function. The assumption above seems reasonable because the collisions of different molecules of the fluid with the small particle occur on very short time scales ($\approx 10^{-13}$ s) and are approximately independent.

2.1.2 A trapped particle

The dynamics of an optically trapped bead are well described by

$$m \frac{d^2x}{dt^2} = -\gamma \frac{dx}{dt} - kx + \sqrt{2k_B T \gamma} \zeta(t), \quad (2.4)$$

where $-kx$ is the restoring force due to an optical trap. For small displacements from the trap center, the force produced by an optical potential $U = (1/2)kx^2$ obeys Hooke's law and increases linearly with the displacement of the particle. Often, experiments with optical tweezers are done in a *low-Reynolds-number* regime. In this regime, the particle stops within a fraction of a microsecond when an applied force is removed. Since the damping is very fast (generally smaller than the time scales typically used in experiments) and viscosity dominates over inertia, the inertial term in Eq. 2.4 can be neglected, i.e., $m = 0$ to write

$$\frac{dx}{dt} = -\frac{x}{\tau_c} + \sqrt{2D} \zeta(t), \quad (2.5)$$

where $D = k_B T / \gamma$ is the diffusion coefficient of the particle and $\tau_c = \gamma / k$ the trap characteristic time. The solution, starting at $x(t=0) \equiv x_0$ is

$$x(t) = x_0 e^{-t/\tau_c} + \sqrt{2D} \int_0^t dt' e^{-(t-t')/\tau_c} \zeta(t'). \quad (2.6)$$

We can calculate the position autocorrelation function (ACF) of an optically trapped bead as [99]

$$\begin{aligned} \langle x(t_1)x(t_2) \rangle &= x_0 e^{-(t_1+t_2)/\tau_c} + \sqrt{2D}x_0 e^{-t_1/\tau_c} \int_0^{t_2} dt'' e^{-(t_2-t'')/\tau_c} \langle \zeta(t'') \rangle + \sqrt{2D}x_0 e^{-t_2/\tau_c} \times \\ &\quad \int_0^{t_1} dt' e^{-(t_1-t')/\tau_c} \langle \zeta(t') \rangle + 2D \int_0^{t_1} dt' \int_0^{t_2} dt'' e^{-(t_1+t_2-t'-t'')/\tau_c} \langle \zeta(t')\zeta(t'') \rangle. \end{aligned} \quad (2.7)$$

The second and third terms in the above equation vanish because of Eq. 2.2. Thus, we have

$$\langle x(t_1)x(t_2) \rangle = x_0 e^{-(t_1+t_2)/\tau_c} + 2D \int_0^{t_1} dt' \int_0^{t_2} dt'' e^{-(t_1+t_2-t'-t'')/\tau_c} \langle \zeta(t')\zeta(t'') \rangle. \quad (2.8)$$

The only contribution to the integral in the second term comes when $t' = t''$, as implied by Eq. 2.3. We can then simplify the equation as

$$\begin{aligned} \langle x(t_1)x(t_2) \rangle &= x_0 e^{-(t_1+t_2)/\tau_c} + 2D \int_0^{t_1} dt' \int_0^{t_2} dt' e^{-(t_1+t_2-2t')/\tau_c}, \\ &= x_0 e^{-(t_1+t_2)/\tau_c} + 2D \int_0^{\min(t_1, t_2)} dt' e^{-(t_1+t_2-2t')/\tau_c}, \\ &= x_0 e^{-(t_1+t_2)/\tau_c} + \frac{2D\tau_c}{2} \left[e^{-(t_1+t_2-2t')/\tau_c} \right]_0^{\min(t_1, t_2)}, \\ &= x_0 e^{-(t_1+t_2)/\tau_c} + D\tau_c \left[e^{-(t_1+t_2-2\min(t_1, t_2))/\tau_c} - e^{-(t_1+t_2)/\tau_c} \right], \\ &= x_0 e^{-(t_1+t_2)/\tau_c} + D\tau_c \left[e^{-|t_1-t_2|/\tau_c} - e^{-(t_1+t_2)/\tau_c} \right] \end{aligned} \quad (2.9)$$

Substituting $t = t_1$ and $t_2 = t + \tau$, we rewrite Eq. 2.9 as

$$\langle x(t)x(t + \tau) \rangle = x_0 e^{-(2t+\tau)/\tau_c} + D\tau_c \left[e^{-|\tau|/\tau_c} - e^{-(2t+\tau)/\tau_c} \right]. \quad (2.10)$$

In the long-time limit, $t \rightarrow \infty$, the autocorrelation is approximated as

$$\langle x(t)x(t + \tau) \rangle \approx D\tau_c e^{-|\tau|/\tau_c} = \frac{k_B T}{k} e^{-|\tau|/\tau_c}. \quad (2.11)$$

For $|\tau| \gg \tau_c$, the correlations go to zero. Thus, position measurements far apart in time are independent and uncorrelated. Equation 2.11 can also be derived from Eq. 2.17 using *Wiener-Khintchine* theorem, which states that the ACF is the Fourier transform of the power spectrum [180].

As the stiffness of the trap increases, the particle experiences a stronger restoring force, and the characteristic time τ decreases. The particle in a stiff trap explores a smaller phase space than the one in a weaker trap. The mean-squared displacement (MSD) of a trapped,

diffusing particle is given as [99]

$$\text{MSD}(\tau) \equiv \langle x(\tau) - x(0) \rangle^2 = 2 \frac{k_B T}{k} \left[1 - e^{-|\tau|/\tau_c} \right], \quad (2.12)$$

which reaches a plateau because of the confinement imposed by the trap. For $\tau \ll \tau_c$, we obtain Einstein's relation $\text{MSD}(\tau) = 2D\tau$ for a freely diffusing particle. The transition from linear growth to the plateau occurs at about τ_c .

The trap characteristic time can be measured from the power spectral analysis of the Brownian motion of a trapped particle. The power spectrum of a trapped particle trajectory decomposes the motion $x(t)$ into contributions at each frequency, each with a particular power. The power spectrum density (PSD) of a signal $x(t)$ is the squared modulus of its Fourier transform.

The Fourier transform $\tilde{g}(\omega)$ of a function $g(t)$ is defined as

$$\tilde{g}(\omega) = \int_{-\infty}^{\infty} dt \, e^{i\omega t} g(t), \quad (2.13)$$

where $\omega = 2\pi f$ is the angular frequency. Taking the Fourier transform of Eq. 2.5, we obtain

$$-i\omega \tilde{x} = \frac{\tilde{x}}{\tau_c} + \sqrt{2D} \tilde{\zeta}, \quad (2.14)$$

Thus, the Fourier transform of $x(t)$ is

$$\tilde{x} = \frac{\tau_c \sqrt{2D} \tilde{\zeta}}{-1 - i\tau_c \omega}. \quad (2.15)$$

Taking the squared modulus of both sides of Eq. 2.15 gives the power spectral density of the particle motion,

$$S(\omega) \equiv |\tilde{x}|^2 = \frac{2D \tau_c^2}{1 + \omega^2 \tau_c^2}. \quad (2.16)$$

By substituting $\omega = 2\pi f$ and $\tau_c = 1/2\pi f_c$, we obtain

$$S(f) \equiv |\tilde{x}|^2 = \frac{D}{2\pi^2(f^2 + f_c^2)}, \quad (2.17)$$

where f_c is the corner frequency of the power spectrum. The form of the power spectrum in Eq. 2.17 is known as a *Lorentzian* [170, 181, 182].

2.2 Fokker-Planck equation

A complete solution of a macroscopic system requires solving all the microscopic equations of the system. These methods can either be computationally extremely expensive or rather

impossible in many cases. Instead, we can describe the system by macroscopic variables that fluctuate in a stochastic way. The Fokker-Planck equation (FPE) is just an equation of motion for the distribution function of fluctuating macroscopic variables. The FPE is a special case of the Kramers-Moyal expansion [183] with the equation of motion of probability given as

$$\frac{\partial p(x, t)}{\partial t} = \left[-\frac{1}{\gamma} \frac{\partial}{\partial x} U'(x) + D \frac{\partial^2}{\partial x^2} \right] p(x, t) \equiv \mathcal{L}_{\text{FP}} p(x, t), \quad (2.18)$$

where \mathcal{L}_{FP} is the Fokker-Planck operator for the Brownian motion with $U'(x) \equiv d_x U(x)$. Note that we use the notation d_x (or ∂_x) to represent derivatives (or partial derivatives) with respect to a variable x for inline equations. For heavily overdamped dynamics, the velocity variables that would otherwise be present in the FP equation may be neglected. In this limit, the FP equation is sometimes referred to as the Smoluchowski equation [183].

At steady state, the probability distribution $p_s(x)$ obeys

$$\frac{\partial}{\partial x} \mathcal{J}(x) = 0, \quad (2.19)$$

where the probability current $\mathcal{J}(x)$ is defined to be

$$\mathcal{J}(x) \equiv -\frac{U'(x)}{\gamma} p(x) - D \frac{\partial p}{\partial x}. \quad (2.20)$$

Equation 2.19 implies that the probability current should be constant in space. The value of the constant depends on the boundary conditions imposed on the probability distribution. If $\mathcal{J}(x) = 0$ at the boundaries, the probability current is uniformly zero for all x , in the stationary state. Then

$$\mathcal{J}(x) \equiv -\frac{U'(x)}{\gamma} p(x) - D \frac{\partial p}{\partial x} = 0 \quad (2.21)$$

readily gives the steady-state solution as

$$p_s(x) \propto \exp \left[\frac{-U(x)}{\gamma D} \right]. \quad (2.22)$$

Comparing $p_s(x)$ with the *Boltzmann* distribution $p = p_0 \exp[-U(x)/k_B T]$, we obtain the Einstein relation $D = \frac{k_B T}{\gamma}$, which is the simplest statement of the *fluctuation-dissipation* theorem [178]. It relates the intensity of fluctuation (D) to the rate of energy dissipation (γ) in a system at thermal equilibrium.

For nonstationary solutions, the Fokker-Planck equation can be solved by assuming a separation ansatz for the probability distribution

$$p(x, t) = \sum_{k=1}^{\infty} a_k(t) v_k(x). \quad (2.23)$$

After inserting Eq. 2.23 into Eq. 2.18, we get the eigenvalue problem

$$\mathcal{L}_{\text{FP}} v_k(x) \equiv \left[D \frac{\partial}{\partial x} \left(\frac{U'(x)}{k_B T} \right) + D \frac{\partial^2}{\partial x^2} \right] v_k(x) = -\lambda_k v_k(x), \quad (2.24)$$

with time-dependent coefficients $a_k(t)$ given by

$$a_k(t) = a_k(0) e^{-\lambda_k t}. \quad (2.25)$$

Here $v_k(x)$ and λ_k are the eigenfunctions and eigenvalues of the Fokker-Planck operator \mathcal{L}_{FP} with appropriate boundary conditions.

2.2.1 Adjoint of the Fokker-Planck operator

Since \mathcal{L}_{FP} is generally not Hermitian, we will also need to consider the eigenfunctions $u_k(x)$ of the adjoint operator $\mathcal{L}_{\text{FP}}^\dagger$

$$\mathcal{L}_{\text{FP}}^\dagger u_k(x) = -\chi_k u_k(x), \quad (2.26)$$

where χ_k are the eigenvalues of the adjoint operator $\mathcal{L}_{\text{FP}}^\dagger$. The adjoint of \mathcal{L}_{FP} is defined such that

$$\langle \mathcal{L}_{\text{FP}}^\dagger \phi | \psi \rangle = \langle \phi | \mathcal{L}_{\text{FP}} \psi \rangle, \quad (2.27)$$

for arbitrary functions $\phi(x)$ and $\psi(x)$, where $\langle \dots \rangle$ denotes the inner product

$$\langle \phi | \psi \rangle = \int dx \phi^*(x) \psi(x). \quad (2.28)$$

Below, we will prove that the eigenvalues λ_k of \mathcal{L}_{FP} are equal to the complex conjugate of the eigenvalues χ_k of $\mathcal{L}_{\text{FP}}^\dagger$.

Thus, we will need to evaluate (numerically) not only the right eigenfunction but also the associated left eigenfunction of the adjoint $\mathcal{L}_{\text{FP}}^\dagger$ of the FP operator [184]. One subtlety is that the boundary conditions for $\mathcal{L}_{\text{FP}}^\dagger$ differ from those of the \mathcal{L}_{FP} operator. In our system, the probability density function for a particle to be found at position x at a time t after a quench, $p(x, t)$, obeys the Fokker-Planck (FP) equation $\partial_t p = \mathcal{L}_{\text{FP}} p$ with the boundary

condition

$$\mathcal{J}(x_{\min}) = \mathcal{J}(x_{\max}) = 0, \quad (2.29)$$

which expresses that there is no flux of particles in or out of the boundaries.

To find $\mathcal{L}_{\text{FP}}^\dagger$ and its boundary conditions, we evaluate the inner product of functions $\phi(x)$ and $p(x)$

$$\langle \phi | \mathcal{L}_{\text{FP}} p \rangle = \int_{x_{\min}}^{x_{\max}} dx \left[\phi(x) \frac{\partial}{\partial x} \left[D \frac{U'(x)}{k_{\text{B}} T} p(x) \right] \right] + D \int_{x_{\min}}^{x_{\max}} dx \phi(x) \left(\frac{\partial^2 p}{\partial x^2} \right). \quad (2.30)$$

Evaluating both integrals by parts, we can write

$$\begin{aligned} \langle \phi | \mathcal{L}_{\text{FP}} p \rangle = & - \int_{x_{\min}}^{x_{\max}} dx \left[D \frac{U'(x)}{k_{\text{B}} T} \left(\frac{\partial \phi}{\partial x} \right) p(x) \right] + \left[\phi(x) D \frac{U'(x)}{k_{\text{B}} T} p(x) \right]_{x_{\min}}^{x_{\max}} \\ & - D \int_{x_{\min}}^{x_{\max}} dx \left(\frac{\partial \phi}{\partial x} \frac{\partial p}{\partial x} \right) + D \left[\phi(x) \frac{\partial p}{\partial x} \right]_{x_{\min}}^{x_{\max}}. \end{aligned} \quad (2.31)$$

Integrating the third term in the above expression again by parts gives

$$\begin{aligned} \langle \phi | \mathcal{L}_{\text{FP}} p \rangle = & \int_{x_{\min}}^{x_{\max}} dx \left[-D \frac{U'(x)}{k_{\text{B}} T} \left(\frac{\partial \phi}{\partial x} \right) + D \frac{\partial^2 \phi}{\partial x^2} \right] p(x) \\ & + \left[\phi(x) D \frac{U'(x)}{k_{\text{B}} T} p(x) + \phi(x) D \frac{\partial p}{\partial x} - D \left(\frac{\partial \phi}{\partial x} \right) p(x) \right]_{x_{\min}}^{x_{\max}} \\ = & \langle \mathcal{L}_{\text{FP}}^\dagger \phi | p \rangle - \left[\phi(x) \mathcal{J}(x) + D \left(\frac{\partial \phi}{\partial x} \right) p(x) \right]_{x_{\min}}^{x_{\max}}, \end{aligned} \quad (2.32)$$

where $\mathcal{L}_{\text{FP}}^\dagger = -D \frac{U'(x)}{k_{\text{B}} T} \partial_x + D \partial_{xx}$ is the adjoint of \mathcal{L}_{FP} . In order to have $\langle \phi | \mathcal{L}_{\text{FP}} p \rangle = \langle \mathcal{L}_{\text{FP}}^\dagger \phi | p \rangle$, all boundary terms in Eq. 2.32 have to vanish. The probability current \mathcal{J} already vanishes because of the condition imposed on the operator \mathcal{L}_{FP} (Eq. 2.29). Thus, a separate boundary condition is imposed on $\mathcal{L}_{\text{FP}}^\dagger$ such that it obeys Neumann boundary conditions for ϕ ,

$$\left. \frac{\partial \phi}{\partial x} \right|_{x=x_{\min}} = \left. \frac{\partial \phi}{\partial x} \right|_{x=x_{\max}} = 0. \quad (2.33)$$

2.2.2 Eigenfunctions and eigenvalues of the Fokker-Planck operator

The eigenvalues of \mathcal{L}_{FP} and $\mathcal{L}_{\text{FP}}^\dagger$ in Eqs. 2.24 and 2.26 are complex conjugates of each other. To prove this claim, we take the inner product between v_k and the corresponding

eigenfunction u_k of the adjoint operator:

$$\begin{aligned}
-\lambda_k \langle u_k | v_k \rangle &= \langle u_k | (-\lambda_k) v_k \rangle \\
&= \langle u_k | \mathcal{L}_{\text{FP}} v_k \rangle \\
&= \langle \mathcal{L}_{\text{FP}}^\dagger u_k | v_k \rangle \\
&= -\chi_k^* \langle u_k | v_k \rangle.
\end{aligned} \tag{2.34}$$

Thus, $\lambda_k = \chi_k^*$. In deriving the third step, we used the definition of adjoint of an operator (Eq. 2.27).

For overdamped dynamics driven by forces due to a potential, the eigenvalues of the FP operator are, in addition, real. To justify the claim, we observe that \mathcal{L}_{FP} can be written as a self-adjoint operator \mathcal{L} using a similarity transformation (Sec. 2.4.1, Eq. 2.66). The explicit derivation of the self-adjoint transformation is given in the supplementary information of this chapter. We also prove that since the expectation value of a Hermitian operator is real, \mathcal{L} is a real operator (Sec. 2.4.1, Eq. 2.72). Since similarity transformations preserve eigenvalues (but not eigenfunctions), the eigenvalues of \mathcal{L}_{FP} and \mathcal{L} are equal. Then, since the self-adjoint operator \mathcal{L} has real eigenvalues, so does \mathcal{L}_{FP} (Sec. 2.4.1, Eq. 2.74).

Finally, it is also straightforward to show that eigenfunctions u_k and v_k for different eigenvalues are orthogonal, i.e.,

$$\begin{aligned}
-\lambda_k \langle u_j | v_k \rangle &= \langle u_j | (-\lambda_k) v_k \rangle \\
&= \langle u_j | \mathcal{L}_{\text{FP}} v_k \rangle \\
&= \langle \mathcal{L}_{\text{FP}}^\dagger u_j | v_k \rangle \\
&= -\chi_j^* \langle u_j | v_k \rangle \\
&= -\lambda_j \langle u_j | v_k \rangle.
\end{aligned} \tag{2.35}$$

In the last line of Eq. 2.35, we have used $\lambda_j = \chi_j^*$. Thus, for $\lambda_k \neq \lambda_j$, $\langle u_j | v_k \rangle = 0$. We may normalize the functions according to

$$\langle u_j | v_k \rangle = \delta_{jk}, \tag{2.36}$$

where $\delta_{jk} = 1$ for $j = k$, else $\delta_{jk} = 0$.

2.2.3 Fokker-Planck equation with no drift

In the limit of vanishing drift coefficient and constant diffusion coefficient, Eq. 2.18 reduces to a partial differential equation describing the evolution of a Wiener process. The equation

for the transition probability $p(x, t) \equiv p(x, t | x' = 0, t' = 0)$ is then the diffusion equation

$$\frac{\partial p(x, t)}{\partial t} = D \frac{\partial^2 p(x, t)}{\partial x^2}, \quad (2.37)$$

with the initial condition

$$p(x, 0) = \delta(x). \quad (2.38)$$

The solution to Eqs. 2.37 and 2.38 is [183]

$$p(x, t) = \frac{1}{\sqrt{4\pi Dt}} \exp \left[-\frac{x^2}{4Dt} \right]. \quad (2.39)$$

Thus, the fundamental solution of the Fokker-Planck equation for a freely diffusing particle is a Gaussian distribution with time-dependent width.

2.3 Heat equation

Since the form of the Fokker-Planck equation is close to that of the classical heat-diffusion equation, it is worth noting some similarities in solutions to the latter.

Consider a one-dimensional thin rod of length l that runs from $x = 0$ to $x = l$. Assume that the sides of the rod are insulated so that the heat flow takes place only along the rod. Let $T(x, t)$ denote the temperature at position x and time t . Then $T(x, t)$ obeys the heat equation [185]

$$\frac{\partial T}{\partial t} = \kappa \frac{\partial^2 T}{\partial x^2} \quad \text{for all } 0 < x < l \text{ and } t > 0 \quad (2.40)$$

where $\kappa = K/c\rho$ is the thermal diffusivity in the wire, which has thermal conductivity K , specific heat c , and density ρ . As an example, we assume that the ends of the rod are maintained at temperatures $T(0, t) = T(l, t) = T_b$ and the initial temperature distribution is $T(x, 0) = f(x)$.

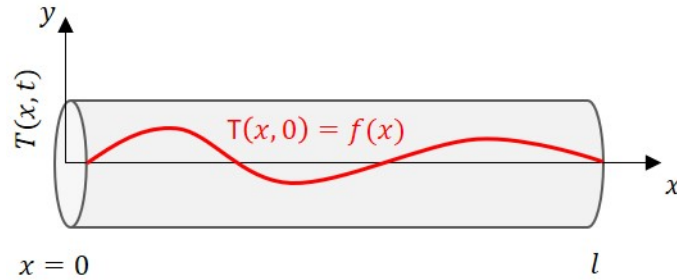


Figure 2.1: Heat transfer in a one-dimensional thin rod.

Since we have inhomogeneous boundary conditions, we cannot use separation of variables. We first find the steady-state temperature distribution $T_S(x)$ by solving

$$\frac{\partial^2 T_S(x)}{\partial x^2} = 0, \quad (2.41)$$

which implies

$$T_S(x) = T_b. \quad (2.42)$$

Now we introduce a function $v(x, t)$ that measures the difference between the temperature $T(x, t)$ and the steady-state value as

$$v(x, t) = T(x, t) - T_S(x). \quad (2.43)$$

It can be easily shown that $v(x, t)$ is a solution of the homogeneous equation

$$\frac{\partial v}{\partial t} = \kappa \frac{\partial^2 v}{\partial x^2}, \quad (2.44)$$

with boundary conditions $v(0, t) = v(l, t) = 0$ and initial condition $v(x, 0) = f(x) - T_S(x)$. Now, we use separation of variables and assume a solution to Eq. 2.44 of the form

$$v(x, t) = X(x)Y(t). \quad (2.45)$$

Inserting Eq. 2.45 into the heat equation gives

$$X(x)Y'(t) = \kappa X''(x)Y(t) \iff \frac{X''(x)}{X(x)} = \frac{1}{\kappa} \frac{Y'(t)}{Y(t)}. \quad (2.46)$$

The left-hand side depends only on x and the right-hand side depends only on t ; and the two sides are equal. We set both equal to some constant, σ . Thus, we have

$$X''(x) - \sigma X(x) = 0 \quad Y'(t) - \kappa \sigma Y(t) = 0. \quad (2.47)$$

For $\sigma \neq 0$, the general solution to Eq. 2.47 is

$$X(x) = Ae^{\sqrt{\sigma}x} + Be^{-\sqrt{\sigma}x} \quad Y(t) = Ce^{\kappa \sigma t} \quad (2.48)$$

for arbitrary A , B , and C . The boundary condition at $x = 0$ implies $A + B = 0$. So with $A = -B$, the condition at $x = l$ imposes

$$A(e^{\sqrt{\sigma}l} - e^{-\sqrt{\sigma}l}) = 0. \quad (2.49)$$

If $A = 0$, it would give a trivial solution $v(x, t) = 0$. So we must have

$$e^{\sqrt{\sigma}l} - e^{-\sqrt{\sigma}l} = 0 \iff e^{2\sqrt{\sigma}l} = 1 \iff 2\sqrt{\sigma}l = 2im\pi \iff \sigma = -m^2 \frac{\pi^2}{l^2} \quad (2.50)$$

for some integer m . Thus the overall solution is given as

$$\begin{aligned} v_m(x, t) &= X(x)Y(t) = A \left(e^{i\frac{m\pi}{l}x} - e^{-i\frac{m\pi}{l}x} \right) (C e^{-\kappa\pi^2 m^2 t/l^2}) = 2iAC \sin \left[\frac{m\pi}{l}x \right] e^{-\kappa\pi^2 m^2 t/l^2} \\ &= D_m \sin \left[\frac{m\pi}{l}x \right] e^{-\kappa\pi^2 m^2 t/l^2}, \end{aligned} \quad (2.51)$$

where the weights $D_m = -2iAC$ are determined by the initial conditions. If v_2, v_3, \dots are solutions to the Eq 2.40, then the principle of superposition states that $c_2 v_2 + c_3 v_3 + \dots$ is also a solution. Thus,

$$\begin{aligned} v(x, t) &= \sum_{m=2}^{\infty} v_{m-2}(x, t) \\ &= \sum_{m=2}^{\infty} D_{m-2} \sin \left[\frac{(m-2)\pi}{l}x \right] e^{-\kappa\pi^2 (m-2)^2 t/l^2}. \end{aligned} \quad (2.52)$$

Note that we begin the eigenfunction expansion at $m = 2$ to be consistent with the analogous expansion of the Fokker-Planck solution by Lu and Raz [186]. Finally, we use the initial condition $v(x, 0) = f(x) - T_S(x)$ to find D_{m-2} as

$$f(x) - T_S(x) = v(x, 0) = \sum_{m=2}^{\infty} D_{m-2} \sin \left[\frac{(m-2)\pi}{l}x \right]. \quad (2.53)$$

Using the orthogonality property of the eigenfunctions $\sin \left(\frac{(m-2)\pi}{l}x \right)$, we can obtain

$$D_{m-2} = \frac{2}{l} \int_0^l dx (f(x) - T_S) \sin \left[\frac{(m-2)\pi x}{l} \right]. \quad (2.54)$$

Then, the solution of Eq. 2.40 is

$$\begin{aligned} T(x, t) &= T_S(x) + \sum_{m=2}^{\infty} D_{m-2} \sin \left[\frac{(m-2)\pi}{l}x \right] e^{-\kappa\pi^2 (m-2)^2 t/l^2}, \\ &= T_b + \sum_{m=2}^{\infty} D_{m-2} \sin \left[\frac{(m-2)\pi}{l}x \right] e^{-\kappa\pi^2 (m-2)^2 t/l^2}. \end{aligned} \quad (2.55)$$

Thus, an extended system relaxes to equilibrium via an infinite set of modes. As $t \rightarrow \infty$, each mode exponentially converges to zero, and $T(x, t)$ reaches equilibrium temperature $T_S(x)$. For $m \geq 3$, the terms are exponentially smaller, and thus, the rate of cooling is determined by the first term, i.e., $m = 2$ of the infinite series.

Equation 2.55 shows that the temperature of the system, in general, depends on x and t in a complicated way, and there is no unique temperature that can be defined for such systems. However, in the mesoscopic case we focus on in this thesis, we describe a single particle through a probability distribution function $p(x, t)$. In this case, the equilibrium state of the system is characterized by a Boltzmann distribution. However, as the system cools to a lower temperature, the density $p(x, t)$ does not necessarily obey the Boltzmann distribution for intermediate times. Thus, the intermediate states of the system may not be characterized by a unique temperature. To observe the relaxation of such a system, a quantity that can measure the distance of the instantaneous state from the equilibrium state is required. In statistical physics, functions such as the L_1 distance and the Kullback-Leibler (KL) divergence are often used in these situations. In order to serve as a proxy for temperature, these distance functions should satisfy certain temperature-like properties [186]. A detailed discussion of these distance functions and their properties will be given in Chapter 4.

2.4 Supplementary information

2.4.1 A Similarity transformation of the Fokker-Planck operator

Here, we show that it is possible to transform the non-Hermitian Fokker-Planck operator \mathcal{L}_{FP} to a Hermitian form. Consider the Fokker-Planck equation

$$\frac{\partial p(x, t)}{\partial t} = \left[D \frac{\partial}{\partial x} \left(\frac{U'(x)}{k_B T} \right) + D \frac{\partial^2}{\partial x^2} \right] p(x, t) \equiv \mathcal{L}_{\text{FP}} p(x, t), \quad (2.56)$$

with arbitrary $U(x)$. Let us introduce a new function

$$\psi(x, t) = \frac{p(x, t)}{\sqrt{\pi(x)}}, \quad (2.57)$$

where $\pi(x)$ is the Boltzmann distribution:

$$\pi(x) = \frac{1}{Z} e^{-\frac{U(x)}{k_B T}} \quad \text{with} \quad Z = \int_{x_{\min}}^{x_{\max}} dx e^{-\frac{U(x)}{k_B T}}. \quad (2.58)$$

Then we have

$$\begin{aligned} p(x, t) &= \psi(x, t) \sqrt{\pi(x)}, \\ &= \frac{1}{\sqrt{Z}} \psi(x, t) e^{-\frac{U(x)}{2k_B T}}. \end{aligned} \quad (2.59)$$

Differentiating both sides, we get

$$\begin{aligned}\frac{\partial p(x, t)}{\partial x} &= \frac{1}{\sqrt{Z}} \frac{\partial \psi(x, t)}{\partial x} e^{-\frac{U(x)}{2k_B T}} + \frac{1}{\sqrt{Z}} \psi(x, t) \left[-\frac{U'(x)}{2k_B T} \right] e^{-\frac{U(x)}{2k_B T}}, \\ &= \frac{1}{\sqrt{Z}} e^{-\frac{U(x)}{2k_B T}} \left[\frac{\partial \psi(x, t)}{\partial x} - \frac{U'(x)}{2k_B T} \psi(x, t) \right].\end{aligned}\quad (2.60)$$

After differentiating both sides of Eq. 2.60 and rearranging terms, we get

$$\begin{aligned}\frac{\partial^2 p(x, t)}{\partial x^2} &= \frac{1}{\sqrt{Z}} e^{-\frac{U(x)}{2k_B T}} \left[-\frac{U'(x)}{2k_B T} \left(\frac{\partial \psi(x, t)}{\partial x} - \frac{U'(x)}{2k_B T} \psi(x, t) \right) \right] \\ &\quad + \frac{1}{\sqrt{Z}} e^{-\frac{U(x)}{2k_B T}} \left[\frac{\partial^2 \psi}{\partial x^2} - \frac{U'(x)}{2k_B T} \frac{\partial \psi(x, t)}{\partial x} - \frac{U''(x)}{2k_B T} \psi(x, t) \right], \\ &= \frac{1}{\sqrt{Z}} e^{-\frac{U(x)}{2k_B T}} \left[\frac{\partial^2 \psi(x, t)}{\partial x^2} - \frac{U'(x)}{k_B T} \frac{\partial \psi(x, t)}{\partial x} - \frac{U''(x)}{2k_B T} \psi(x, t) + \left(\frac{U'(x)}{2k_B T} \right)^2 \psi(x, t) \right].\end{aligned}\quad (2.61)$$

We can write Eq. 2.56 explicitly as

$$\begin{aligned}\mathcal{L}_{\text{FP}} p(x, t) &= \left[D \frac{\partial}{\partial x} \left(\frac{U'(x)}{k_B T} \right) + D \frac{\partial^2}{\partial x^2} \right] p(x, t), \\ &= D \frac{U''(x)}{k_B T} p(x, t) + D \frac{U'(x)}{k_B T} \frac{\partial p(x, t)}{\partial x} + D \frac{\partial^2 p(x, t)}{\partial x^2}.\end{aligned}\quad (2.62)$$

Inserting Eqs. 2.60 and 2.61 in Eq. 2.62 and simplifying the expression gives

$$\begin{aligned}\mathcal{L}_{\text{FP}} p(x, t) &= \sqrt{\pi(x)} \left[\frac{D}{2} \frac{U''(x)}{k_B T} - D \left(\frac{U'(x)}{2k_B T} \right)^2 + D \frac{\partial^2}{\partial x^2} \right] \psi(x, t), \\ &= \sqrt{\pi(x)} \mathcal{L} \psi(x, t),\end{aligned}\quad (2.63)$$

where the operator \mathcal{L} is given by

$$\mathcal{L} = \frac{D}{2} \frac{U''(x)}{k_B T} - D \left(\frac{U'(x)}{2k_B T} \right)^2 + D \frac{\partial^2}{\partial x^2}.\quad (2.64)$$

Since the second-derivative operator is Hermitian, \mathcal{L} is also Hermitian, i.e., $\mathcal{L} = \mathcal{L}^\dagger$. Using $p(x, t) = \sqrt{\pi(x)} \psi(x, t)$, Eq. 2.63 becomes

$$\mathcal{L}_{\text{FP}} p(x, t) = \pi(x)^{\frac{1}{2}} \mathcal{L} \pi(x)^{-\frac{1}{2}} p(x, t).\quad (2.65)$$

Comparing both sides, we get

$$\mathcal{L}_{\text{FP}} = \pi(x)^{\frac{1}{2}} \mathcal{L} \pi(x)^{-\frac{1}{2}} \implies \mathcal{L} = \pi(x)^{-\frac{1}{2}} \mathcal{L}_{\text{FP}} \pi(x)^{\frac{1}{2}}.\quad (2.66)$$

Using Eq. 2.56, we obtain the eigenvalue equation for $\psi(x, t)$

$$\frac{\partial \psi(x, t)}{\partial t} = \mathcal{L} \psi(x, t). \quad (2.67)$$

If $p(x, t) = \sqrt{\pi(x)} \psi(x, t)$, then $\psi(x, t)$ solves the eigenvalue problem of the operator \mathcal{L} with the *same* eigenvalues λ_k

$$\begin{aligned} \mathcal{L} \psi_k &= \pi_k^{-\frac{1}{2}} \mathcal{L}_{\text{FP}} \pi_k^{\frac{1}{2}} \psi_k, \\ &= \pi_k^{-\frac{1}{2}} \mathcal{L}_{\text{FP}} p_k, \\ &= -\pi_k^{-\frac{1}{2}} \lambda_k p_k, \\ &= -\lambda_k \pi_k^{-\frac{1}{2}} \pi_k^{\frac{1}{2}} \psi_k, \\ &= -\lambda_k \psi_k. \end{aligned} \quad (2.68)$$

In the fourth line, we substituted back $p_k = \pi_k^{\frac{1}{2}} \psi_k$. It is now easy to show that \mathcal{L} is a real operator [187]. The expected value of \mathcal{L} is defined as

$$\langle \mathcal{L} \rangle [\psi_k] \equiv \langle \mathcal{L} \rangle \equiv \langle \psi_k | \mathcal{L} \psi_k \rangle = \int dx \psi_k^* \mathcal{L} \psi_k. \quad (2.69)$$

The complex conjugate of the expected value of \mathcal{L} is then

$$\begin{aligned} \langle \mathcal{L} \rangle^* &= \int dx (\psi_k^* \mathcal{L} \psi_k)^*, \\ &= \int dx \psi_k (\mathcal{L} \psi_k)^*. \end{aligned} \quad (2.70)$$

Rearranging the factors in the integrand, we get

$$\langle \mathcal{L} \rangle^* = \int dx (\mathcal{L} \psi_k)^* \psi_k = \langle \mathcal{L} \psi_k | \psi_k \rangle. \quad (2.71)$$

Applying the definition of Hermitian operator

$$\begin{aligned} \langle \mathcal{L} \rangle^* &= \langle \psi_k | \mathcal{L} \psi_k \rangle, \\ &= \langle \mathcal{L} \rangle. \end{aligned} \quad (2.72)$$

Thus, $\langle \mathcal{L} \rangle$ is real. Furthermore, we can show that if an operator is real, its eigenvalues are real. Assume the operator \mathcal{L} has eigenvalues λ_k with eigenfunctions ψ_k :

$$\mathcal{L} \psi_k = -\lambda_k \psi_k. \quad (2.73)$$

We can compute again the expected value of \mathcal{L} in the state ψ_k :

$$\langle \mathcal{L} \rangle = \langle \psi_k | \mathcal{L} \psi_k \rangle = -\langle \psi_k | \lambda \psi_k \rangle = -\lambda_k. \quad (2.74)$$

From Eq. 2.72, the expected value of \mathcal{L} is real, and so are the eigenvalues λ_k .

Chapter 3

Optical Feedback traps

3.1 Feedback traps

Over the last three decades, optical tweezers [59, 188] have been used to exert piconewton forces on mesoscopic particles and detect their motion for physical [64–67], chemical [68, 69], and biological applications [63, 70–72]. Generalizations of tweezers such as optofluidic lattices [189, 190], plasmonic tweezers [191], and other techniques have been used to manipulate, sort and separate nanoparticles on nanometer scales [192]. In parallel with these applications of optical tweezers, feedback forces have been another way to trap particles and exert small forces. Although the details of such *feedback traps* vary, they share the common feature of operating in a cycle where one measures the position of a particle, calculates the desired trapping force, and then applies it (Fig. 3.1). Often the goal is simply to trap an object, a task that has been done using many different types of force for the feedback, including electrokinetic [111], magnetic [89], microfluidic flow [193], and thermophoretic forces [166]. The objects trapped have ranged from colloidal particles to bacteria to proteins and even to individual dye molecules diffusing in water [115]. Trapping allows one to measure, with good statistics, physical properties of individual objects [194]. In other situations, the goal is not simply to trap but to create a more-complicated force field, for example, a *virtual potential* that can be a discrete approximation to a physical potential [195], an idea that has been used to test fundamental aspects of statistical physics such as the relations between information and thermodynamics [119, 196], or the measurement of the functional form of the Gibbs-Shannon entropy function [197].

Feedback has been used previously in optical tweezers, but for relatively simple goals such as increasing the stiffness of the trap relative to its normal value. Simmons et al. [198] achieved a 400-fold gain in the stiffness using two-dimensional analog feedback control provided by a pair of orthogonal acousto-optic deflectors (AODs). Using similar setups based on digital feedback control, Ranaweera et al. [199] and Wallin et al. [200] achieved 29-fold and 10-fold gains in stiffness, respectively.

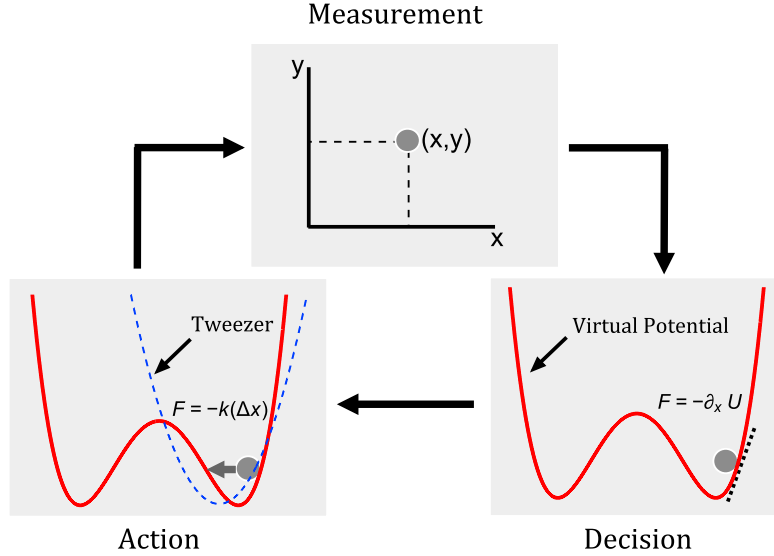


Figure 3.1: One cycle of the feedback trap. *Measurement*: estimate the current position of the particle, *Decision*: calculate force based on the imposed potential (red), and *Action*: apply the force by shifting the harmonic well center (blue). The force applied is a linear restoring force with k the stiffness of the harmonic trap and Δx the expected trap displacement.

Our goal is to create virtual potentials such as harmonic and double-well potentials. In previous studies on feedback traps [119, 195], such virtual potentials were created by applying electrokinetic forces, which are particularly well suited for applying strong forces to nanometer-scale particles [115]. Here, we substitute the electrokinetic forces with forces created by optical tweezers. A similar instrument was developed independently by Albay et al. [201]. In this chapter, we will describe the experimental setup for optical feedback tweezers. We will discuss how conventional optical tweezers can be used to create arbitrary potentials.

The content of this chapter has been published in three papers. The first version of the optical feedback tweezers was published in SPIE Proceedings [202]. Further extensions of the technique to create complex potentials such as double-well potentials and isotropic traps were published in Refs. [203, 204].

3.2 Principles of optical tweezers

The force exerted by an optical tweezer is classified into two scattering and gradient forces. *Scattering forces* arise due to momentum transfer from the photons to the particle and push

the particle along the light's propagation direction. *Gradient forces* arise from gradients in the electric field and act in the direction of increasing electric field strength.

The working principle of an optical trap can be explained in terms of ray optics or the electromagnetic interaction between the trapped particle and the trapping beam. Depending upon the size of a trapped particle (a bead of diameter d) trapped by a laser of wavelength λ , trapping forces can be calculated easily by using either ray optics (valid for $d \gg \lambda$) or a dipole approximation (valid for $d \ll \lambda$).

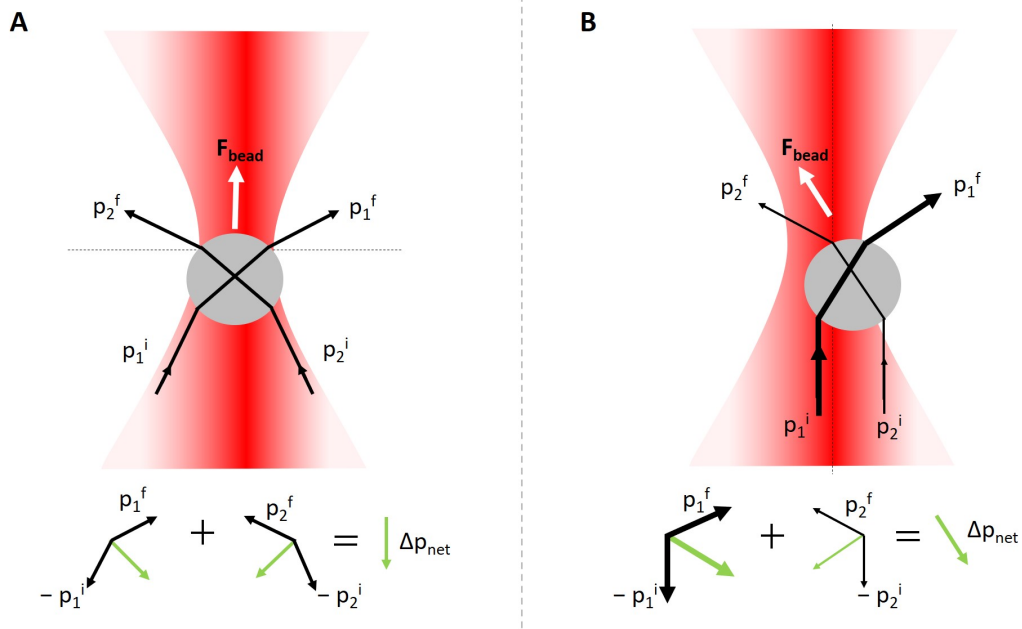


Figure 3.2: Working principle of optical tweezers based on ray optics. Because of the refraction of the light beam by the bead, the momentum of the light changes. The net change in momentum of light $\Delta \mathbf{p}_{\text{net}}$ results in a force exerted on the bead. If the bead is positioned below the focus, the beam pushes the particle towards the focus (**A**). If the bead is laterally displaced from the trap center, the gradient force results in a net force towards the center of the beam (**B**). Adapted from [182].

Ray optics describes the forces exerted on a particle in terms of changes in the momentum flux of the trapping beam [205]. According to Newton's third law, a reaction force acts on the bead in the direction opposite to the change in momentum of light. The reaction force pushes the bead either towards the beam or away from it. The force is attractive or repulsive, depending on the ratio $m = n_p/n_m$ of the refractive index of the particle (n_p) relative to the surrounding medium (n_m). For the attractive case, the particle acts as a positive lens. If the particle is at the beam's focus, individual rays of light refract symmetrically through the particle, resulting in no net lateral force. If the particle is "upstream" from the focus, it converges the beam more, and thus the momentum flux decreases. The change in momentum results in a force acting on the particle in the direction of beam propagation (Fig. 3.2A). Similarly, the force on the particle is opposite to the propagation of the beam

if it is downstream of the focus. However, if the particle is shifted sideways, there is a lateral gain in momentum towards the particle center. The reaction force acts towards the beam axis (Fig. 3.2B). Notice that we have neglected the effect of surface reflections and internal reflections. In practice, these reflections add to the downstream scattering force. Thus, apart from weakening the trap, the scattering force pushes the particle downstream, past the focus.

If the particle is much smaller than the wavelength of light, then the Rayleigh-scattering regime applies. The instantaneous electric field experienced by the particle in the electromagnetic field of light is uniform, and electrostatics can be applied for force calculation [206]. The particle, in this case, acts as a dipole particle with dipole moment given by

$$\mathbf{d}(\mathbf{r}, t) = 4\pi\epsilon_0 n_m^2 a^3 \left(\frac{m^2 - 1}{m^2 + 2} \right) \mathbf{E}(\mathbf{r}, t), \quad (3.1)$$

where ϵ_0 is the dielectric constant of the vacuum, a the radius of the particle, n_m the refractive index of the surrounding medium, and m the relative refractive index of the particle in the medium. As the electric field is oscillating, the induced dipole moment oscillates synchronously with the electric field and radiates secondary or scattering waves in all directions [206]. This scattering event changes both the magnitude and the direction of the energy flux of the electromagnetic wave. The corresponding momentum transfer also occurs, and the scattering force associated with these changes is exerted on the particle. The scattering force is given by

$$\mathbf{F}_{\text{scat}}(\mathbf{r}) = \left(\frac{n_m}{c} \right) C_{\text{scat}} I(\mathbf{r}), \quad (3.2)$$

where c is the speed of light in vacuum, $I(\mathbf{r})$ the intensity at position \mathbf{r} and $C_{\text{scat}} = \frac{8}{3}\pi(kr)^4 a^2 \left(\frac{m^2 - 1}{m^2 + 2} \right)^2$ the scattering cross-section with $k = 2\pi/\lambda$ the wavenumber of the trapping beam. The sign of the force is independent of the relative refractive index of the particle; thus, the scattering force always pushes the particle along the direction of the beam.

Because of the Lorentz force acting on a dipole in an electromagnetic field, a gradient force also acts on the particle in an optical trap. The instantaneous gradient force is defined by [206]

$$\begin{aligned} \mathbf{F}_{\text{grad}}(\mathbf{r}, t) &= [\mathbf{d}(\mathbf{r}, t) \cdot \nabla] \mathbf{E}(\mathbf{r}, t), \\ &= 4\pi n_m^2 \epsilon_0 a^3 \left(\frac{m^2 - 1}{m^2 + 2} \right) \frac{1}{2} \nabla E^2(\mathbf{r}, t). \end{aligned} \quad (3.3)$$

The steady-state gradient force is the time average of Eq. 3.3 and is given by [206]

$$\begin{aligned}
\mathbf{F}_{\text{grad}}(\mathbf{r}) &= \langle \mathbf{F}_{\text{grad}}(\mathbf{r}, t) \rangle_{\text{T}} , \\
&= 4\pi n_{\text{m}}^2 \epsilon_0 a^3 \left(\frac{m^2 - 1}{m^2 + 2} \right) \frac{1}{2} \nabla \langle \mathbf{E}^2(\mathbf{r}, t) \rangle_{\text{T}} \\
&= \pi n_{\text{m}}^2 \epsilon_0 a^3 \left(\frac{m^2 - 1}{m^2 + 2} \right) \nabla |E(\mathbf{r})|^2 , \\
&= \frac{2\pi n_{\text{m}} a^3}{c} \left(\frac{m^2 - 1}{m^2 + 2} \right) \nabla I(\mathbf{r}) , \tag{3.4}
\end{aligned}$$

where $\langle \mathbf{E}^2(\mathbf{r}, t) \rangle_{\text{T}} = \frac{1}{2} |E(\mathbf{r})|^2$ and $I(\mathbf{r}) = \frac{n_{\text{m}} \epsilon_0 c}{2} |E(\mathbf{r})|^2$. Thus, for $m > 1$, the gradient force attracts the particle towards the region with maximum intensity, and vice versa. For a Gaussian beam, the intensity distribution leads to $F_{\text{grad}} \propto -\Delta x$, to first order in the displacement Δx , a restoring force that acts as a Hookean spring.

In practice, the particle size usually falls in a regime where neither ray optics nor Rayleigh scattering is a good approximation. This size range, where the particle's dimensions are comparable to the wavelength of light, is often called the *resonance region* [207]. An exact electromagnetic theory is needed to determine the scattering of the trapping beam by the particle, and hence the optical force, based on either the Maxwell equations or the vector Helmholtz equation [208, 209]. The generalized Lorenz-Mie theory (GLMT), an extension of the Lorenz-Mie theory for a spherical particle under planar illumination, is used to model the trap for arbitrary illumination of an arbitrarily shaped particle [210–212]. Further exploration of GLMT needs a detailed calculation of the incident and scattered wave as a sum of vector spherical wavefunctions (VSWFs) to calculate the Mie coefficients. This rigorous treatment of electromagnetic theory is outside the scope of this thesis.

3.3 Optical tweezers setup

Our optical tweezer setup is based on a custom-built microscope constructed on a vibration-isolation table (Melles Griot) (Fig. 3.3). A linearly polarized 532 nm laser (Nd:YAG, Coherent Genesis MX STM-series, 1 Watt) is used for trapping and detection. The laser passes through a Faraday isolator (LINOS FI-530-2SV), which protects the laser cavity from back-reflections. We use a spatial filter (SF) consisting of a microscope objective and a pinhole to produce a clean Gaussian beam. The clean laser beam is separated into trapping and detection beams using a 90:10 beam splitter. The polarization of the detection beam is rotated by 90° with a half-wave plate to minimize any interference with the trapping laser. The trapping beam passes through an assembly of two acousto-optic deflectors (AODs) that provide orthogonal XY deflection (DTSXY-250-532, AA Opto Electronic). Each AOD can change the intensity in the first-order diffraction beam and steer its angle using ana-

log voltage-controlled oscillators (DFRA10Y-B-0-60.90, AA Opto Electronic). The trapping beam is then expanded by a factor of two to slightly overfill the back aperture of the microscope objectives. A pair of relay lenses images the steering point of the AOD onto the back focal plane of the trapping objective to translate beam rotation into linear motion in the trapping plane.

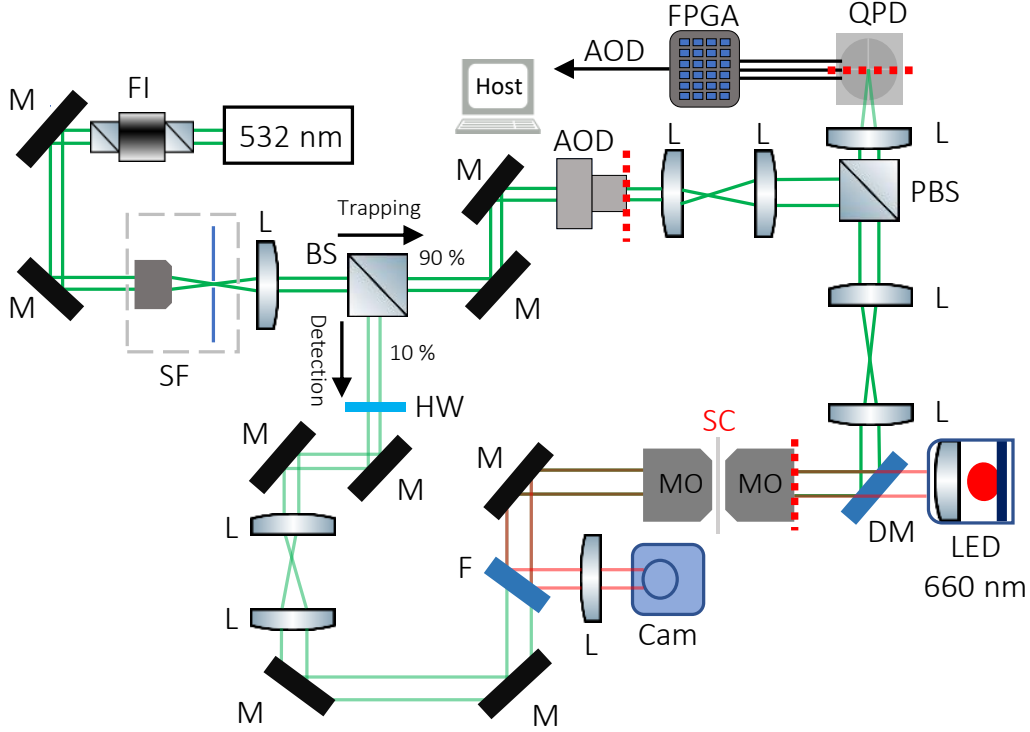


Figure 3.3: Schematic diagram of the feedback-trap setup. FI = Faraday Isolator, M = Mirror, SF = Spatial Filter, BS = Beam Splitter (non-polarizing), AOD = Acousto-Optic Deflector, L = Lens, MO = Microscope Objective, SC = Sample Chamber, PBS = Polarizing Beam Splitter, HW = Half-Wave Plate, F = Short-Pass Filter, QPD = Quadrant Photodiode, DM = Dichroic Mirror, PD = Photodiode, CS = Cover-Slip, Cam = Camera. Planes conjugate to the back-focal plane of the trapping objective are shown in red-dashed lines.

We use a water-immersion, high-numerical-aperture objective (Olympus 60X, UPlanSApo, $NA = 1.2$) for trapping a $1.5 \mu\text{m}$ diameter spherical silica bead (Bangs Laboratories). The detection beam enters through a low-numerical-aperture (40X, $NA = 0.4$) objective oriented opposite to the propagation of the trapping beam. The weakly focused detection beam minimizes trapping effects and extends the linear range for position detection [213, 214]. The trapping objective collects the forward scattered light from the detection beam. A polarizing beam splitter (PBS25-532-HP, Thorlabs) separates the detection beam and

the back-scattered light from the trapping laser by transmitting the former and reflecting the latter. We use a quadrant photodiode (QPD, First Sensor, QP50-6-18u-SD2) to detect the particle's fluctuations. The QPD is placed at the back focal plane of the trapping objective for back-focal-plane interferometry (see Sec. 3.3.3) [215]. A 660 nm LED (Thorlabs, M660L4) is used to illuminate the sample chamber. The illumination light is separated from the trapping laser before it enters the camera using a short-pass filter (cut-off wavelength ≈ 600 nm, Edmund Optics), which transmits wavelengths shorter than the cut-off wavelength of the filter. A LabVIEW-based FPGA data-acquisition system (NI 7855R) collects the voltage signals from the QPD and sends the command signals to AODs. The FPGA card runs the control protocol with a user-defined deterministic time step.

Having outlined the overall setup, we will now review the working principles of our setup's essential components, such as Faraday isolators, acousto-optic deflectors, and beam-position detectors.

3.3.1 Faraday isolator

A Faraday isolator is a device that transmits light in one direction while blocking the light in the opposite direction [216]. It is typically used to prevent unwanted feedback from back reflections into an optical oscillator, such as a laser cavity [217, 218]. These isolators are based on the *Faraday effect*, which is a first-order *magneto-optic* interaction. When a linearly polarized light is passed through a material placed parallel to a magnetic field, the plane of polarization of the emergent light is rotated by an angle θ that is proportional to the thickness d of the sample and the strength of the magnetic field B , according to the relation [216],

$$\theta = VBd, \quad (3.5)$$

where V is the *Verdet constant*, which depends on both the temperature and the wavelength.

For a given material, the sense of rotation is independent of the propagation direction of light. The repeated forward and backward propagation has a cumulative effect on the rotation angle. Typically, a Faraday isolator consists of three components: an input polarizer, a Faraday rotator, and an output analyzer. As shown in Fig. 3.4, incident light enters an input polarizer, which polarizes the otherwise unpolarized light. Upon passing through the Faraday rotator, the plane of polarization is rotated by 45° . When the back-reflection at 45° passes through the rotator, the polarization axis is further rotated by 45° . Thus, the back-reflection, polarized in the horizontal plane, is either absorbed or reflected by the input polarizer. As a result, Faraday isolators prevent beam reflections from returning to the laser cavity. Inside the cavity, interference between the delayed reflected beam and the laser field can destabilize the laser cavity, leading to large unwanted intensity oscillations [217, 218].

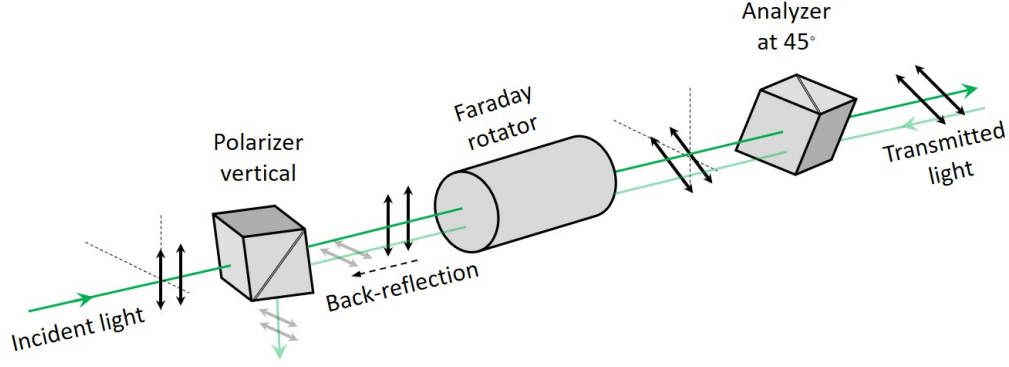


Figure 3.4: Schematic diagram of the Faraday isolator. A Faraday rotator placed between a polarizer-analyzer pair prevents the back-reflection (light green) of the incident light (green) from entering the laser cavity. Adapted from [216].

3.3.2 Acousto-optic deflector

The basic principles of acousto-optic devices are based on the scattering of light by the periodic index variations generated by an acoustic wave in the supporting medium. These periodic variations form a moving index grating, generated by a traveling acoustic wave, or a standing index grating, generated by a standing acoustic wave. Typically, the size of these grating periods ranges from the order of $1\text{ }\mu\text{m}$ to a few centimeters. The grating period in our setup is $\approx 9\text{ }\mu\text{m}$. The period and the modulation depth of these gratings can be varied by varying the frequency and amplitude of the acoustic wave, respectively.

Figure 3.5 shows a typical configuration of an acousto-optic deflector. A preamplified signal is sent through a transducer attached at the bottom of the device to launch an acoustic wave of frequency f_a . Upon interaction with the gratings set up by the acoustic wave, the incident light is scattered by the periodic modulation of refractive index along the propagation direction of the acoustic wave. If the interaction length is sufficiently long, and the laser beam is incident at the Bragg angle $\theta_B = 0.5\lambda/\Lambda_a$, with Λ_a the wavelength of the acoustic wave, the deflection angle for the first-order light is given by

$$\theta_d = \frac{\lambda f_a}{2nv_a}, \quad (3.6)$$

where λ is the wavelength of the incident light, n the refractive index of the traveling medium, and v_a the acoustic wave velocity. In the configuration shown in Fig. 3.5, an acoustic absorber helps create traveling acoustic waves inside the crystal. Thus, the density modulation is $\rho(x) \sim e^{i\kappa x}$ along the propagation direction, where $\kappa = 2\pi/\Lambda_a$. The Bragg condition is then satisfied for $m = 0$ and $+1$ only. Using Eq. 3.6, we observe that, for a fixed angle of incidence, the deflection angle can be controlled through the acoustic wave frequency. For a given acoustic frequency f_a , when the angle of incidence is equal to the Bragg angle, i.e., $\theta_i = \theta_B$, the first-order efficiency is maximum.

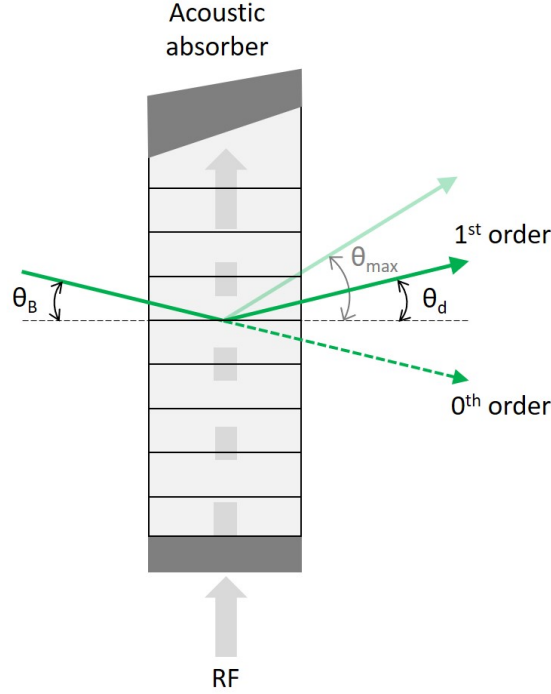


Figure 3.5: Schematic diagram of an acousto-optic deflector. When a light beam is incident at an angle θ_B , the first-order diffracted beam is produced at an angle θ_d . The maximum deflection angle θ_{\max} is determined by the RF frequency sent to the piezo-transducer, bonded to the crystal. The crystal is typically skew cut and fitted with an acoustic absorbing material on the opposite end to avoid reflection of the acoustic wave back into the crystal.

The acousto-optic crystal is made up of TeO_2 , and the acoustic wave velocity through the medium is $v_a = 650$ m/s. The variation of the diffraction efficiency upon changes in the acoustic frequency shows that the Bragg condition is met near the central frequency (75 MHz) of the acoustic range (50 MHz) (Fig. 3.6). The maximum efficiency is $\approx 73\%$, near the middle of the scan voltage. The AOD modulation that corresponds to the maximum efficiency indicates the matching of Bragg's criterion for diffraction. The approximately flat plateau in the AOD-calibration graph indicates that the output efficiency of the device does not change much during steering of the beam through small angles about the Bragg angle.

The deflection of the first-order beam is not instantaneous. Since it takes a finite amount of time for an acoustic wave to travel through the laser beam, the switching between different angles takes time. This settling time is called the *rise time* and given as

$$T_R = \Omega \frac{\phi}{v_a}, \quad (3.7)$$

where Ω is a constant depending on the laser beam profile, ϕ the beam diameter, and v_a the acoustic velocity. For a beam diameter of 3 mm and $\Omega = 0.66$ (TEM_{00}), the rise time is ≈ 3 μs . Other scanning strategies include galvanometer mirrors, piezoelectric mirrors,

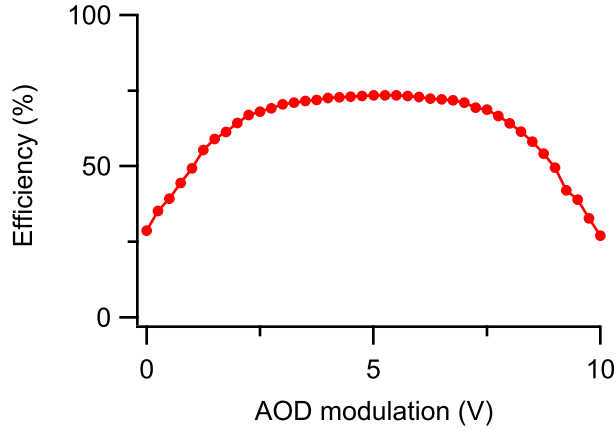


Figure 3.6: Diffraction efficiency of the acousto-optic deflector. The ratio of power in the first-order beam to incident power changes as the beam is steered at different angles by changing the AOD modulation voltage. The modulation voltage changes the acoustic wave frequency through a voltage-controlled oscillator (VCO) driver. For a given incident angle of the incoming beam, the Bragg diffraction depends on the acoustic wave frequency.

and electro-optic deflectors [219]. Scanning mirrors are typically slow, with response $\gtrsim 100$ μ s. However, a response time of about 1 μ s can be achieved using electro-optic deflectors (EODs) [220]. Although EODs have lower deflection-angle errors and higher linearity in deflection angle than AODs, their higher cost and smaller deflection angle (≈ 20 mrad vs. ≈ 40 mrad) limit their use in a typical optical-tweezer setup [221].

3.3.3 Detection scheme

Once a bead is trapped, we need to detect its motion. We use an interferometry-based detection scheme to detect the particle position. Interferometric detection can provide high spatial and temporal resolution — angstroms and microseconds, respectively. The interference signal is monitored with a quadrant photodiode (QPD) positioned along the optical axis at a plane conjugate to the back focal plane (BFP) of the condenser [215]. The intensity pattern in the BFP does not depend on the position of the trapping beam focus, and the pattern in the BFP represents the angular-intensity distribution of the interference between the forward-scattered light from the trapped bead and the unscattered light.

The laser-based detection scheme uses a low-power laser (taken from the trapping beam) with polarization rotated to be orthogonal to that of the trapping beam. The trapping beam is dynamically shifted to provide feedback forces. Under such circumstances, it is necessary to decouple the detection beam from the trapping beam to simplify the position measurements. It should be noted that the detection laser is introduced through a low-numerical-aperture objective to create a wide detection spot that enlarges the linear range for position

detection (Fig. 3.7) [213, 214]. We also do a nonlinear calibration of the position signal obtained from QPD to further extend the range of the position-detection measurements.

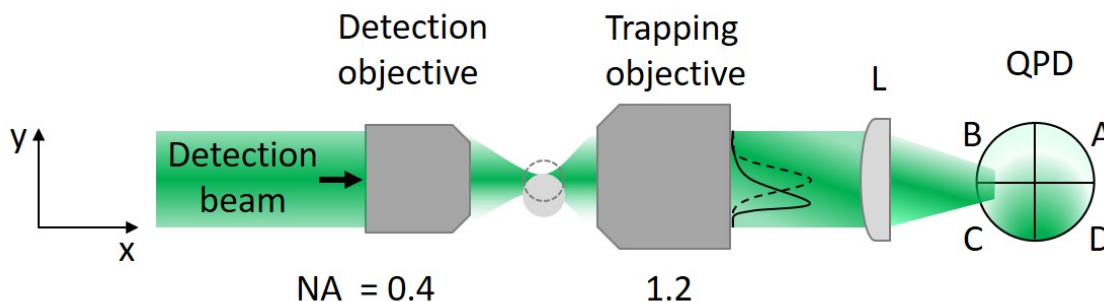


Figure 3.7: Interferometry-based detection scheme. The interference between the unscattered and scattered light is collected by the trapping objective in the forward direction. The interference signal is monitored with a QPD placed at a plane conjugate to the back focal plane of the trapping objective.

The light pattern on the QPD is converted to an electrical signal readable by a data-acquisition system. A QPD is a set of four identical P or N silicon photodiodes separated by a small gap. When light is incident on the detector, a photocurrent is detected by each photodiode (labeled A, B, C, and D in Fig. 3.7). The output voltages are obtained by routing the photocurrents from each quadrant into current-to-voltage amplifiers. Thus the QPD circuit provides three signals V_x , V_y , and V_z as

$$\begin{aligned} V_x &= (V_B + V_C) - (V_A + V_D) , \\ V_y &= (V_A + V_B) - (V_C + V_D) , \\ V_z &= V_A + V_B + V_C + V_D. \end{aligned} \tag{3.8}$$

Often the X and Y signals are normalized by dividing the sum signal V_z to reduce the dependence of the output on the light intensity. We have used a standard silicon QPD (QP50-618u-SD2) from First Sensor. Operating with zero bias, the detector has a bandwidth ≈ 150 kHz.

3.3.4 Control and data acquisition

As we discussed in Sec. 3.3.2, the trap's position is controlled by repositioning the laser focus in the trapping plane by an AOD. The acquisition of particle position in the trap and generation of control signal requires a controller. We use a LabVIEW-based field-programmable gate array (FPGA) data-acquisition system to receive signals and send control commands.

An FPGA has a finite number of hardware resources such as programmable logic, I/O, and memory resources [222–224]. Contrary to a processor or a microcontroller, these limited resources often constrain FPGAs in storage. These resources are located at regular intervals

across the chip, which allows for short paths between the resources. These short paths reduce the minimum execution time of a code on the FPGA target. Since there are multiple instances of each resource on an FPGA, multiple concurrent (parallel) processes can run on the same device simultaneously while minimizing resource conflicts. Another benefit of an FPGA-based acquisition device is the precise and deterministic time of sampling. The precise timing set by the hardware control is important to digital protocols and high-speed control applications because it can affect a system’s ability to communicate or the stability of the controlled system.

For a typical application, we need two parts of the controller program (code): one runs on the target, and the other runs independently on the host. In the target version, one downloads the actions such as input acquisitions, calculation of control signals, and generation of output signals. An FPGA must receive configuration instructions before it can perform any computation. The compiler generates configuration instructions for the FPGA that implements the written code. After the compilation, the compiler arranges the programmable resources on the FPGA to create a circuit that performs the designed actions. On the other hand, the host program, running on a standard computer, intermittently sends and receives signals from the target device. The transfer of signal takes place through direct memory access (DMA) communication, consisting of two DMA first-in-first-out (FIFO) buffers: one FIFO on the host computer and the other on the FPGA target. Our 7855R controller has three DMA channels that provide high-throughput and lossless data transfer at the 100 kHz rates used.

3.4 Sample preparation

We trap a colloidal particle diffusing in water. The sample chamber consists of a 1-mm-thick glass slide and a coverslip (25 mm \times 25 mm, No. 1.5). We use a 100- μ m-thick spacer wire (black lines in Fig. 3.8) to create a small volume, \approx 60 μ l. We begin by applying two parallel stripes of nail polish and placing two straight spacer wires. A coverslip is put on the wires by applying gentle pressure.

We place the assembly in an oven at 60°C to dry the nail polish quickly. After it has dried, we pipette \approx 40 μ l of a dilute bead solution in deionized water. Finally, we seal the remaining sides with nail polish and leave it to dry at room temperature. The sample chamber is mounted on a compact dovetail linear stage (DS25-XYZ, Newport) for three-dimensional positioning.

3.5 Calibration

To create dynamics that can be quantitatively measured requires a careful chain of calibration. First, using the camera as a length standard, we calibrate the image pixel size. Next, we calibrate the trap displacement produced by a change in the modulation voltage in

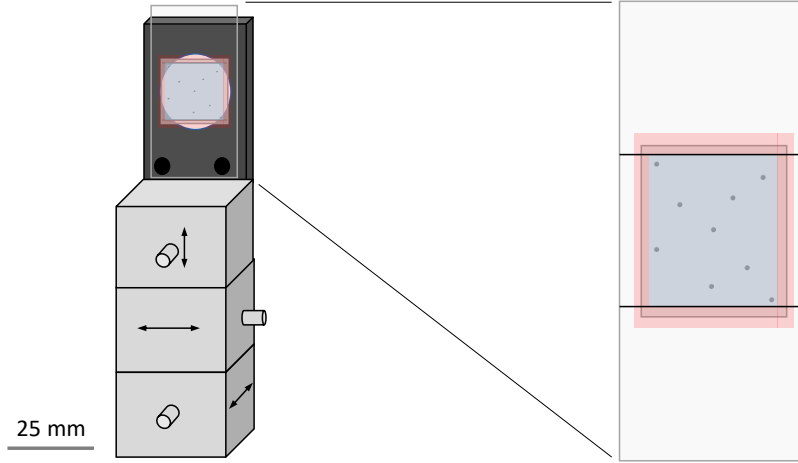


Figure 3.8: Schematic of the sample chamber. A chamber containing silica beads is mounted on an assembly of linear stages for three-dimensional manipulation.

the AOD. Having determined the camera and AOD calibration constants, we calibrate the response of the QPD against the AOD modulation voltage. Finally, we calibrate the force exerted by the trap on the particle. The calibration process for QPD and force has to be repeated each time before measurement. We will now discuss the step-by-step calibration procedure performed each time before an experiment.

3.5.1 Position calibration

A three-step calibration maps the voltage signals produced by the QPD (V) to displacement (μm). We first calibrate the camera using a standard micrometer scale. Using ImageJ (<https://imagej.nih.gov/ij/index.html>), we found that the average size of one pixel is 79.0 ± 0.4 nm. We then calibrate the AOD by discretely moving the trap position and recording the image of the trapped bead. Figure 3.9 shows the response of the AOD for the change of the modulation voltage. We explored either side of the trap center by varying the modulation voltage from -0.1 to $+0.1$ V, and the trap displacement in μm was measured from the displacement of the image on the camera. This is a one-time calibration for the AOD, provided there is no change in the optics of the experiment.

Once we calibrate the camera and AOD, we also need to calibrate the response of the QPD against the AOD modulation voltage. Figure 3.10A shows a typical response of the QPD as a function of trap displacement. The response of the QPD is linear only over a very small region (≈ 350 nm) around the trap center (indicated by the region between dashed-vertical lines). Although the AOD is linear over a relatively large range, the small range of linear response of the QPD limits the accuracy of the linear feedback algorithms used by the feedback traps. A nonlinear calibration is required for larger trap displacements.

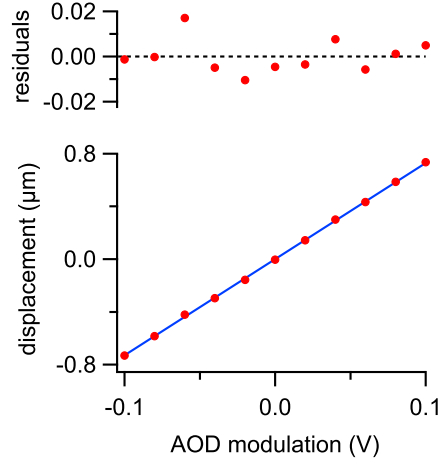


Figure 3.9: Calibration of the AOD. The modulation voltage is varied from -0.1 V to $+0.1$ V (≈ 1.6 μm) to calibrate the AOD using a camera.

For the nonlinear calibration (NLC) of the QPD signal, we fit a 5th-order polynomial to the QPD response (Fig. 3.10B). Once the fit parameters are obtained, we feed the QPD signal through the fit equation (now with known parameters) to remove the nonlinearity from the QPD signal. Figure 3.11 shows the QPD signal after the NLC. Although the calibration procedure works well, it is susceptible to drifts in the system. To reduce these effects, we developed a routine in LabVIEW to automate the NLC procedure in our experiment. The calibration process is repeated whenever we move the sample chamber or trap a new particle

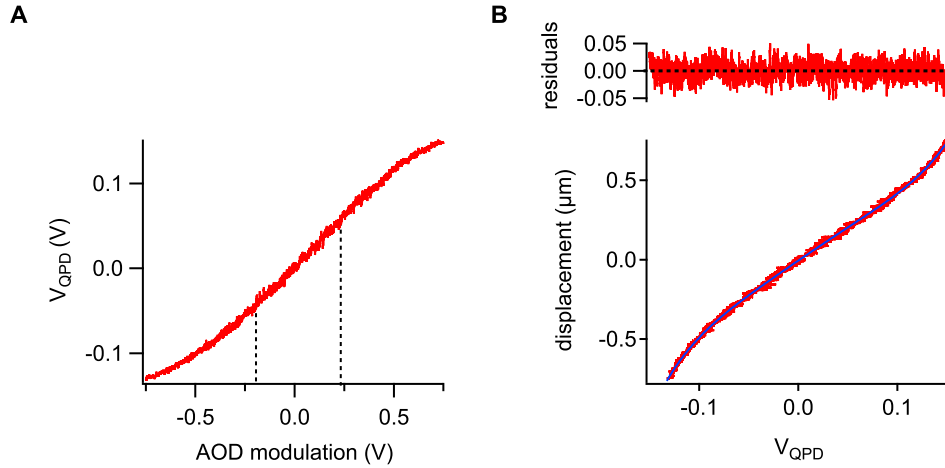


Figure 3.10: Calibration of the QPD signal. **A.** The signal from QPD for small displacement about the center of the detection beam varies non-linearly. Dashed vertical lines indicate region of approximately linear response. **B.** Nonlinear fit of the QPD signal to a 5th-order polynomial.

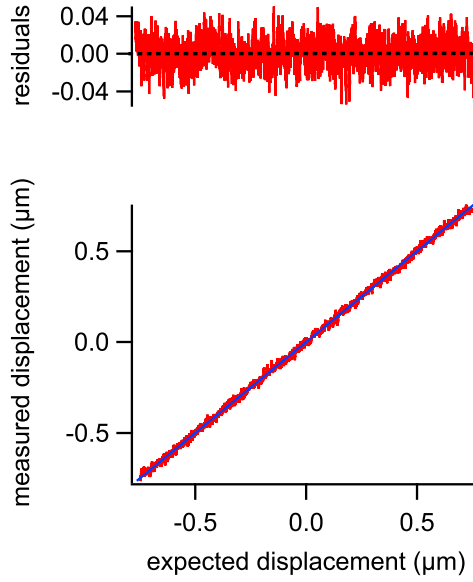


Figure 3.11: Expected displacement vs. measured displacement. A nonlinear calibration linearizes the measured displacement signal shown in Fig. 3.10B. The superimposed solid blue line is a plot of $y = x$ (with no curve fitting). The root-mean-square error of the residuals is 1.3%.

to avoid errors caused by instrument drift ($\approx 1 \text{ nm s}^{-1}$) or bead-size variations. Note that separate calibration protocols are needed for X and Y directions.

3.5.2 Trap-stiffness calibration

Once the trap position is calibrated, we need to calibrate the stiffness of the trap. The standard calibration method in optical tweezers is the power spectral analysis of the Brownian motion of the trapped particle [170]. The power spectral density (PSD) of a variable $x(t)$ is defined as the expectation value of the squared modulus of its Fourier transform. The Einstein-Ornstein-Uhlenbeck theory predicts a Lorentzian spectrum for an overdamped Brownian particle (Eq. 2.17) [181]. However, in practice, the trajectory $x(t)$ is sampled with frequency $f_s = \Delta t^{-1}$, which causes *aliasing*. In other words, the sampling process cannot distinguish frequency components of the signal that differ from each other by integer multiples of the sampling frequency: They all add up to a single amplitude. However, in our setup, the bandwidth of the signal is limited to $\approx 150 \text{ kHz}$ by the detector (QPD) and the signal is sampled at 100 kHz by the data acquisition device¹. Since the corner frequency $f_c = k/2\pi\gamma \approx 300 \text{ Hz}$ of the trap is sufficiently below the Nyquist frequency

¹In a more careful setup, I would have used either a sampling rate around 300 kHz or an antialiasing filter with a bandwidth of 50 kHz . However, in this case, the signal is so attenuated and the electronic noise so small that these steps were not necessary.

($f_{\text{Nyq}} = f_s/2 \approx 50$ kHz), the power attenuates by approximately four orders of magnitude for frequencies near f_{Nyq} . We thus do not expect significant aliasing in our signals. Our model then ignores the aliasing effects from the detector. However, a more careful analysis of the power spectrum that accurately accounts for aliasing can be done by including the response function of the detector [170].

The Langevin equation for a discretely sampled position $x(t)$ is given as (see Chapter 2) [170]

$$x_{i+1} = c x_i + \Delta x \eta_i, \quad (3.9)$$

with $\langle \eta_i \rangle = 0$ and $\langle \eta_i \eta_j \rangle = \delta_{ij}$ for all i, j , where δ_{ij} is the Kronecker delta function ($\delta_{ij} = 1$ for $i = j$, 0 otherwise). The expectation $\langle \dots \rangle$ is an average with respect to the ensemble of realizations of the stochastic variable η_i . The η_i are independent Gaussian random numbers with zero mean and unit variance. The remaining terms c and Δx can be calculated by integrating the Langevin equation over a time interval $\Delta t = f_s^{-1}$, to find

$$c = \exp(-\pi f_c / f_{\text{Nyq}}), \quad (3.10)$$

and

$$\Delta x = \left(\frac{(1 - c^2)D}{2\pi f_c} \right)^{1/2}. \quad (3.11)$$

Taking the discrete Fourier transform of Eq. 3.9, we obtain [170]

$$S_k = \langle |\hat{x}_k|^2 / \tau \rangle = \frac{(\Delta x)^2 \Delta t}{1 + c^2 - 2c \cos(2\pi k \Delta t)}, \quad (3.12)$$

where \hat{x}_k is the discrete Fourier transform of x_k sampled for a time τ .

Figure 3.12B is a typical power spectral density of a trapped bead's position $x(t)$ (Fig. 3.12A) sampled at $\Delta t = 10$ μ s. We fit the experimental PSD with Eq. 3.12 to estimate the values of D and f_c . The corner frequency divides the spectrum into two regimes. For frequency $f \ll f_c$, the power spectrum is constant, indicating suppressed motion of the particle. For $f_{\text{Nyq}} \gg f \gg f_c$, the power spectrum decreases approximately as $1/f^2$, indicating free diffusion. The power spectrum has been averaged over $n = 50$ non-overlapping intervals (also known as blocking) to reduce the noise ($\text{PSD}_{\text{noise}} = S_{\text{avg}}/\sqrt{n}$) in the PSD [225]. The accurate estimation of k requires accuracy in both D and f_c . As we use a least-square fitting to estimate these parameters, we get a systematic bias in D : The least-squares fitting method assumes that the weights are uncorrelated with the experimental data. However, we use experimental ($\text{PSD}_{\text{noise}}$) as weights for the fitting. As Nørrelykke and Flyvbjerg

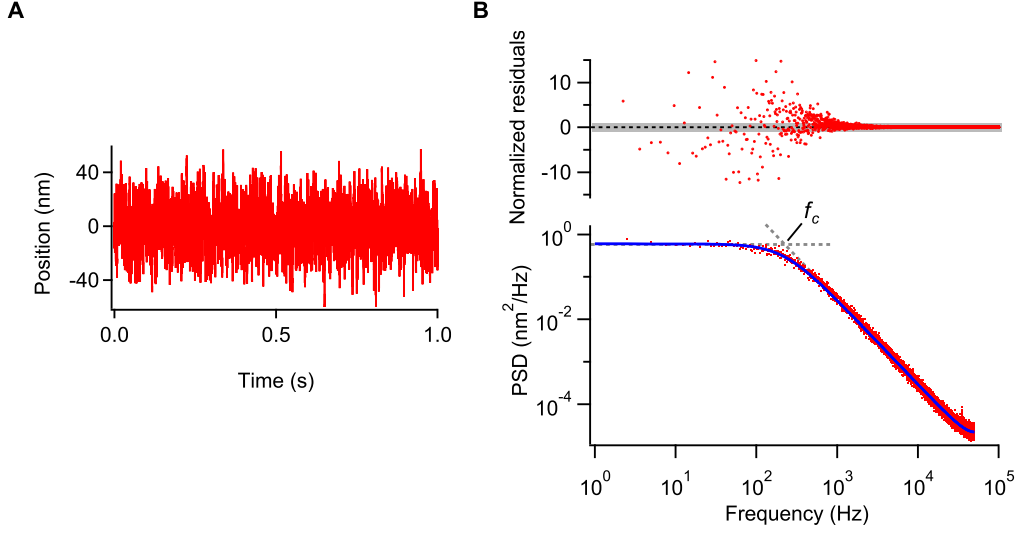


Figure 3.12: Calibration of trap stiffness. **A.** Time series of the position of a trapped particle. **B.** Power spectrum of a trapped bead. The blue line is a fit to the aliased Lorentzian (Eq. 3.12). The corner frequency measured from the fit is $f_c = 236 \pm 2$ Hz. The reduced chi-squared value $\chi_\nu^2 \approx 1.02$, where $\nu = 19998$. The shaded gray region in the normalized residual plot indicates one standard deviation (1σ) from the mean.

calculated, we multiply Eq. 3.12 by the factor $= n/(n - 2)$, which approximately removes the bias in the estimate of D [225].

Because the Brownian particle is in thermal equilibrium with the bath, its probability distribution follows the Boltzmann distribution given by [226]

$$\pi(x) = \frac{1}{Z} \exp \left[\frac{-U(x)}{k_B T} \right], \quad (3.13)$$

where $Z = \int dx e^{-U(x)/k_B T}$ normalizes the probability distribution. By solving Eq. 3.13 for $U(x)$, we obtain

$$U(x) = -k_B T \ln [\pi(x)] + U_0, \quad (3.14)$$

where $U_0 = -k_B T \ln Z$. Figure 3.13**A** represents a frequency estimate of the probability for a measured position x at a time t to fall within the interval $[x_i, x_{i+1})$, where $x_i = i\Delta x$, with Δx the bin width. Figure 3.13**B** represents the potential energy obtained from the probability distribution $p(x)$. Assuming $U = \frac{1}{2}kx^2$, we can fit either the probability distribution or the potential with appropriate function to obtain the trap stiffness k . The determination of the potential by this method is subjected to systematic errors due to uncorrelated noise such as low-frequency mechanical drift in the setup and detection errors.

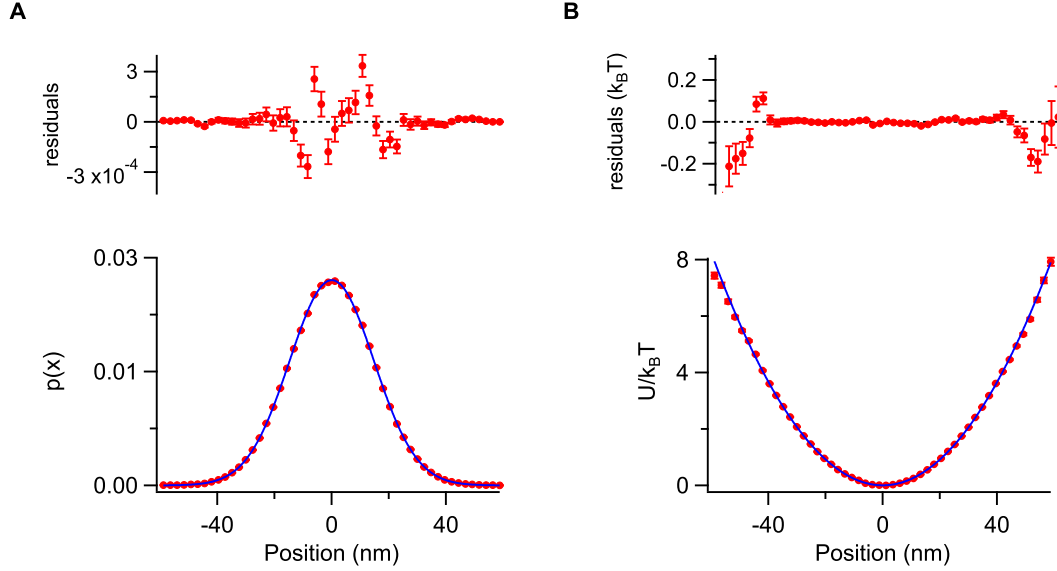


Figure 3.13: Potential and equipartition analysis. **A.** Position histogram and **B.** potential corresponding to the data shown in Fig. 3.12. The red markers are the experimental data, and solid blue lines are fits using Eq. 3.13 and Eq. 3.14, respectively. Values of trap constants measured from the fits are $k = 19.05 \pm 0.18$ and 19.02 ± 0.21 pN/ μm for **A** and **B**, respectively.

If the trap is harmonic and the measurement errors are $\ll \sigma_x$, a simple theory based on the equipartition theorem can give the stiffness as

$$k = \frac{k_B T}{\sigma_x^2}, \quad (3.15)$$

where σ_x^2 is the position variance. The equipartition method is independent of the particle's shape or size; however, this method requires a calibrated detection system and removal of measurement noise; i.e., $\sigma_x^2 = \sigma_{\text{tot}}^2 - \sigma_{\text{meas}}^2$, where σ_{tot}^2 is the total variance and σ_{meas}^2 the measurement variance of the signal.

Other passive techniques, such as mean-squared displacement, autocorrelation analysis, and step response, are often used to estimate the stiffness of optical traps [99, 198, 227]. Active calibration techniques include estimating the trap stiffness from the displacement of a trapped particle caused by a fluid flow. A power spectral density of an oscillating particle in a fluid has been used to calibrate both position and stiffness simultaneously [228]. In our experiment, we require very good estimates of D and k to accurately apply feedback forces on the trapped particle to impose arbitrary potentials. Some of the methods described above are affected by low-frequency drifts and noise. Frequency-domain analysis permits one to remove these sources of noise; for these reasons, power spectrum analysis is a reliable method to calibrate optical tweezers. The spectral analysis has also been generalized to include hydrodynamic effects [170]. When a rigid body moves through a dense fluid, the friction

acting on the body moving in an infinitely deep fluid depends on the body's past motion and can be obtained from the Navier-Stokes equation [229]. However, in practice, a particle in a trap is near a surface, and the hydrodynamic interaction between the microsphere and the surface must be accounted for. The effect of the finite depth of the fluid can be addressed by considering Faxén's correction for the drag coefficient [230]. To reduce the hydrodynamics effect in our experiment, we trap beads at a depth of $\approx 50 \text{ }\mu\text{m}$ ($h/r \approx 30$) from the surface. The hydrodynamic interaction with the surface has an effect of $\approx 2\%$. We do account for this error in our analysis.

With all the requirements of a feedback trap and the calibration protocols, we are ready to implement the apparatus to create virtual potentials. In the next few sections, I will outline the technical applications of our setup.

3.6 Virtual harmonic potential

As shown in Fig. 3.1, force is exerted by moving the trap center relative to the beam. The force required at a position x_n is calculated by evaluating the spatial derivative of the potential at x_{n-1} , using $F_n = -U'(x_{n-1})$, where $U(x)$ is the potential to be imposed and $U'(x) = d_x U$. These forces generated by an optical tweezer are approximated as $F_n = \beta x_n$, where β is a proportional feedback constant. The dimensionless feedback constant can also be expressed as $\beta = \Delta t/t_r$, where t_r is the relaxation time of the corresponding physical potential [118]. Unlike a real potential, where forces are applied continuously as the particle changes, feedback traps apply forces once per cycle. Thus, although the β in a feedback trap is similar to the force constant in a real harmonic potential, it can affect the dynamics of the particle differently. For $\beta \ll 1$, the dynamics of the particle in a virtual trap are similar to dynamics in a real potential and obey the equipartition theorem [118]. For a total delay $t_d \approx 2\Delta t$ (characteristic of our setup), the discrete dynamics of the particle in a virtual potential created by optical tweezers follows

$$\begin{aligned} x_{n+1} &= x_n - \tilde{\beta}(x_n - x_n^t) + \xi_n \\ x_n^t &= \bar{x}_n(1 - G) \\ \bar{x}_n &= x_{n-2} + \xi_n^m, \end{aligned} \tag{3.16}$$

where x_n is the true position of the particle, \bar{x}_n the observed position, x_n^t the trap position at time t_n and ξ_n and ξ_n^m reflect integrated thermal and measurement noise [231]. The gain $G = k_v/k_t$ is the ratio of stiffnesses of the desired virtual feedback trap to the usual tweezer force constant. Notice that $G = 1$ implies placing the trap at $x = 0$: this is the usual operation of optical tweezers. The trap constant $\tilde{\beta} = (k_v/\gamma)t_r[1 - \exp(-\Delta t/t_r)]$ is dimensionless and reflects the relaxation in the tweezer during the feedback-loop update time interval Δt with relaxation time $t_r = \gamma/k_t$. Here, $\gamma \approx 6\pi\eta r$ is the Stokes-Einstein friction

coefficient for a particle of radius r in a fluid of viscosity η . For $\Delta t \ll t_r$, $\tilde{\beta} \approx (k_v/\gamma)\Delta t \equiv \beta$, the usual result for constant-force feedback traps. For $\Delta t \gg t_r$, we have $\tilde{\beta} \approx (k_v/\gamma)t_r$. We operate the trap in the first limit, with $\Delta t = 10 \mu\text{s}$ and $t_r \approx 0.8 \text{ ms}$, so that $\tilde{\beta} \approx \beta \approx 0.01$. The feedback delay time, including the delay from the AOD electronics ($10 \mu\text{s}$), is $t_d = 20 \mu\text{s} \approx 2\Delta t$.

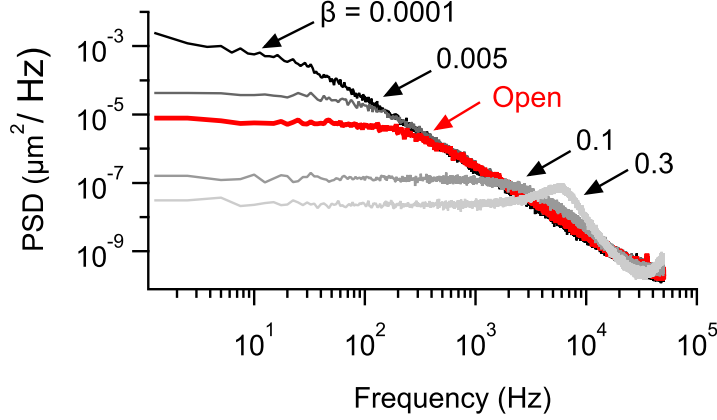


Figure 3.14: Power spectral density for different values of proportional feedback gain ($\beta = \Delta t/t_r$). The power spectrum for the “natural” trap without feedback (“open-loop”) is shown in red. Feedback can create both weaker and stiffer traps. The corresponding values of trap stiffness (excluding $\beta = 0.3$) are 1.36 ± 0.05 , 7.33 ± 0.11 , 19.84 ± 0.16 , and $243 \pm 0.49 \text{ pN}/\mu\text{m}$, respectively.

In Figure 3.14, we show that the feedback trap can alter the effective stiffness k of the virtual potential. We obtained a 30-fold gain in the stiffness of the trap compared to that of the underlying harmonic trap. Often changes in trap stiffness are created by varying the total laser intensity in the trap. In a feedback trap, a similar control is achieved by changing the feedback gain β . For larger values of β , the particle starts to oscillate because of overcorrection of the perturbations, as indicated by the emergence of the peak in the power spectrum [231]. The motion is undesirable both for the longer relaxation time created by the oscillations and for the greater variance in the particle position. The frequency at which the resonance appears depends on the time delay (t_d) of the feedback loop. In Fig. 3.14, we exclude the resonant $\beta = 0.3$ curve from our estimate of bandwidth increase.

3.7 Isotropic traps

As shown in Fig. 3.14, the feedback trap can *reduce* trap strength. In the usual version of an optical trap, the axial stiffness is typically 3–4 times smaller than the transverse stiffness because of radiation pressure and the weaker gradient of intensity along the axis of the focused laser beam [188]. Anisotropic traps used as force sensors have the disadvantage that the measurement bandwidth differs according to the direction of the force that is applied.

An isotropic trap would allow unbiased measurement of dynamics in a three-dimensional environment.

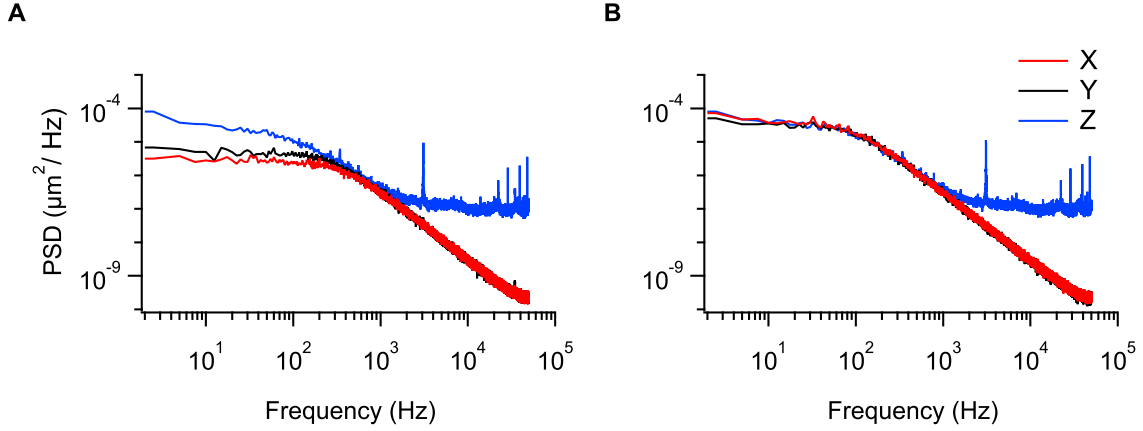


Figure 3.15: Power spectrum density of the isotropic trap. **A.** Power spectrum density of the x , y and z signals before the feedback ($k_t^x = 27.35 \pm 0.20$, $k_t^y = 20.72 \pm 0.17$, and $k_t^z = 7.48 \pm 0.13$ pN/ μm). **B.** Power spectrum density of the x , y , and z signals after the feedback ($k_v^x = 7.34 \pm 0.10$, $k_v^y = 7.42 \pm 0.12$, and $k_v^z = 7.48 \pm 0.13$ pN/ μm).

Here, we show that we can use feedback to reduce the lateral stiffness of the trap to make the trap isotropic, with equal stiffness in the lateral and axial directions (Fig. 3.15). The axial position of the trapped particle is estimated from the total intensity of the scattered light on the detector. Currently, the higher noise level of axial measurements limits the bandwidth that can be achieved through feedback to ≈ 2 kHz, as compared to transverse sensitivity (≈ 50 kHz). With improved axial sensitivity, it should be possible to create an isotropic trap by *increasing* the axial stiffness to match the lateral stiffness.

3.8 Virtual double-well potential

We create a static virtual double well with our feedback trap. Such potentials have previously been created with rapidly scanning single-beam optical tweezers between two positions [171]. However, multiplexed optical tweezers can impose only a limited range of potentials. Here, we define a double-well potential from three parabolic pieces that are joined together in a way that makes the function and its first derivative continuous but has two jump discontinuities in the second derivative. The parametric form allows independent control of well separation and barrier height. To simplify the equations, we scale energy by $k_B T$ and lengths by $\sqrt{D\Delta t}$, where D is the diffusion constant of the particle, and Δt is the sampling

time. Specifically, we define

$$U(x') \equiv \begin{cases} \frac{1}{2}\beta(x' + x'_m)^2 & x' \leq -x'_p \\ -\frac{1}{2} \left[\frac{2E_b}{(x'_m)^2 - \frac{2E_b}{\beta}} \right] x'^2 + E_b & -x'_p < x' < x'_p \\ \frac{1}{2}\beta(x' - x'_m)^2 & x' \geq x'_p, \end{cases} \quad (3.17)$$

where x'_m is the well position, $\beta = 0.03$ the proportional feedback constant near the minimum of the potential well, and E_b the potential barrier. The matching point is defined by enforcing continuity of U and $\partial_{x'}U$ and given as

$$x'_p = \left(\frac{k_1}{k_1 + k_2} \right) x'_m. \quad (3.18)$$

The force constants of the stabilizing potential k_1 and the destabilizing potential k_2 can be calculated from the values of β and E_b as

$$k_1 = \beta \frac{\gamma}{\Delta t} \quad \text{and} \quad k_2 = \left(\frac{2E_b}{x'^2_m - \frac{2E_b}{\beta}} \right) \frac{\gamma}{\Delta t}. \quad (3.19)$$

This parametrization of a double-well potential is more flexible than the one used in Ref. [202], as we can independently control the well separation and barrier height, keeping the curvature at the bottom of the wells fixed.

Figure 3.16 shows a family of double-well potential curves reconstructed from their respective time series using the Boltzmann distribution, $\pi(x') \sim \exp[-U(x')/k_B T]$, where the well separation is 60 nm. The black curves in Fig. 3.16 are calculated from Eq. 3.17 with imposed parameters that are not fit to the data (gray markers). We have confirmed that best-fit values for parameters such as E_b and x'_m are within 5% of the values imposed by the control program. The errors in these parameters can be the cumulative effect of systematic errors in our calibration procedure. Although these errors are small for our purpose, a more careful calibration can be done to create virtual potentials by including systematic error in the feedback algorithm.

Another important feature of a feedback trap is that the scale of potentials is not limited by the optical resolution of the microscope. The ability to create double-well potentials with low energy barrier but high well curvature is important, as it traps the particle in a well-defined volume of space while still allowing for fast transitions between macrostates. In Figure 3.16, the well separation was 60 nm. To test the smallest scale we could create, we increased the feedback gain [231] to $\alpha \approx 0.14$, which roughly corresponds to critical

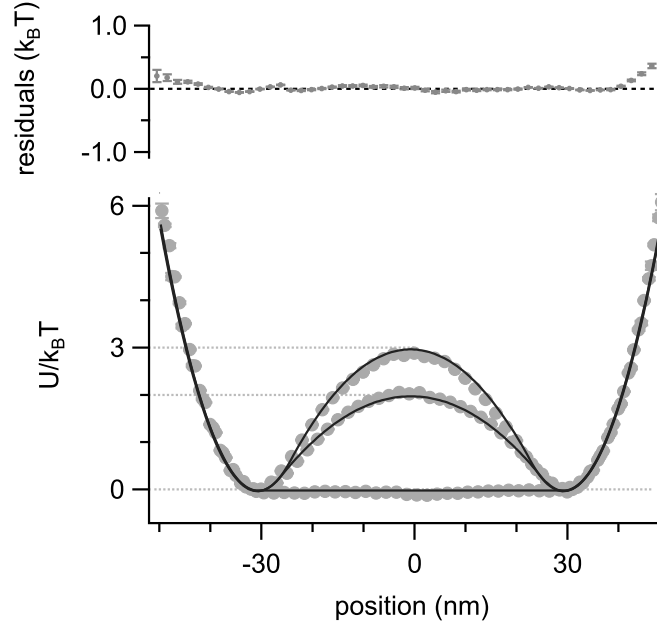


Figure 3.16: Virtual double-well potentials with different barrier heights ($E_b/k_B T = 0, 2$, and 3) and fixed well separation. Gray markers denote potentials reconstructed from the Boltzmann distribution of the position measurements; the superimposed solid black lines show the imposed potentials. The residuals are calculated for $E_b/k_B T = 3$, which has the maximum root-mean-square error of $\approx 0.12 k_B T$. Time series duration is 50 s for all three cases.

damping. At such large values of feedback gain, the effective damping of the trap dynamics is reduced.

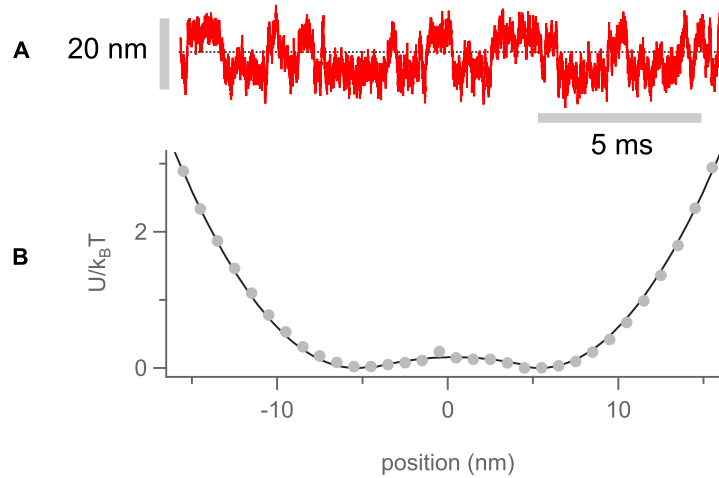


Figure 3.17: **A.** Time series showing spontaneous hops between two states. **B.** The reconstructed potential (gray markers) shows wells 10.6 nm apart and a barrier height $0.16 k_B T$. Black solid line is a fit using Eq. 3.17.

Figure 3.17A shows the time series for the smallest well separation that we could achieve with feedback under these conditions. At 10.6 nm, the well separation is far below the diffraction limit ≈ 220 nm (Fig. 3.17B). Time-shared traps cannot create potentials with independently tunable barrier height, well separation, and well curvature. Spatial light modulators cannot create these shapes at sub-diffractive-limit length scales [171]. Although the energy barrier is quite low ($0.16 k_B T$), the small curvature of the barrier and sufficiently large separation of wells still lead to two-state behavior in the time series, where the dwell time in a well is $\approx 10\times$ the transition time between wells with the transition rate r_k given by Kramer’s formula $r_k = 1/(2\pi\gamma)\sqrt{k_1 k_2} \exp[-E_b/(k_B T)]$ [232]. A full analysis would need to account for the effects of measurement errors, which smooth the histogram and thus the potential.

3.9 Discussion

In this chapter, we have demonstrated a feedback trap system based on optical tweezers. Using this feedback technique, we have created virtual harmonic potentials with different stiffness constants, static double wells with independently tunable parameters, and isotropic traps. These applications of optical tweezers have not been shown before using techniques such as time-shared traps. Although our work is for two-dimensional traps, it can be readily extended to feedback in three dimensions, using the intensity to measure the axial position (as done here) or using a variety of more sophisticated techniques [233–235] and a method to move the trap position axially.

The ability to create and control energy landscapes at scales comparable to the size of proteins offers intriguing possibilities for biophysical applications. For example, recent experiments suggest that protein folding can be well described by diffusive dynamics on an effectively one-dimensional energy surface [236]. Using the techniques developed here, one could create model systems with similar dynamics. Also, one could place a colloidal particle in a potential whose dynamics could imitate, in a controllable way, the dynamics of a ligand. Even more intriguingly, those dynamics could be adaptive, allowing exploration of phenomena such as catch bonds, whose dissociation lifetime increases sharply when pulled [237]. Such studies would likely be facilitated by using smaller particles. Techniques such as interferometric scattering microscopy (iSCAT) have shown that by interfering a reference beam with scattered light, it is possible to detect colloidal particles and even proteins on a 10-nm scale [238, 239]. Reducing the delays and feedback latency will allow a further reduction in the scale of potentials.

Finally, time-dependent potentials can be used to carry out interesting stochastic thermodynamic experiments. With feedback bandwidths $1000\times$ faster than the Bechhoefer lab’s previous work on slow stochastic processes [119, 196, 197], we can address problems with faster dynamics such as finite-time transformations in non-equilibrium thermodynamics

[240, 241]. Such experiments could also take advantage of another feature of feedback traps based on optical tweezers: because the applied forces are localized (in contrast to traps based on electrokinetic forces), they allow custom energy landscapes containing multiple particles.

Chapter 4

Mpemba effect

That an initially hot object might cool more quickly than an initially warm object seems impossible, because our intuitions tend to be shaped by systems that remain at or near thermal equilibrium. If an object is cooled *slowly*, its time-dependent state is well characterized by a temperature, and a hot object cannot cool without passing through all intermediate temperatures. Nonetheless, when rapidly quenched by placing a system in contact with a cold bath, the Mpemba effect is often observed in settings where a phase transition occurs [242, 243]. In this chapter, we provide clear experimental evidence for the Mpemba effect in a colloidal system that lacks a phase transition. Our results agree quantitatively with theoretical predictions giving a *general* explanation for the Mpemba effect [186], and we take advantage of our understanding of the underlying physics to achieve cooling times that are exponentially faster than the time to cool under typical initial conditions.

The bulk of this chapter was published in *Nature* [244]. The theory, developed with Raphaël Chétrite, for the geometric interpretation of the Mpemba effect was published in *Frontiers in Physics* [245].

4.1 Definition of the Mpemba effect

Past investigations of the Mpemba effect have suffered from vague, mutually inconsistent definitions. We thus begin by defining the Mpemba effect in terms of three temperatures $T_h > T_w > T_c$, for which the time t_h to cool a system from a hot to a cold state is shorter than the time t_w to cool it from an intermediate warm state to the same cold state. In the above definition, “hot” describes an initial state that is at thermal equilibrium at temperature T_h , while “warm” describes an initial state at thermal equilibrium at temperature T_w . The cold temperature $T_c = T_b$ is that of the thermal bath of water and is the identical final state for all initial conditions studied. All terms in our definition are unambiguous: the only ingredients are the equilibrium start and end states, characterized by the usual notion of temperature, and the time it takes to go from one state to another. By contrast, previous definitions of the Mpemba effect have been based on criteria such as the “time to start

freezing” [12, 243], which is hard to reproduce because of sensitivity to details of sample preparation [14], including impurities in the water, cleanliness of the sample container, and number of times heated.

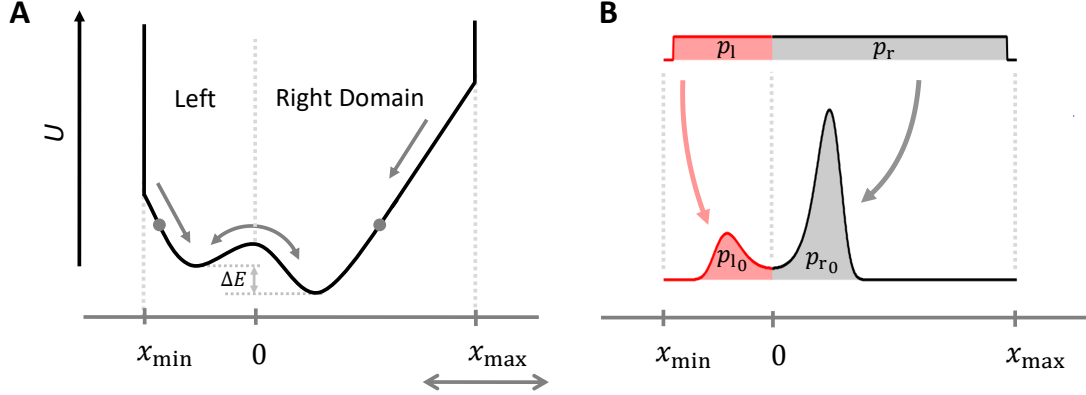


Figure 4.1: Schematic diagram of the energy landscape and Boltzmann distribution for the Mpemba effect. **A.** The solid black line represents the energy landscape $U(x)$, set asymmetrically within the box $[x_{\min}, x_{\max}]$ with infinite potential walls at the domain boundaries. The asymmetry coefficient $\alpha \equiv |x_{\max}/x_{\min}|$, where x_{\max} is changed to vary α . The outer slopes of the potential (indicated by solid gray markers) correspond to the maximum force that can be exerted by the optical tweezers. The difference in energy between metastable and stable states is ΔE . **B.** The Boltzmann distribution $\pi(x; T_b)$ at the bath temperature. The interval p_r is the probability for a particle to initially be in the right domain for $T_h \rightarrow \infty$. At the bath temperature, the probability to be in the ground state (right well) is p_{r0} . We find that the Mpemba effect is strongest for $p_r \approx p_{r0}$, a condition that allows the probability contained in the initial “basin of attraction” to drain directly to the ground state. Similarly, for the left well, $p_l \approx p_{l0}$, with $p_l = 1 - p_r$ and $p_{l0} = 1 - p_{r0}$.

4.2 Energy landscape for the Mpemba effect

In our experiment, a single Brownian particle diffuses in water, subject to forces from a carefully shaped potential (Fig. 4.1A). We construct a one-dimensional virtual tilted double-well potential using a feedback-optical tweezer (Fig. 3.1). It is a continuous piecewise potential with a double well joined by linear potentials at the extremes (Eq. 4.2). The overall potential is set in an asymmetric domain. The tilted double-well potential is parametrized as

$$U_0(x) = E_b \left[1 - 2 \left(\frac{x}{x_m} \right)^2 + \left(\frac{x}{x_m} \right)^4 \right] - \frac{1}{2} \Delta E \left(\frac{x}{x_m} \right), \quad (4.1)$$

where $E_b = 2$ is the barrier height, $\Delta E = 1.3$ the tilt in the potential, and $x_m = 40$ nm the well position. In Eq. 4.1, energies are scaled by $k_B T_b$ and lengths by $\sqrt{D \Delta t} \approx 1.8$ nm, where k_B is the Boltzmann constant, T_b the bath temperature (set by the room temperature),

$D = 0.32 \text{ } \mu\text{m}^2/\text{s}$ the diffusion coefficient of the particle, and $\Delta t = 10 \text{ } \mu\text{s}$ the sampling time. The bath temperature is typically $\approx 23 \text{ }^\circ\text{C}$. Its precise value for different runs is unimportant since the potential and all related energies are scaled by $k_B T_b$ and thus are independent of the bath temperature value. In our experiment, the temperature quenches are large, never less than a factor of two in absolute temperature. Minor changes in the trap position due to temperature drifts during runs ($\approx 0.1 \text{ nm/run}$) then do not directly have a significant effect on the dynamics of $p(x, t)$.

The overall potential energy landscape $U(x)$ of the system is given as

$$U(x) \equiv \begin{cases} U_0(x_1) + F_{\max}x & x \leq x_1 \\ U_0(x) & x_1 \leq x \leq x_r \\ U_0(x_r) - F_{\max}x & x \geq x_r, \end{cases} \quad (4.2)$$

where $x_1 \approx -66 \text{ nm}$ and $x_r \approx 68 \text{ nm}$ are positions defined so that $|U'_0(x_1)| = |U'_0(x_r)| = F_{\max}$ ($\approx 20 \text{ pN}$). The potential $U(x)$ and its first derivatives (forces) are continuous everywhere, but the second derivative has jump discontinuities at x_1 and x_r . To implement the double-well potential in Eq. 4.1 requires a force whose magnitude increases indefinitely at large distances from the well minima. However, optical tweezers are limited to a maximum force F_{\max} , given a fixed beam power. To accommodate this physical constraint, we match the double-well potential of Eq. 4.1 beyond x_1 and x_r to a linear potential whose slope corresponds to the maximum force an optical tweezer can exert.

The tilted double well creates a bistable potential with two macrostates: the shallow left well corresponds to a metastable macrostate, and the deep right well to a stable macrostate. The linear parts of the potential provide direct kinetic paths towards the minima, and the barrier allows spontaneous hopping between the wells. Because spatial dimensions are small and the energy barrier low, the bead can rapidly equilibrate with the bath ($\lesssim 0.1 \text{ s}$). We can then easily carry out several thousand trials, forming a statistical ensemble from which accurate measurements of both equilibrium and nonequilibrium states are possible. As we will see below, to observe the Mpemba effect, we should place the potential asymmetrically between the potential boundaries, x_{\min} and x_{\max} , which determine the region in space explored by the particle at high temperatures. The parameter $\alpha \equiv |x_{\max}/x_{\min}|$ defines the degree of asymmetry within the domain “box.” In our experiments, we change α by varying x_{\max} while fixing x_{\min} .

4.2.1 Choice of potential energy landscape

We have engineered our potential in such a way that the equilibration times for both hot and warm systems are $\lesssim 0.1 \text{ s}$. Such short times allow us to reach the equilibrium state with the bath, to connect directly to our definition of the Mpemba effect. They also allow for

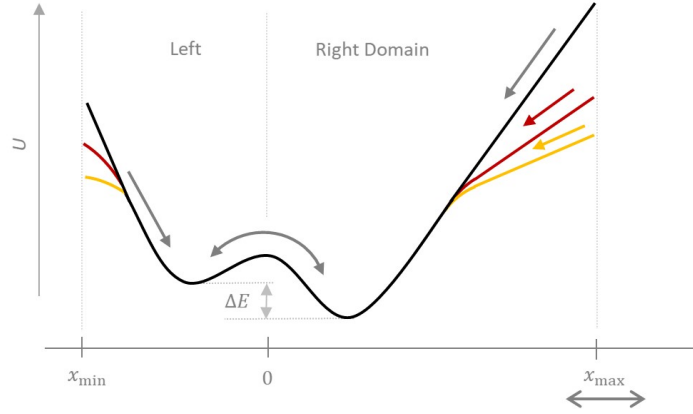


Figure 4.2: Schematic of potential energy landscape. The bath potential energy is shown with different slopes. A steep slope represents high velocities with which the particles are quenched towards the minima. The steepness of the linear potential determines both the time and temperature scales.

easy acquisition of several thousand runs. From such an ensemble, we can accurately reconstruct the time-dependent nonequilibrium state $p(x, t)$ of the system as it cools. Moreover, because we recalibrate after each quench, we avoid the effects of drifts. In particular, even after allowing all transient effects due to the preparation of an experiment to die away, we consistently observe drifts in position measurements on the order of 1 nm s^{-1} . Given length scales of $\approx 100 \text{ nm}$, these can become significant after several seconds. By limiting runs to 0.1 s , we ensure that effects due to drifts are negligible.

Having chosen the overall scale of the potential, we needed to define its actual shape. The barrier height and tilt are adjusted in such a way that the system, when trapped in the metastable state, takes longer to reach the equilibrium than the system that finds a direct path towards the equilibrium.

As Eq. 4.2 implies, we also impose a linear potential for $x < x_l$ and $x > x_r$ (gray markers, Fig. 4.1A). The principal motivation, in our case, is that the tweezers can impose a maximum force F_{max} , and we simply allow the imposed force field to saturate when that limit is reached. Because the maximum forces are large, we can reach large energies; the potential can easily range up to $\approx 100 k_B T_b$. Such energy ranges are much larger than ordinary materials. However, we use such large energy scales solely as a means to create short time scales.

If time scales were allowed to be longer, then we could create similar dynamics with much reduced energy scales. The velocity at which the particle is pulled towards a minimum is determined by the force as $v_{\text{max}} = F_{\text{max}}/\gamma \approx E_{\text{tot}}/\gamma \ell \approx 60 \text{ } \mu\text{m/s}$, where $F_{\text{max}} \approx 20 \text{ pN}$ ($0.2 k_B T_b/\text{nm}$) is the maximum force exerted by the optical tweezer, $E_{\text{tot}} \approx 100$ the energy (scaled by $k_B T_b$) at the domain boundaries, γ the viscous drag coefficient, and ℓ the distance

between the basins of attraction and the respective domain boundaries. Thus, the kinetic timescale is approximated as $\tau \approx \ell^2/DE_{\text{tot}} \approx 0.3$ ms, where $D = k_{\text{B}}T_{\text{b}}/\gamma \approx 0.32$ $\mu\text{m}^2/\text{s}$ is the diffusion constant of the particle at the bath temperature T_{b} . Thus, we choose a large energy scale to have a fast relaxation towards the two macrostates. If we were to use a lower maximum slope of potential, we would have the same overall structure and range of Mpemba effects, but their time scale would be correspondingly longer. Figure 4.2 illustrates qualitatively how similar effects can be seen in potentials where there is a reduced maximum slope. Previous work [246] carried out in a potential similar to the yellow case indeed shows the Mpemba effect, but with a longer equilibration time (≈ 100 s) and smaller temperature range.

4.3 Imposing an instantaneous quench via initial conditions

In our experiment, the particle is always in contact with water at temperature T_{b} ; however, the initial state of the system is drawn from a Boltzmann distribution at a *higher* initial temperature. All temperatures are measured relative to the bath temperature T_{b} , and all energies are scaled by $k_{\text{B}}T_{\text{b}}$. However, physically preparing systems that are in thermal equilibrium at high temperatures such as $T_0 = 1000$ is not possible in our setup. Nor is it possible to create an instantaneous quench by changing the temperature of the bath. Instead, we sample initial positions from an equilibrium distribution and place the particle at those positions in the beginning of each run by applying a stronger force via the optical trap. To implement this, we calculate the cumulative distribution function (CDF) from the equilibrium probability density function (PDF) [246, 247]. The CDF for a random variable X is given as

$$F_X(x) = \int_{x_{\min}}^x dx p(x), \quad (4.3)$$

where the PDF $p(x)$ is integrated over the range $[x_{\min}, x]$ to calculate the CDF, $F_X(x)$. Since the CDF is in the range $[0, 1]$, we use a uniform random number generator to generate numbers between 0 and 1. A combination of binary-search algorithm and linear interpolation based on the neighboring values is used to get the accurate position (Fig. 4.3). We create lookup tables (LUTs) of the CDF functions at different temperatures and sample the initial position in a similar way for each run. Because the initial potential includes hard walls, the probability to draw an initial condition with $x < x_{\min}$ or $x > x_{\max}$ is zero. We thus normalize the PDF and CDF on the range $[x_{\min}, x_{\max}]$.

After an effectively instantaneous quench at $t = 0$, the particle position evolves according to the imposed virtual potential $U(x)$ under thermal environment fluctuations for 60 ms. This protocol is repeated $N = 1000$ times, with the resulting data used to create a statistical ensemble from which we estimate the state of the system every 10 μs . Although

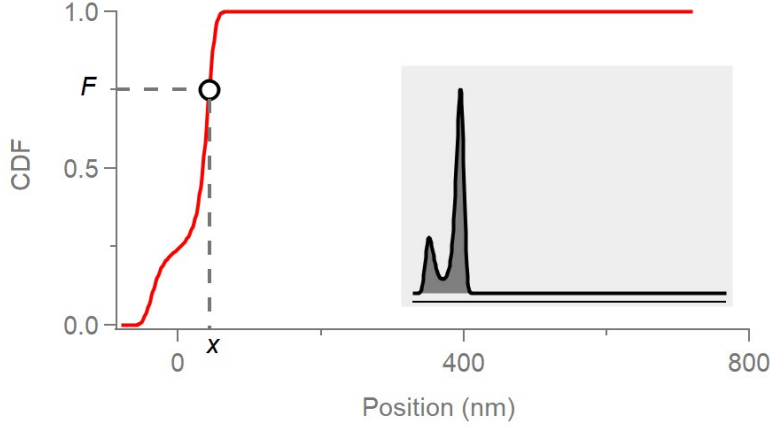


Figure 4.3: Cumulative probability distribution at the bath temperature. An algorithm based on binary search and linear interpolation is used to map the CDF (F) to position x (dashed lines). Asymmetry coefficient $\alpha = 9$.

the initial conditions are calculated assuming infinite walls at the domain boundaries, we cannot physically impose an infinite potential wall in the experiment. There is a maximum possible force applied by an optical trap. Thus, the dynamics of a particle may violate the motion and can briefly explore the regions outside the domain defined by the infinite walls. By simulating the particle dynamics using the Langevin equation, we found that these violations occur only 0.003% of the total time of the experiment (see section 4.10.1).

Figure 4.4A–C shows example time traces of evolution in the potential $U(x)$. From the time traces, we form frequency estimates of the probability density function $p(x, t)$ that records the system state as it evolves between the initial state $p(x, 0) = \pi(x; T_0) \propto \exp[-U(x)/k_B T_0]$ and the final state at equilibrium with the bath, characterized by $\pi(x; T_b)$, where T_0 is the initial temperature of the system.

At intermediate times while the system is relaxing, the dynamical state $p(x, t)$ does not, in general, have the form of a Boltzmann distribution for the potential $U(x)$ at any temperature; nevertheless, we can define a scalar quantity [183, 248] that measures the “distance” \mathcal{D} between $p(x, t)$ and the Boltzmann distribution in equilibrium with the bath, $\pi(x; T_b)$. For simplicity, we choose an L_1 measure of distance, but any measure that is monotonic with T_0 will also work.

4.4 Measuring the distance to equilibrium

Consider a colloidal particle immersed in a fluid bath of temperature T_b and subject to a one-dimensional potential $U(x)$. For systems in thermal equilibrium, the position x of the particle, when sampled from an ensemble of identically prepared systems, will obey the Boltzmann distribution (Eq. 3.13),

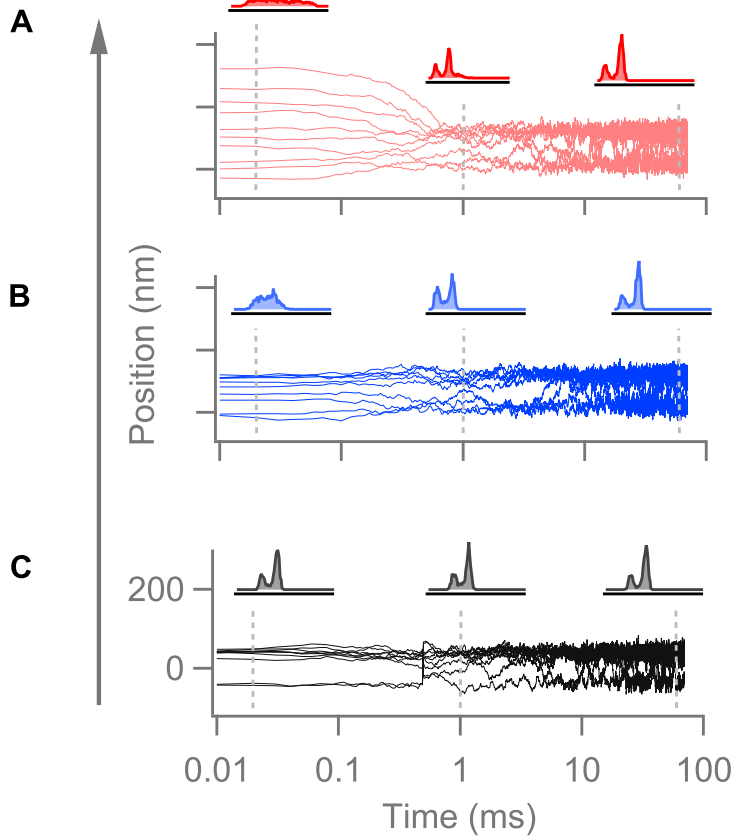


Figure 4.4: Dynamics of system relaxation to equilibrium. **A–C.** Ten trajectories of a particle released from the equilibrium distributions at hot (red), warm (blue), and cold (black) temperatures into the cold bath, with the evolving probability density $p(x, t)$ shown for three times.

$$\pi(x; T_b) = \frac{1}{Z} e^{-U(x)/k_B T_b} . \quad (4.4)$$

For a nonequilibrium system, it is not possible, in general, to define an equivalent notion of temperature. In a macroscopic system such as the ones used for previous experiments on the Mpemba effect, the system is typically in local equilibrium and may be described by a temperature field, $T(\mathbf{x}, t)$. When subject to the temperature quench specified by the protocol used in the Mpemba effect, temperature gradients are large, and it is impossible to characterize the system accurately by a single time-dependent temperature, such as the spatial average of $T(\mathbf{x}, t)$. In addition, a fluid object can have internal fluid motions that arise because of the quench (such as convection currents created when the top cools off more quickly than the bottom), meaning that other fields may be relevant, too.

In the mesoscopic single-colloidal-particle system studied here, we can measure the one-dimensional instantaneous probability distribution $p(x, t)$, the probability density for the measured position to lie between x and $x + dx$, by conducting a series of experiments on identically prepared trials. The set of trials forms an ensemble. In general, $p(x, t)$ does not correspond to a Boltzmann distribution of the form of Eq. 4.4, for any choice of “effective” temperature. As a result, we cannot assign an intermediate temperature to the system as it relaxes to equilibrium. Instead, we follow Lu and Raz [186], who argue that even though it is in general impossible to define an intermediate temperature, one can nonetheless define a “distance measure” between probability distributions. They further argue that the observation of the Mpemba effect is independent of the choice of the functional that measures the distance from thermal equilibrium, if the measure satisfies three properties:

1. $\mathcal{D}[p(x, t), \pi(x, T_b)]$ should be a monotonically non-increasing function of time during relaxation towards equilibrium;
2. $\mathcal{D}[\pi(x, T_0), \pi(x, T_b)]$ should be a monotonically increasing function of T_0 for all $T_0 > T_b$, so that initially hotter states are farther from the bath distribution;
3. $\mathcal{D}[p(x, t), \pi(x, T_b)]$ should be a continuous and convex function of probability p when evaluated at any particular value of x and t .

Although we often write \mathcal{D} using a simplified notation that omits terms from its arguments, it is important to remember that it is a functional that depends on both a dynamic probability distribution $p(x, t)$ and a reference equilibrium distribution $\pi(x, T_b)$. Note that the measure is not required to be a proper distance, allowing for the asymmetric Kullback-Leibler (KL) divergence as one possibility.

Although our results are based on L_1 distance measures, we will check that similar results are found using the KL divergence. We begin by defining and discussing the L_1 distance and KL divergence here.

4.4.1 L_1 distance

To evaluate this distance from trajectory data, we partition the position measurements into N_b bins:

$$\mathcal{D}_{L_1}[p(x, t); \pi(x; T_b)] = \sum_{i=1}^{N_b} |p_i - \pi_i|, \quad (4.5)$$

where $p_i \equiv P(x_i, t)$ is the frequency estimate of the probability for a measured position x at a time t after the quench to fall within the interval $[x_i, x_{i+1})$, where $x_i \equiv i \Delta x$, with $\Delta x = (|x_{\max}| + |x_{\min}|)/N_b$. Similarly, $\pi_i \equiv \pi(x_i; T_b)$ is the histogram estimate of the Boltzmann distribution at temperature T_b . The smallest L_1 distance measured between the two distributions is limited by the statistical noise due to the finite sample size. To make

a naive calculation for two uniform distributions (not necessarily in equilibrium), we can write

$$p_i = \frac{N_c}{N}, \quad (4.6)$$

where $N_c = N/N_b$ is the average number of counts in each bin and N the number of counts across all bins. The variance σ^2 of p_i for a typical bin is approximately

$$\sigma_{p_i}^2 = \frac{N_c}{N^2} = \frac{1}{N_b N}. \quad (4.7)$$

The variance of $|p_i - \pi_i|$ is expected to be comparable to the variance of $(p_i - \pi_i)$, which is $\sigma_{p_i}^2 + \sigma_{\pi_i}^2 = 2N_c/N^2$. Then, summing over N_b bins (neglecting correlations) and taking a square root to estimate the standard deviation leads us to expect fluctuations of

$$\sigma_{\mathcal{D}_{L_1}} = \mathcal{O} \left(\sqrt{\frac{N_b}{N}} \right). \quad (4.8)$$

Numerically, we confirm this scaling of fluctuations. Note that even though we impose a particular potential and therefore have an expected Boltzmann distribution, we use the empirical estimate for π_i . A more sophisticated approach—not needed here—would be to calculate the mean absolute difference of two Poisson variables, which can be expressed in terms of a Skellam distribution [249]. The main point is that the noise level scales with the number of trials N that constitute the ensemble as $N^{-1/2}$.

As shown in Fig. 4.5, we use the L_1 distance curve to determine the time at which the system reaches equilibrium ($\mathcal{D} \approx 0$, within noise levels—black curve). The crossing between the distance curves of the hot and warm system indicates that the Mpemba effect exists. Note that the effect is independent of the noise level of the control experiment because once the hot distance curve crosses the warm distance curve, the former stays below the latter until they both reach equilibrium.

4.4.2 Kullback-Leibler (KL) divergence.

Another possible measure of distance is the KL divergence [250]. Using similar definitions of the distributions, we write

$$\mathcal{D}_{\text{KL}} [p(x, t); \pi(x; T_b)] \equiv \sum_{i=1}^{N_b} p_i \ln \left(\frac{p_i}{\pi_i} \right) = \sum_{i=1}^{N_b} [p_i \ln p_i - p_i \ln \pi_i]. \quad (4.9)$$

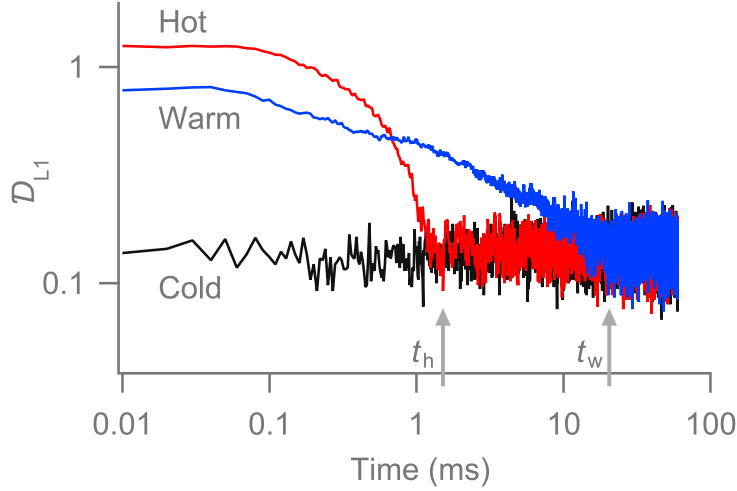


Figure 4.5: L_1 distance shows the Mpemba effect. The L_1 distances calculated for systems at three different temperatures ($T_h = 1000$, $T_w = 12$, and $T_c = 1$) from their respective time traces. The initially hot system starts a greater distance from equilibrium than the initially warm system but equilibrates first ($t_h < t_w$), illustrating the Mpemba effect. The cold distance plot is a control experiment where the particle is released from the equilibrium distribution at the bath's temperature. At each time, the distribution fluctuates from the average by an always-positive distance. There are $N = 1000$ runs per initial temperature; asymmetry coefficient $\alpha = 3$.

The KL divergence measures the relative entropy between two probability distributions. It has a physical motivation in that it can be related to the nonequilibrium free energy of a system as $F_{\text{noneq}} = F_{\text{eq}} + \mathcal{D}_{\text{KL}}[p(x, t); \pi(x; T_b)]$ and can thereby be connected to the entropy produced during the relaxation process [186, 251]. Both equilibrium and nonequilibrium free energies here are scaled by $k_B T_b$.

Figure 4.6 shows the KL divergence curves based on the data presented in Fig. 4.5. The figure illustrates that the observation of the Mpemba effect does not depend on the choice of distance function, provided the choices satisfy the temperature-like properties mentioned in Sec. 4.4. The numerical details and shape of the individual curves may change, but the crossing of curves is a robust observation, as proved earlier by Lu and Raz [186].

Although the KL divergence can measure the distance from thermal equilibrium, it has two inconvenient features that led us to prefer the L_1 distance. The first is that some bins will have zero counts. If these zero-value bins were counted in Eq. (4.9), the measured KL divergence would be infinite. To avoid such issues, we regularize the equilibrium distribution by adding a single pseudocount to each bin [252]. We then normalize the histogram to estimate the probability density. Although the use of pseudocounts biases the distance estimation slightly, there is no effect on the presence or absence of distance-curve crossing (Fig. 4.6), as demonstrated by the fact that the results with the KL divergence agree

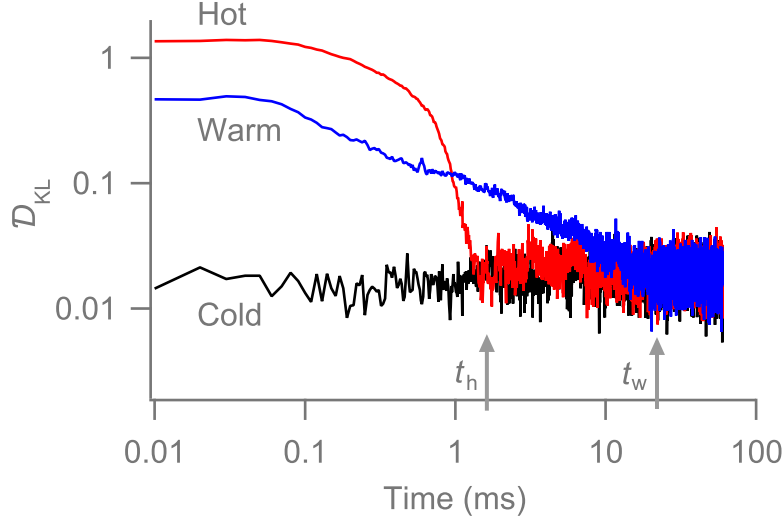


Figure 4.6: The KL divergence calculated based on the data used to calculate \mathcal{D}_{L_1} in Fig. 4.5.

qualitatively with those using the other distance measure. The second inconvenience of the KL divergence is that to extract the a_2 coefficient (see Sec. 4.6) requires a Taylor expansion, which is not needed when using the L_1 norm.

Thus, we choose L_1 distance for our analysis. From now onward, we will use the notation \mathcal{D} (with no subscript) to represent the L_1 distance. Figure 4.5 shows a qualitative representation of the Mpemba effect based on the crossing of the distance curves. However, the equilibration times of systems starting at different initial temperatures is a direct measure of the cooling time. We found that the relaxation dynamics of the cooling system are dependent on both the initial temperature and the asymmetry in the domain of the bath potential. In the next section, we will do a systematic study of the effect of the domain sizes on the Mpemba effect.

4.5 Observation of the Mpemba effect in asymmetric domains

To determine how the Mpemba effect depends on the shape of the potential, we first place the double-well potential in a symmetric box ($\alpha = 1$). Figure 4.7A shows the measured times to reach equilibrium for systems that start at different initial temperatures. The equilibration time increases sharply and saturates at high temperatures, where the initial probability distribution is nearly uniform. Since the equilibration time monotonically increases with initial temperature, there is no Mpemba effect.

The situation changes qualitatively when x_{\max} is increased and the box becomes asymmetric. For $\alpha = 3$ (Fig. 4.7B), the equilibration time increases initially but then decreases rapidly for higher initial temperatures ($T_0 > 10$), indicating the Mpemba effect. For

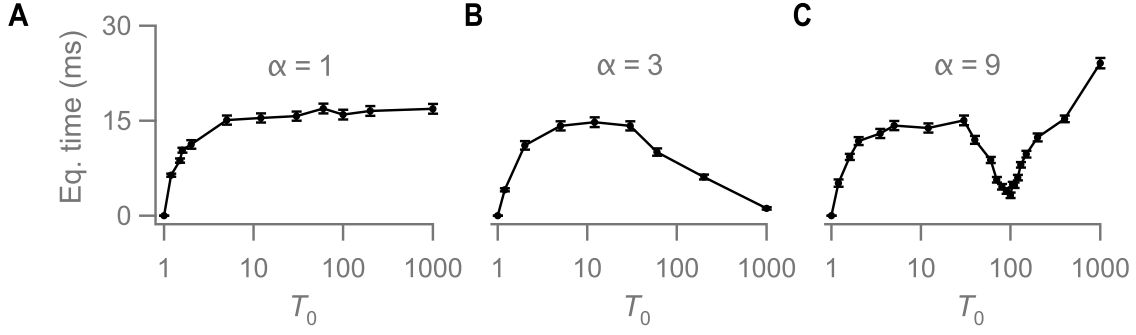


Figure 4.7: Equilibration time as a function of initial system temperature. **A–C.** Solid markers are the equilibration times for asymmetry coefficients $\alpha = 1, 3, 9$. Regions of each plot with a negative slope indicate the Mpemba effect. The error bars represent standard deviations calculated using Eq. 4.40 in section 4.10.2.

$\alpha = 9$ (Fig. 4.7C), the equilibration time decreases at intermediate temperatures, where the Mpemba effect is observed, but increases again at very high temperatures.

To understand the different equilibration-time curves in Fig. 4.7, we should examine more closely the distance curves $\mathcal{D}(t)$, which summarize the relaxation of the system to thermal equilibrium. Figure 4.8A shows data for $\alpha = 9$, corresponding to the curve in Fig. 4.7C. On the semilog plots, straight lines represent exponential decay. For $T_0 = 100$, the Mpemba effect is particularly clear, and the system appears to relax to equilibrium as a single exponential. For other initial temperatures, the relaxation seems to involve multiple exponential relaxation processes.

4.6 Analysis based on eigenfunction expansion

To interpret the dynamical behavior of $\mathcal{D}(t)$, we apply a recent approach that connects the Mpemba effect to an eigenvalue expansion [186]. In our experiment, the particle is continuously under the influence of drag forces and random forces. The time evolution of the particle is generally described by the Langevin equation (Eq. 3.9). Equivalently, these dynamics can also be described in terms of the time evolution of the probability density $p(x, t)$ of particle positions by the Fokker-Planck (FP) equation as (Eq. 2.25)

$$\frac{\partial p(x, t)}{\partial t} = \left[-\frac{1}{\gamma} \frac{\partial}{\partial x} F(x) + \frac{k_B T_b}{\gamma} \frac{\partial^2}{\partial x^2} \right] p(x, t) \equiv \mathcal{L}_{\text{FP}} p(x, t). \quad (4.10)$$

The underlying probability density $p(x, t)$ can be expressed as an infinite sum of eigenfunctions of the Fokker-Planck equation (FPE) as

$$p(x, t) = \pi(x; T_b) + \sum_{k=2}^{\infty} a_k(\alpha, T_0) e^{-\lambda_k t} v_k(x; \alpha, T_b), \quad (4.11)$$

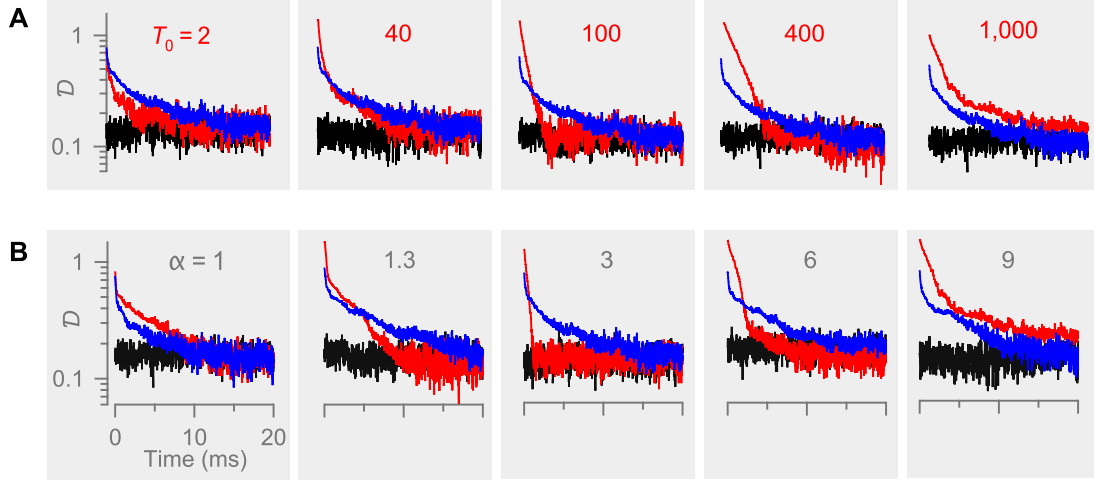


Figure 4.8: Controlling relaxation times. **A.** L_1 distance for systems with initial temperatures $T_b = 1$ (black), $T_w = 12$ (blue), and $T_0 = \{2, 40, 100, 400, 1000\}$ (red), with $\alpha = 9$. At low and high T_h , no Mpemba effect is observed. At intermediate T_h , the distance curves cross, indicating a more rapid cooling of the hot system. **B.** L_1 distance for domain asymmetries $\alpha = \{1, 1.3, 3, 6, 9\}$, for $T_b = 1$ (red), $T_w = 12$ (blue), and $T_h = 1000$ (red). The Mpemba effect is observed for intermediate asymmetry. The control experiment is repeated for each measurement.

where $\pi(x; T_b)$ is the equilibrium probability density function, achieved for $t \rightarrow \infty$. The k^{th} eigenfunction $v_k(x; \alpha, T_b)$ is a spatial function that depends on the form of the potential $U(x)$, including the asymmetry coefficient α , and the bath temperature T_b . The contribution of eigenfunction v_k decays exponentially, at a rate $\exp(-\lambda_k t)$, where the eigenvalues $\lambda_k \geq 0$ are ordered so that $0 = \lambda_1 < \lambda_2 < \dots$. Since $\lambda_2 < \lambda_3$, the higher-order terms are exponentially small; thus, the eigenvalue λ_2 corresponds to the slowest relaxation rate. Note that relaxation $\sim e^{-\lambda_3 t}$ is exponentially faster than relaxation $\sim e^{-\lambda_2 t}$, so that the condition $a_2 = 0$ corresponds to an exponential speed-up of relaxation rate. At long times, Eq. 4.11 implies that the density function is dominated by the first two terms of the infinite series:

$$p(x, t) \approx \pi(x; T_b) + a_2(\alpha, T_0) e^{-\lambda_2 t} v_2(x; \alpha, T_b), \quad (4.12)$$

where the coefficient $a_2(\alpha, T_0)$ is a real number that depends on the initial temperature and the potential energy.

4.6.1 Calculation of the a_2 coefficient

To calculate $a_2(\alpha, T_0)$, we evaluate the inner product between the left eigenfunction $u_2(x; \alpha, T_b)$ and the initial probability distribution $p(x, 0) = \pi(x; T_0)$. Then,

$$\langle u_2 | \pi(x; T_0) \rangle = \langle u_2 | \pi(x; T_b) \rangle + \sum_{k=2}^{\infty} a_k(\alpha, T_0) \langle u_2 | v_k \rangle, \quad (4.13)$$

where the inner product between two functions $f(x)$ and $g(x)$ in the interval $[x_{\min}, x_{\max}]$ is defined as $\langle f | g \rangle \equiv \int_{x_{\min}}^{x_{\max}} dx f(x)g(x)$. The left and right eigenfunctions are biorthogonal, $\langle u_2 | v_k \rangle = 0$ for $k \neq 2$ (Sec. 2.2.2). We can evaluate the scalar products in Eq. (4.13) to find $\langle u_2 | \pi(x; T_0) \rangle = a_2(\alpha, T_0) \langle u_2 | v_2 \rangle$, or

$$a_2(\alpha, T_0) = \frac{\langle u_2 | \pi(x; T_0) \rangle}{\langle u_2 | v_2 \rangle}, \quad (4.14)$$

where the normalization factor $\langle u_2 | v_2 \rangle = 0.55$, given our normalization convention, which is to take $\langle u_i | u_i \rangle = \langle v_i | v_i \rangle = 1$, for $i = 1, 2, \dots$. In Eq. (4.14), we recall that $u_2(x)$ and $v_2(x)$ depend on the *bath* temperature T_b and the asymmetry coefficient, α . Thus, a_2 captures the “overlap” between the initial system state and the second left eigenfunction.

We have shown that the FP operator is non-Hermitian, and thus the left and right eigenfunctions are different (Sec. 2.2.1). We numerically solve the FP equation for our system using standard *Mathematica* operations to find the eigenfunctions. Figure 4.9 shows the negative left and positive right eigenfunctions corresponding to the smallest non-zero eigenvalue of \mathcal{L}_{FP} . To clearly show both the eigenfunctions, we have plotted the *negative* left eigenfunction here. Note that the overall sign of the eigenfunctions is arbitrary. Once we fix the sign of one eigenfunction, the sign of the others follows accordingly.

Equation (4.12) has several consequences:

- The equilibration time of an initial state depends on its a_2 coefficient.
- The difference in equilibration times $t_w - t_h$ is independent of the noise level of $\mathcal{D}(t)$.
- The magnitude of the a_2 coefficient may be extracted from the time course of $\mathcal{D}(t)$.
- For $a_2 = 0$, the system reaches equilibrium at an exponentially faster rate than systems with non-zero values of a_2 (decay dominated by $\lambda_3 > \lambda_2$).
- The Mpemba effect correlates with the condition [186] that $|a_2(\alpha, T_h)| < |a_2(\alpha, T_w)|$.

The last point implies that the Mpemba effect occurs over a range of initial temperatures for which $|a_2(\alpha, T_0)|$ decreases as T_0 increases.

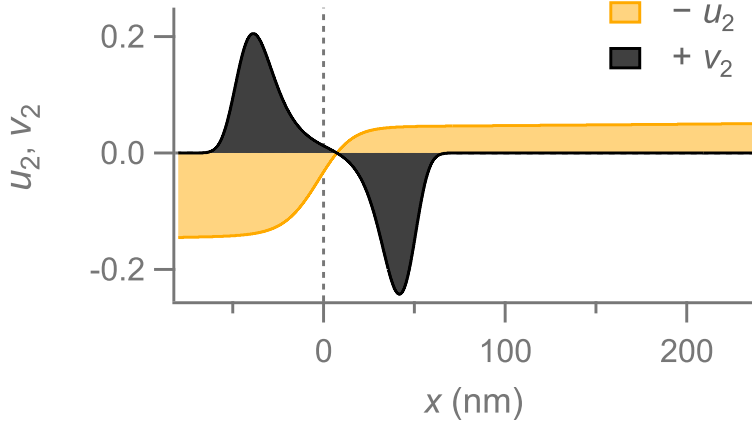


Figure 4.9: Eigenfunction for the FP operator for a double-well potential. $u_2(x)$ and $v_2(x)$ are the left and right eigenfunctions, respectively, and correspond to the smallest non-zero eigenvalue of the FP operator. The negative of the left eigenfunction is plotted to aid visualisation. The eigenfunctions are calculated for $\alpha = 3$.

4.6.2 Relationship between $\Delta\mathcal{D}$ and the a_2 coefficient

In the experiment, we do not measure the second left and right eigenfunctions directly but rather a quantity $\Delta\mathcal{D}$ proportional to $|a_2(\alpha, T_0)|$. To connect these quantities in the long-time limit, we rearrange Eq. 4.12 as $p(x, t) - \pi(x; T_b) \approx a_2(\alpha, T_0) e^{-\lambda_2 t} v_2(x)$ for $k = 2$ and take the absolute difference between the dynamic and reference probabilities. Note that, in the long-time limit, we have neglected the terms for $k > 2$, as they are exponentially smaller. However, in the experiment, we calculate the frequency estimate of the probability and thus summing over all the bins for the absolute difference between the two probabilities gives

$$\sum_{i=1}^{N_b} |p_i - \pi_i| = \sum_{i=1}^{N_b} |a_2(\alpha, T_0) e^{-\lambda_2 t} v_i| + \sigma_{\mathcal{D}}, \quad (4.15)$$

where $v_i \equiv v_2(i\Delta x)$ for $x \in [i\Delta x, (i+1)\Delta x)$ and $\sigma_{\mathcal{D}}$ is the noise in the \mathcal{D} measurement due to finite sampling (Eq. 4.8). The left-hand term in Eq. 4.15 is the L_1 distance between the discretized distributions $p(x, t)$ and $\pi(x; T_b)$. Thus, neglecting the terms for $k > 2$, we have

$$\begin{aligned} \mathcal{D}[p(x, t); \pi(x; T_b)] &\equiv \mathcal{D}(t) = |a_2(\alpha, T_0)| e^{-\lambda_2 t} \sum_{i=1}^{N_b} |v_i| + \sigma_{\mathcal{D}}, \\ &= |a_2(\alpha, T_0)| e^{-\lambda_2 t} V + \sigma_{\mathcal{D}}, \end{aligned} \quad (4.16)$$

where $V \equiv \sum_{i=1}^{N_b} |v_i|$. The $\mathcal{D}(t)$ plot typically has two regimes. The first corresponds to a fast initial relaxation, and the second to the slow barrier hopping. Note that the fast initial relaxation is absent in experiments starting at the cold temperature.

Following these points, we analyze the $\mathcal{D}(t)$ curves by extracting from them a quantity $\Delta\mathcal{D}$ that is sketched in Fig. 4.10A. For $a_2 \neq 0$, it may be estimated by globally fitting a single exponential to the long-time asymptotic regimes of all the T_h decays in Fig. 4.8, extrapolating back in time to find the intercept at $t = 0$, and subtracting the noise level $\sigma_{\mathcal{D}}$ resulting from finite sampling (Eq. 4.8). Thus, $\Delta\mathcal{D}$ is related to $|a_2(\alpha, T_0)|$ by

$$\Delta\mathcal{D} = |a_2(\alpha, T_0)| V. \quad (4.17)$$

For the fit based on Eq. 4.16, each $\mathcal{D}(t)$ decay curve has three parameters, a_2 , λ_2 , and V . The first, a_2 , depends on T_0 and α . The other two parameters, λ_2 and V , are common to all the data sets, as they depend only on the properties of the bath. Thus, the fit is local with respect to product $|a_2|V$ but global with respect to λ_2 . We note that it is also necessary to choose, by hand, the starting point for each decay curve. We verified that the values of the fit parameters are robust to the choice of starting point, typically varying by amounts consistent with the statistical estimates of the parameter error estimates.

After we have extracted the $\Delta\mathcal{D}$ values from the experiment, we fit to the data a prediction based on Eq. 4.17, using a_2 coefficients that are numerically calculated from Eq. 4.14. The remaining fit parameter V agrees with the numerically calculated value based on the eigenfunctions. For cases where $|a_2(\alpha, T_0)| \approx 0$, the decay is dominated by λ_3 , and thus the slow part of the distance curve is absent. In this case, we fit the region of the distance curve after the fast initial kinetic part reaches the noise level.

Carrying out the analysis sketched above, we extract $a_2(\alpha, T_0)$ and confirm that the Mpemba effect is indeed associated with an a_2 that decreases with the initial temperature (Fig. 4.10B). We fit the measured values of $\Delta\mathcal{D}(\alpha, T_0)$ with the numerical result from the FPE to estimate the scaling factor multiplying the $|a_2(\alpha, T_0)|$ coefficients. The scaling factor from the fit, 0.96 ± 0.03 , agrees with the numerical value ≈ 0.967 calculated using the FPE and its numerically determined eigenfunctions. The variation of $\Delta\mathcal{D}$ (and thus, a_2) with temperature for this fixed α shows non-monotonic behavior that also reflects the presence of the Mpemba effect. However, the eigenfunction analysis does not itself explain *why* the a_2 coefficient has a non-monotonic dependence on T_0 .

4.7 Strong Mpemba effect

To gain more physical insight, we conducted further experiments probing the Mpemba effect at fixed temperatures but variable asymmetry. In particular, we fixed the hot initial temperature $T_h = 1000$, which is so high that the initial probability density $p(x, 0) = \pi(x; T_h)$ is approximately a uniform distribution over the domain (x_{\min}, x_{\max}) . Figure 4.8B

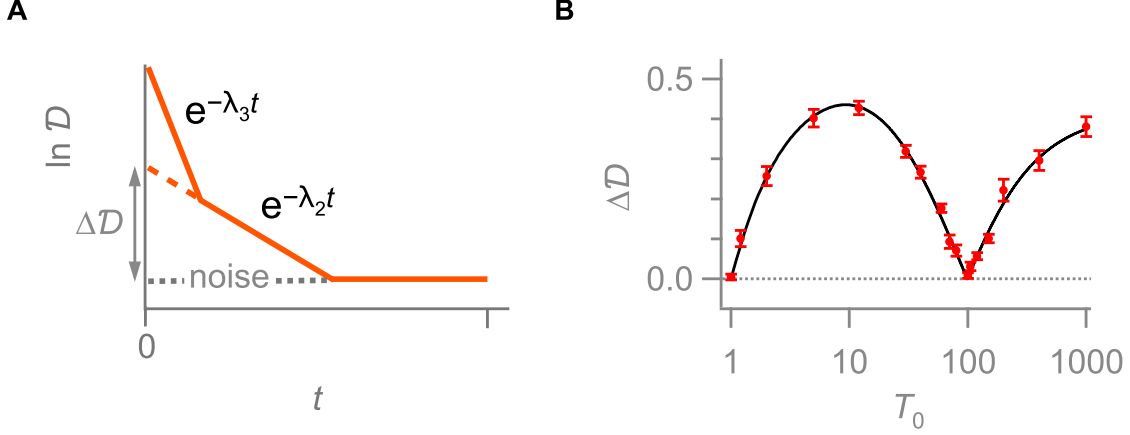


Figure 4.10: Measurements of $\Delta\mathcal{D}$ at fixed α . **A.** $\Delta\mathcal{D}$ is measured by extrapolating the long-time limit of the logarithm of the \mathcal{D} curve back to the quench time ($t = 0$). **B.** Markers are $\Delta\mathcal{D}$ measurements based on distance plots for different initial temperatures for $\alpha = 9$. Solid line in **B** is based on the calculated $|a_2(\alpha, T_0)|$ coefficient multiplied by an experimentally determined scaling factor (Eq. 4.17). The error bars represent one standard deviation and are calculated from the fits.

shows distance plots for different α , for hot and warm initial temperatures $T_h = 1000$, $T_w = 12$. As the asymmetry varies from $\alpha = 1$ to $\alpha = 9$, we see the same sequence of normal, anomalous (Mpemba), and normal relaxations to thermal equilibrium that we saw in Fig. 4.8A, where α was fixed and T_0 was varied.

Figure 4.11 shows the $\Delta\mathcal{D}$ ($\propto |a_2|$) values as a function of aspect ratio α for the warm and hot cases. We first notice that the value of the a_2 coefficient for the warm system is roughly constant, as increasing the asymmetry does not significantly change its initial state. The behavior of the a_2 coefficient for the hot system is more complicated. For small asymmetry, $|a_2(\alpha, T_w)| < |a_2(\alpha, T_h)|$, and the warm system cools down faster; i.e., $t_w < t_h$ (Eq. 4.42). This corresponds to normal cooling. For larger asymmetries, the situation is reversed, and we observe the Mpemba effect. For an asymmetry $\alpha \approx 3$, the $|a_2(\alpha, T_h)|$ coefficient vanishes. Such a situation corresponds to the recently identified strong Mpemba effect [253] and implies an exponential speed-up of the cooling process.

In the limit of large T_h , it is easy to understand this normal-anomalous-normal sequence of relaxation behavior. Because the initial probability density at T_h is approximately uniform, we can approximate the relative probability p_r to be in the right-hand domain $(0, x_{\max})$ as

$$p_r = \frac{|x_{\max}|}{|x_{\min}| + |x_{\max}|} = \frac{\alpha}{1 + \alpha}. \quad (4.18)$$

We can refer to this subset of initial conditions as the *ground-state basin* because it constitutes the states that, in the absence of thermal fluctuations, would flow into the

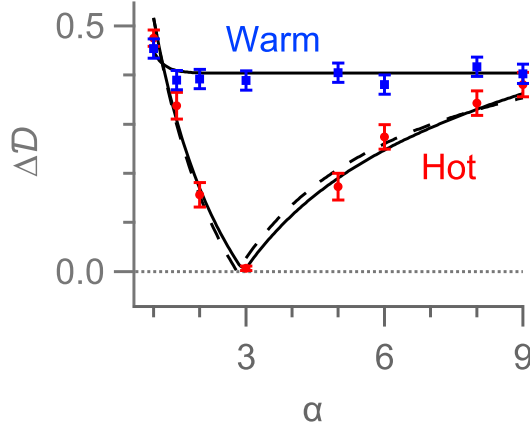


Figure 4.11: Measurements of $\Delta\mathcal{D}$ at fixed initial temperatures. Red and blue markers denote $\Delta\mathcal{D}$ measurements based on distance plots of the hot ($T_h = 1000$) and warm ($T_w = 12$) systems for different asymmetry coefficients. Solid line is based on the calculated $|a_2(\alpha, T_0)|$ coefficient multiplied by an experimentally determined scaling factor V (Eq. 4.17). Dashed line shows fit based on Eqs. (4.18), (4.19). The error bars represent one standard deviation and are calculated from the fits.

well corresponding to the stable state. Similarly, the metastable state attracts the initial conditions $(x_{\min}, 0)$, which may be termed the *metastable-state basin*. On the one hand, when the particle is released from its initial position to evolve under the influence of the potential, it rapidly moves to one of the two wells. Thus, after a fast transient, we expect the probability to be in the ground-state well to be $\approx p_r$. On the other hand, the measured probability for a system in thermal equilibrium (Fig. 4.1B) to occupy the ground state is $p_{r_0} \approx 0.7$. If the asymmetry α is chosen so that $p_r = p_{r_0}$, then the system will be in equilibrium after this initial transient. But for any other α , there will be a mismatch and $p_r \neq p_{r_0}$. The system will then relax to equilibrium by thermal hops over the barrier. This process is slowed by the Kramers factor $\exp(E_b/k_B T_b) \approx 7$ in our system, implying a longer time to reach equilibrium than processes that relax within a single local well.

The above argument leads to a simple prediction for the asymmetry dependence of the a_2 coefficient for the hot system in Fig. 4.11 and hence for $\Delta\mathcal{D}$. If the dynamic and the reference probabilities are close, we can approximate their difference using a Taylor expansion,

$$\Delta\mathcal{D}(\alpha, T) \propto |p_r - p_0|. \quad (4.19)$$

We then fit to the data shown in Fig. 4.11 (dashed line). The fit agrees well with the experimental observations and with a numerical calculation based on the FPE eigenfunctions (solid line).

4.8 Geometric interpretation of the Mpemba effect

The analysis based on the eigenfunction expansion of the probability density does not lead to good physical insight into the conditions needed to produce or observe the Mpemba effect. Here, we offer a more physical interpretation of the Mpemba effect explored so far.

4.8.1 Thermalization in a double-well potential with metastability

A common feature of experiments showing Mpemba effects is that they involve a temperature *quench*: the system is cooled very rapidly. We model this situation by making the high-temperature initial state an initial condition for dynamics that take place entirely in contact with a bath of fixed temperature. In effect, the quench is infinitely fast. We recall that the thermalization dynamics are given by the Langevin equation (Sec. 2.1)

$$\dot{x} = -\frac{U'(x)}{\gamma} + \sqrt{\frac{2k_{\text{B}}T_{\text{b}}}{\gamma}} \eta, \quad (4.20)$$

with γ a friction coefficient and $\eta(t)$ Gaussian white noise modeling thermal fluctuations from the bath, with $\langle \eta(t) \rangle = 0$ and $\langle \eta(t) \eta(t') \rangle = \delta(t - t')$. The noise-strength $2k_{\text{B}}T_{\text{b}}/\gamma$ enforces the fluctuation-dissipation relation [180, 254]. The potential $U(x)$ is a double-well potential with barrier height $E_0 \gg k_{\text{B}}T_{\text{b}}$ and two coarse-grained states, denoted L and R in Figure 4.12A. The range of particle motions is also constrained to a finite range; the potential is implicitly infinite at the extremities. By tilting the potential, one state has a higher energy than the other (difference is ΔE) and the potential becomes a toy model for the water-ice phase transition. However, the energy barrier E_0 , while high enough that the two states are well defined, is also low enough that many transitions over the barrier are observed during a typical experiment.

Figure 4.12 illustrates our experimental scenario, with **(A)** showing the potential and **(B)** the dynamics of a quench from a high temperature. With a moderately high barrier, both wells have significant probability for the equilibrium state $\pi(x, T_{\text{b}})$ (Figure 4.12B, right). For $U(x)$, the barrier $E_0 = 2.0$, the energy difference between states is $\Delta E = 1.3$, and the hot temperature $T_{\text{h}} = 1000$; energies are scaled by $k_{\text{B}}T_{\text{b}}$ and are, hence, dimensionless.

At a temperature corresponding to T_0 , the equilibrium free energy of the system is

$$F_{T_0}^{\text{eq}} = -k_{\text{B}}T_0 \ln Z \equiv -k_{\text{B}}T_0 \ln \left[\int_{-\infty}^{+\infty} dx \exp \left(-\frac{U(x)}{k_{\text{B}}T_0} \right) \right]. \quad (4.21)$$

and the corresponding equilibrium Boltzmann density is

$$\pi(x, T_0) = \frac{1}{Z} \exp \left[-\frac{U(x)}{k_{\text{B}}T_0} \right] = \exp \left[-\frac{U(x) - F_{T_0}^{\text{eq}}}{k_{\text{B}}T_0} \right], \quad (4.22)$$

The metastability of U means that the system evolves on two very different time scales:

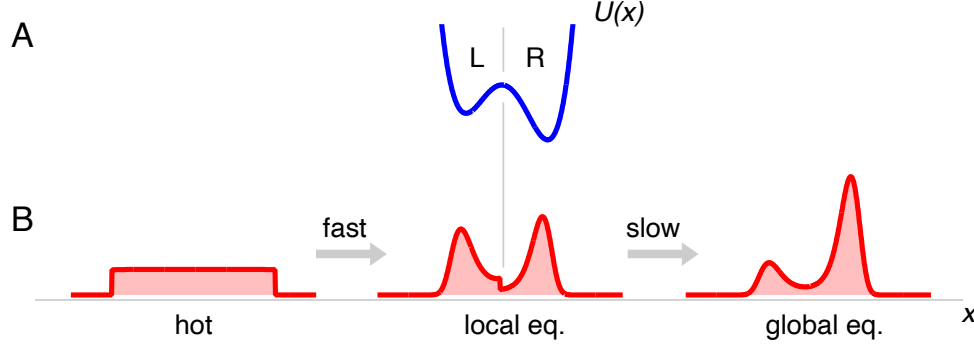


Figure 4.12: Two-stage dynamics. **A.** Tilted double-well potential $U(x)$ with coarse-grained states $\{L, R\}$. The potential includes infinitely steep walls at the domain boundaries (not shown). **B.** Evolution of the probability density function for position: a high-temperature equilibrium initial state $\pi(x; T_0)$ (left) has a fast relaxation to a local equilibrium state $p^{\text{leq}}(x; T_0, T_b)$ (middle) and a slow relaxation to global equilibrium $\pi(x; T_b)$ at the colder bath temperature (right).

Stage 1 is a fast relaxation to local equilibrium. The initial, high-temperature Boltzmann density rapidly evolves to a state that is at local equilibrium with respect to the bath temperature. A local equilibrium is a density that is similar locally to $\pi(x; T_b)$ but with altered fractions of systems in the left or right wells. Using marginalization and the definition of conditional probability, we can write such a local-equilibrium state as

$$p^{\text{leq}}(x; T_0, T_b) = P(\text{be in the left well at } T_0) P(x | \text{be in the left well at } T_b) \\ + P(\text{be in the right well at } T_0) P(x | \text{be in the right well at } T_b). \quad (4.23)$$

More precisely, the local equilibrium density is

$$p^{\text{leq}}(x; T_0, T_b) = \begin{cases} a_L \left(\frac{\pi(x; T_b)}{\int_{-\infty}^0 dx' \pi(x'; T_b)} \right) & x < 0 \quad (\text{left well}), \\ a_R \left(\frac{\pi(x; T_b)}{\int_0^{\infty} dx' \pi(x'; T_b)} \right) & x > 0 \quad (\text{right well}), \end{cases} \quad (4.24)$$

with $0 \leq a_L \leq 1$. Choosing $a_L + a_R = 1$ ensures normalization of the probability density.

In a fast quench, we assume that the fraction of initial systems at equilibrium at the higher temperature T_0 is unchanged when local equilibrium is established. Essentially, we ignore the diffusion of trajectories that start on one side of the barrier and end up on the other at the end of the transient. In this approximation, the fraction that ends up in each well corresponds to that of the initial state, $\pi(x; T_0)$. Thus,

$$a_L = \int_{-\infty}^0 dx' \pi(x'; T_0) \quad \text{and} \quad a_R = \int_0^{\infty} dx' \pi(x'; T_0). \quad (4.25)$$

As shown in Figure 4.12B, center, the local-equilibrium distribution $p^{\text{leq}}(x; T_0, T_b)$ is discontinuous at $x = 0$; higher barriers will reduce the discontinuity, of order $e^{-E_0/(k_B T_b)} \ll 1$ (see section 4.10.4).

Stage 2 is a final relaxation to global equilibrium on a slow time scale: the overall populations in each well (coarse-grained state) change, and the density converges to the Boltzmann density $\pi(x; T_b)$. Local equilibrium is maintained during the evolution, which is illustrated schematically in Fig 4.12B. In this *metastable regime*, the equilibration time was analyzed long ago by Kramers [180, 232, 255, 256]. It also corresponds to the long-time limit of Eq. 4.12; as a result, the final relaxation is exponential, with decay rate λ_2 .

4.8.2 Metastable Mpemba effect

Given this scenario of thermal relaxation as a two-stage process, we can readily understand how the Mpemba effect can occur. The idea is to follow the dynamics in the function space of all admissible probability density functions $p(x, t)$. If we expand the solution in eigenfunctions analogously to Eq. 2.55, we see that the infinite-dimensional function space is spanned by the eigenfunctions. To visualize the motion, we project it onto the 2D subspace spanned by the eigenfunctions $v_2(x)$ and $v_3(x)$. The system state is then characterized as a parametric plot of the amplitudes $a_2(t)$ and $a_3(t)$. A similar geometric plot was used to explore quenching in an anti-ferromagnetic Ising spin system in [253].

Figure 4.13 shows the geometry of trajectories. They are organized about two static, 1D curves, labeled G and G_{leq} . The red curve (G) represents the set of all equilibrium Gibbs-Boltzmann densities, $p(x; T_0)$, for $0 \leq T_0 < \infty$. It is sometimes known as the *quasi-static locus*. The green curve (G_{leq}) represents the set of all local-equilibrium densities of the form of Eq. 4.24, as parametrized by $a_L \in [0, 1]$. Both curves are represented as 2D parametric plots but lie in the full infinite-dimensional space. Both G and G_{leq} have finite length, in general. (The entire length is not shown in the figure.) The two curves intersect at $a_2 = a_3 = 0$, which describes the global equilibrium $\pi(x; T_b)$ with respect to the bath (large hollow marker with dot). The apparent crossing near $a_2 \approx 0.4$ is spurious, as the 3D projections in Fig. 4.13B show.

The dynamical trajectories are represented by the variously shaded gray curves. At time $t = 0$, the systems are in equilibrium along the red curve at a variety of temperatures $\{1, 1.2, 1.5, 3, 50, 100, 1000\} \times T_b$, which are indicated by black markers. The curves then move rapidly towards the green curve (local equilibrium). The time course is suggested by the dark-to-light gradient. Once they reach the vicinity of G_{leq} , they closely follow this green curve back to the global-equilibrium state.

Within this representation, we note the “arrival point” of each trajectory when it “hits” G_{leq} . For small temperatures (1, 1.2, 1.5, 3), the distance between this arrival point and the global-equilibrium state increases monotonically with T_0 . For larger temperatures (50, 100, 1000), however, the distance decreases until, at $T_0 = 1000T_b$, it nearly vanishes (denoting

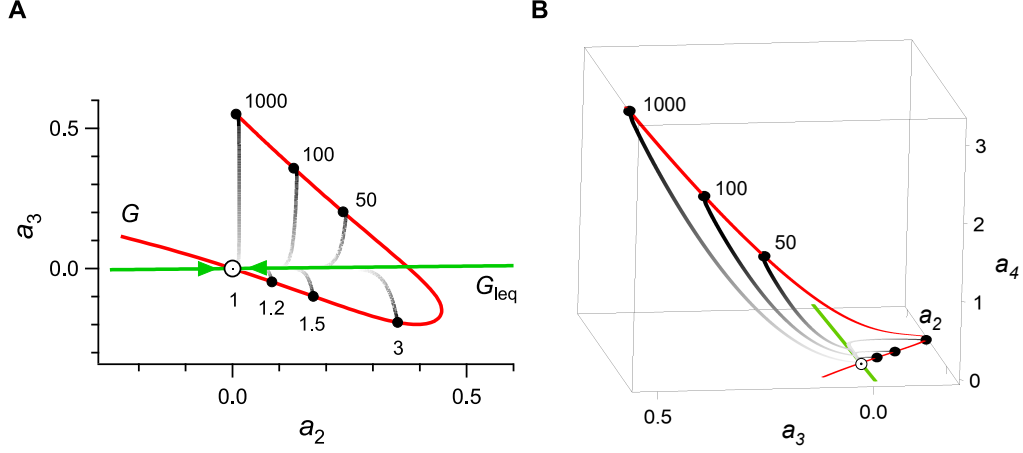


Figure 4.13: Dynamics of a_2 , a_3 , and a_4 coefficients. **A.** Probability-density dynamics in the plane defined by the a_2 and a_3 coefficients. The red curve G denotes the set of equilibrium densities, the green curve G_{leq} the set of local-equilibrium densities. Arrows indicate the slow relaxation along G_{leq} to global equilibrium, at the intersection with G (denoted by the large hollow marker with a dot at its center at $T_0 = 1$). Gray lines denote the rapid relaxation from an initial condition (temperature relative to the bath indicated by a marker along G). The time progression of $p(x, t)$, projected onto the a_2 – a_3 plane, is from dark to light. **B.** 3D projections of the a_2 , a_3 , and a_4 coefficients shown in **A**. Curves are calculated from the double-well potential described in Eq. 4.2, with domain asymmetry $\alpha = 3$.

the strong Mpemba effect). Along G_{leq} , the system is in the limit described by Eq. 4.12 and relaxes exponentially to global equilibrium. Relaxation along G_{leq} therefore *must* be monotonic with the distance away from global equilibrium. Trajectories that arrive along this curve that are farther from global equilibrium will take longer to relax. The Kullback-Leibler divergence D_{KL} between the local equilibrium density $p^{\text{leq}}(x; T_0, T_b)$ given in Eq. 4.24

and the global equilibrium density $\pi(x; T_b)$ can be written as

$$\begin{aligned}
D_{\text{KL}}(p^{\text{leq}}(x; T_0, T_b), \pi(x; T_b)) &= \int_{-\infty}^{\infty} dx p^{\text{leq}}(x; T_0, T_b) \ln \left[\frac{p^{\text{leq}}(x; T_0, T_b)}{\pi(x; T_b)} \right] \\
&= \int_{-\infty}^0 dx a_L \left(\frac{\pi(x; T_b)}{\int_{-\infty}^0 dx' \pi(x'; T_b)} \right) \ln \frac{a_L \pi(x; T_b)}{[\int_{-\infty}^0 dx' \pi(x'; T_b)] \pi(x; T_b)} \\
&\quad + \int_0^{\infty} dx a_R \left(\frac{\pi(x; T_b)}{\int_0^{\infty} dx' \pi(x'; T_b)} \right) \ln \frac{a_R \pi(x; T_b)}{[\int_0^{\infty} dx' \pi(x'; T_b)] \pi(x; T_b)} \\
&= a_L \ln \left(\frac{a_L}{a_L^*} \right) + a_R \ln \left(\frac{a_R}{a_R^*} \right) \\
&= D_{\text{KL}} \left[\begin{pmatrix} a_L \\ a_R \end{pmatrix}, \begin{pmatrix} a_L^* \\ a_R^* \end{pmatrix} \right]. \tag{4.26}
\end{aligned}$$

In the fourth line, $a_L^* \equiv \int_{-\infty}^0 dx \pi(x; T_b)$ and $a_R^* \equiv \int_0^{\infty} dx \pi(x; T_b)$. In the fifth line, the vectors represent two-state probability distributions. Note that in the “short Stage 1” approximation of Equation (4.25), the final expression for D_{KL} involves two coarse-grained probability distributions, with $\begin{pmatrix} a_L \\ a_R \end{pmatrix}$ depending only on T_0 and $\begin{pmatrix} a_L^* \\ a_R^* \end{pmatrix}$ only on T_b .

We then investigate the monotonicity of $D_{\text{KL}} \left[\begin{pmatrix} a_L \\ a_R \end{pmatrix}, \begin{pmatrix} a_L^* \\ a_R^* \end{pmatrix} \right]$ by differentiating:

$$\frac{dD_{\text{KL}}}{da_L} = \ln \left(\frac{a_L}{a_R} \right) - \ln \left(\frac{a_L^*}{a_R^*} \right), \tag{4.27}$$

which is positive for $a_L > a_L^*$ and negative for $a_L < a_L^*$. (Recall that $a_L + a_R = a_L^* + a_R^* = 1$.) Thus, $D_{\text{KL}}(p^{\text{leq}}, \pi)$ is monotonic in a_L on either side of equilibrium. In particular, $D_{\text{KL}}[p^{\text{leq}}(x; T_0, T_b), \pi(x; T_b)]$ is a monotonic function of a_L (defined in Eq. 4.25), which is the natural parameter for the manifold G_{leq} .

Now we can understand how the (metastable) Mpemba effect can arise. In the example shown in Fig. 4.13, the distance along G_{leq} initially increases with T_0 and so does the total equilibration time. But then this distance decreases for higher temperatures, leading to the Mpemba effect. We note that in our approximation, the time to traverse the initial stage is much shorter than the time to relax along the green curve, so that variations in the length of the initial trajectory are irrelevant.

If the bath temperature were changed at a finite rate (rather than a hot system being quenched directly into the bath), then the dynamics would be different. For example, if the system is very slowly cooled from the initial temperature to final bath temperature, the trajectory would follow the quasi-static locus (red curve G) and no Mpemba effect would be possible. Having shown that no Mpemba effect is possible with an infinitely slow quench and that the effect can be observed in the limit of an infinitely rapid quench, we can conclude that the Mpemba effect requires a *sufficiently fast* temperature quench.

4.8.3 Metastable Mpemba effect in terms of extractable work

Our final goal is to express the criterion for the Mpemba effect in more physical terms. For the metastable setting described above, we will find such a criterion in terms of a thermodynamic work. We recall that the second law of thermodynamics for a system in contact with a single thermal bath of temperature T_b can be expressed in terms of work and free energy rather than entropy:

$$W \geq \Delta F_{\text{neq}, T_b} , \quad (4.28)$$

where W is the work received by the system and ΔF_{neq} denotes the difference in *nonequilibrium free energies* (final – initial values). See, for example, [197], Eq. 5 and associated references.

We recall also that the nonequilibrium free energy generalizes the familiar notion of free energy to systems out of equilibrium. Thus, in analogy to Eq. 4.21, we define

$$F_{\text{neq}, T_b}(p) \equiv E(p) - k_B T_b S(p) , \quad (4.29)$$

where the average energy $E(p)$ and Gibbs-Shannon entropy $S(p)$ are given by

$$E(p) \equiv \int_{-\infty}^{+\infty} dx p(x) U(x) \quad \text{and} \quad S(p) \equiv - \int_{-\infty}^{+\infty} dx p(x) \ln p(x) . \quad (4.30)$$

These expressions reduce to their usual definitions for $p = \pi(x; T_b)$ but can be evaluated, as well, over nonequilibrium densities.

In the formulation of the second law of Eq. 4.28, the initial and final states are arbitrary. In our case, the initial state is the (approximate) local equilibrium reached at the end of Stage 1. In the final state, the system is in equilibrium with the bath.

Physically $-\Delta F_{\text{neq}}$ represents the maximum amount of work that may be extracted from the nonequilibrium isothermal protocol [257]. We will refer to this quantity as the *extractable work*.

$$W_{\text{ex}} \equiv -\Delta F_{\text{neq}, T_b} . \quad (4.31)$$

To derive the relationship between the difference in nonequilibrium free energies ΔF_{neq} and the Kullback-Leibler divergence [258], we begin with Eq. 4.26 as

$$\begin{aligned}
D_{\text{KL}}(p^{\text{leq}}, g) &= \int_{-\infty}^{\infty} dx p^{\text{leq}}(x) \ln \left[\frac{p^{\text{leq}}(x)}{\pi(x)} \right] \\
&= \int_{-\infty}^{\infty} dx p^{\text{leq}}(x) \ln p^{\text{leq}}(x) - \int_{-\infty}^{\infty} dx p^{\text{leq}}(x) \ln \pi(x) \\
&= -S(p^{\text{leq}}) - \int_{-\infty}^{\infty} dx p^{\text{leq}}(x) [-\beta_{\text{b}} U(x) + \beta_{\text{b}} F(\pi)] \\
&= -S(p^{\text{leq}}) + \beta_{\text{b}} [E(p^{\text{leq}})] - \beta_{\text{b}} F(\pi) \\
&= \beta_{\text{b}} [F(p^{\text{leq}}) - F(\pi)] .
\end{aligned} \tag{4.32}$$

To simplify notation, we have written p^{leq} for $p^{\text{leq}}(x; T, T_{\text{b}})$ and π for $\pi(x; T_{\text{b}})$. We can write Eq. 4.32 explicitly as

$$\Delta F_{\text{neq}} = - [F(p_{T, T_{\text{b}}}^{\text{leq}}) - F(\pi(T_{\text{b}}))] = -k_{\text{B}} T_{\text{b}} D_{\text{KL}}(p_{T, T_{\text{b}}}^{\text{leq}}, \pi(x; T_{\text{b}})) . \tag{4.33}$$

In our set-up, the extractable work between the “intermediate” time (end of Stage 1) where $F_{\text{neq}, T_{\text{b}}} = F_{\text{neq}, T_{\text{b}}}(p^{\text{leq}}(x; T_0, T_{\text{b}}))$, and the final time of the slow evolution (where $F_{\text{neq}, T_{\text{b}}} = F_{\text{eq}, T_{\text{b}}}$), is given by Eq. 4.33:

$$W_{\text{ex}}(T_0, T_{\text{b}}) = k_{\text{B}} T_{\text{b}} D_{\text{KL}}(p^{\text{leq}}(x; T_0, T_{\text{b}}), \pi(x, T_{\text{b}})) . \tag{4.34}$$

In Sec. 4.8.2 and Fig. 4.13, we saw that $D_{\text{KL}}(p^{\text{leq}}(T_0, T_{\text{b}}), \pi T_{\text{b}})$ can be non-monotonic as a function of T_0 . We thus conclude that there can be a non-monotonic dependence on T_0 of the function

$$T_0 \longmapsto W_{\text{ex}}(T_0, T_{\text{b}}) . \tag{4.35}$$

This is the main result of this section: If the metastable Mpemba effect occurs, then the extractable work from the local-equilibrium state at the end of Stage 1 is non-monotonic in the initial temperature T_0 . Figure 4.14 shows an example, again calculated for the potential described by Eq. 4.2.

In addition to having a clear physical interpretation, $W_{\text{ex}}(T_0, T_{\text{b}})$ is easily calculated as a simple numerical integral of equilibrium Boltzmann distributions for two temperatures. By contrast, to establish the non-monotonicity of a_2 , the criterion of [186], one must first find the left eigenfunction u_2 by solving the boundary-value problem associated with the adjoint Fokker-Planck operator. Note that in this geometric picture, the local equilibrium G_{leq} lies approximately along the a_2 axis and thus is equivalent to the picture previously established (see Eq. 4.12). In this picture, the dynamics, in the long-time limit, were governed by the a_2 coefficients.

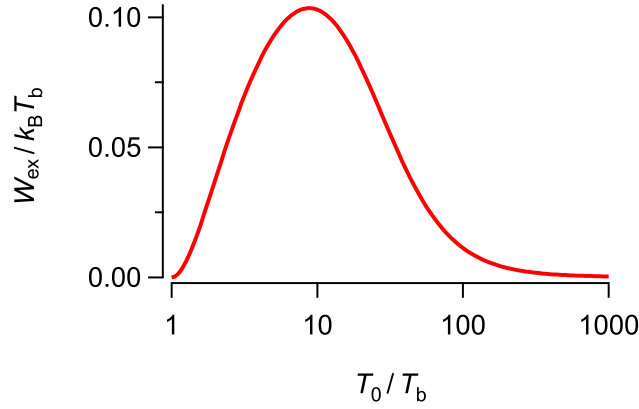


Figure 4.14: Extractable work is a non-monotonic function of initial temperature T_0 for the double-well potential of Figure 4.12A.

4.9 Discussion

The results presented in this chapter experimentally demonstrate the Mpemba effect. We have shown that the Mpemba effect is defined by a non-monotonic dependence of relaxation time on initial temperature. Using our understanding of the phenomenology of the Mpemba effect, we identified special combinations of experimental parameters where the a_2 coefficient vanishes (strong Mpemba effect), which correspond to exponentially faster cooling. For a 1D potential with a metastable and a stable minimum, we presented a geometric interpretation of the effect as a two-stage relaxation in the function space of all admissible probability densities. In such a situation, we showed that the Mpemba effect is associated with a non-monotonic temperature dependence of the maximum extractable work of the local equilibrium state at the end of Stage 1, which is a much more physical quantity than a_2 coefficients.

4.10 Supplementary information

4.10.1 Infinite potential vs. finite potential

A systematic deviation in the imposed potential from the desired shape arises because the initial conditions for the cooling experiment were calculated assuming infinite walls at the domain boundaries. However, physically imposing an infinite potential wall is impossible, meaning that there is a maximum possible force exerted by the virtual potential while the particle is evolving towards equilibrium with the bath. Nevertheless, we can and do take into account the infinite walls in creating the initial conditions for particles released in the potential. In almost all cases, the inward forces cause the particles to move towards positions in the interior of the experimental domain. In rare cases, a fluctuation from the bath can briefly push a particle outside the domain defined by the infinite walls. Thus, particles moving in the physically imposed potential can have motion that violates very slightly the potential assumed in defining the initial conditions and assumed in calculating quantities such as the eigenfunctions of the FPE.

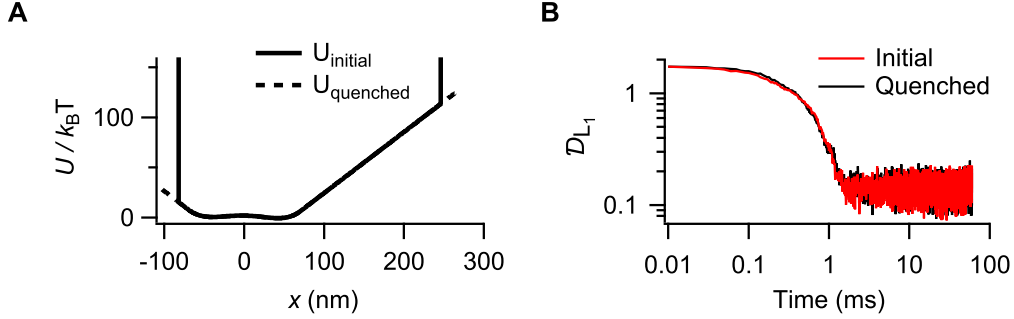


Figure 4.15: **Finite maximum slope of the potential does not affect particle dynamics significantly.** **A.** The energy landscape for the Mpemba effect. Solid line depicts the initial energy landscape with infinite potential walls at the domain boundaries. The equilibrium distribution of the particle is calculated based on this potential (U_0). Dashed line shows the potential (U_{quenched}) in which the particle is quenched. **B.** Langevin simulations of the Mpemba effect using both potentials show no significant differences between the two cases.

To test whether such violations are important, we simulate the overdamped particle motion in the feedback trap using a discretized Langevin equation [231]

$$x_{n+1} = x_n + \frac{1}{\gamma} F_n \Delta t + \xi_n,$$

$$\bar{x}_{n+1} = x_n + \chi_n, \quad (4.36)$$

where x_n is the true position of the particle, \bar{x}_n the observed position at time t_n , and ξ_n and χ_n are the integrated thermal and measurement noises. The force $F_n = -\partial_x U(\bar{x}_n, \Delta t)$

is applied at a deterministic time step of $\Delta t = 10 \text{ } \mu\text{s}$. Langevin simulations based on Eq. (4.36) for both the idealized and physical potentials (Fig. 4.15) show that these small violations have no significant effect on the quantity of interest, the distance function \mathcal{D} . As an independent, experimental assessment, we have also measured the fraction of time that a particle spends outside the box created by the infinite walls of the assumed potential. Analyzing the particle trajectories, we find that such excursions occur only during 0.003% of the total time of the experiment.

4.10.2 Calculation of equilibration time

We define the equilibration time t_{eq} to be the time when the distance curve $\mathcal{D}(t)$ reaches the noise level $\sigma_{\mathcal{D}}$. By equating the terms on the right hand side of Eq. 4.16, we can determine the time when the slow decay of the distance curve intersects the noise floor, thus reaching equilibrium. The condition implies

$$\sigma_{\mathcal{D}} = |a_2(\alpha, T_0)| e^{-\lambda_2 t_{\text{eq}}} V = \Delta \mathcal{D} e^{-\lambda_2 t_{\text{eq}}} . \quad (4.37)$$

Solving for t_{eq} gives

$$t_{\text{eq}} = \frac{1}{\lambda_2} \ln \left[\frac{\Delta \mathcal{D}}{\sigma_{\mathcal{D}}} \right] . \quad (4.38)$$

With normally distributed uncertainties for λ_2 and $\Delta \mathcal{D}$, the variance of t_{eq} is

$$\sigma_{t_{\text{eq}}}^2 \approx \left(\frac{\partial t_{\text{eq}}}{\partial \lambda_2} \right)^2 \sigma_{\lambda_2}^2 + \left(\frac{\partial t_{\text{eq}}}{\partial \Delta \mathcal{D}} \right)^2 \sigma_{\Delta \mathcal{D}}^2 + 2 \left(\frac{\partial t_{\text{eq}}}{\partial \lambda_2} \frac{\partial f}{\partial \Delta \mathcal{D}} \right) \sigma_{\lambda_2 \Delta \mathcal{D}} , \quad (4.39)$$

where σ_{λ_2} is the standard deviation of λ_2 , $\sigma_{\Delta \mathcal{D}}$ the standard deviation of $\Delta \mathcal{D}$, and $\sigma_{\lambda_2 \Delta \mathcal{D}}$ the covariance between λ_2 and $\Delta \mathcal{D}$. Using Eqs. 4.38 and 4.39, we can write the fractional uncertainty in the equilibration time as

$$\frac{\sigma_{t_{\text{eq}}}}{t_{\text{eq}}} = \left[\left(\frac{\sigma_{\lambda_2}}{\lambda_2} \right)^2 + \frac{1}{t_{\text{eq}}^2 \lambda_2^2} \left(\frac{\sigma_{\Delta \mathcal{D}}}{\Delta \mathcal{D}} \right)^2 + \frac{2}{t_{\text{eq}} \lambda_2} \left(\frac{\sigma_{\lambda_2 \Delta \mathcal{D}}}{\lambda_2 \Delta \mathcal{D}} \right) \right]^{1/2} . \quad (4.40)$$

The typical fractional uncertainties in these variables are $(\sigma_{\lambda_2}/\lambda_2) \approx 0.04$, $(\sigma_{\Delta \mathcal{D}}/\Delta \mathcal{D}) \approx 0.05$, and $\sigma_{\lambda_2 \Delta \mathcal{D}}/(\lambda_2 \Delta \mathcal{D}) \approx -0.0001$, where $\lambda_2 \approx 0.3 \text{ ms}^{-1}$ and t_{eq} varies within the range 1–20 ms. From Eq. 4.40, the fractional uncertainty in a typical data for the equilibration time is $(\sigma_{t_{\text{eq}}}/t_{\text{eq}}) \approx 0.04$ –0.13. Although these are typical numbers, the calculation in Eq. 4.40 is repeated for each data point in Fig. 4.7. A separate fit is performed in each case, with separate fit parameters and parameter uncertainties.

Finally, because the uncertainty of the noise level $\sigma_{\mathcal{D}}$ is determined from a long baseline, its fractional value (≈ 0.006) is nearly ten times smaller than other fractional uncertainties and does not appreciably alter the uncertainty estimate. We thus neglect it in our analysis.

4.10.3 Equilibration time versus the a_2 coefficient

To explicitly relate the equilibration time to $a_2(\alpha, T_0)$ for the hot and warm cases, we rewrite Eq. 4.16 at times t_h and t_w as

$$\mathcal{D}[p(x, t_w); \pi(x; T_b)] = |a_2(\alpha, T_w)| e^{-\lambda_2 t_w} V + \sigma_{\mathcal{D}}, \quad (4.41a)$$

$$\mathcal{D}[p(x, t_h); \pi(x; T_b)] = |a_2(\alpha, T_h)| e^{-\lambda_2 t_h} V + \sigma_{\mathcal{D}}, \quad (4.41b)$$

where t_w and t_h are the equilibration times for the warm and hot systems, respectively. After both systems have reached equilibrium, the instantaneous value of their L_1 distances from the equilibrium value fluctuates at a typical noise level of $\sigma_{\mathcal{D}}$ (Eq. 4.8). Equating the two identical average values and simplifying gives

$$t_w - t_h = \frac{1}{\lambda_2} \ln \frac{|a_2(\alpha, T_w)|}{|a_2(\alpha, T_h)|}. \quad (4.42)$$

Although t_w and t_h both increase as the noise level of the distance measure is reduced, their difference is independent of the noise level (Fig. 4.16). Thus, no matter what the noise

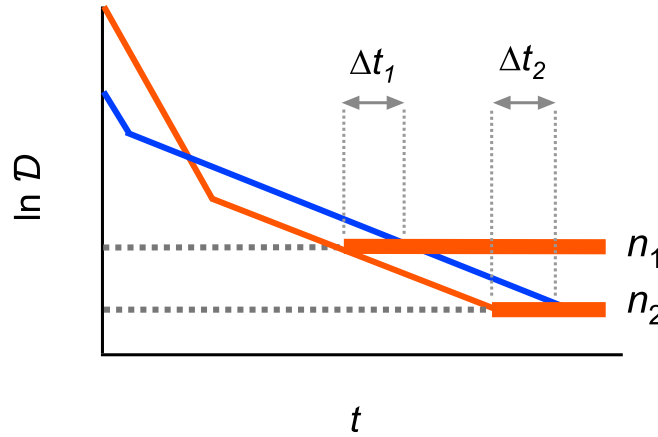


Figure 4.16: Different noise levels do not affect the difference in equilibration time. The hot (red) and warm (blue) systems have the same slope at large times (set by the potential energy). The signal decreases until it hits one of two different noise levels, n_1 or n_2 (indicated by thick red lines and horizontal dashes). The difference in the equilibration time is independent of the noise levels: $\Delta t_1 = \Delta t_2 = t_w - t_h$.

level in the estimates of probability densities, assuming $a_2 \neq 0$, we will always reach an unambiguous conclusion concerning the presence of the Mpemba effect. For $|a_2(\alpha, T_w)| > |a_2(\alpha, T_h)|$, the warm system lags the hot, and the Mpemba effect is observed.

4.10.4 Barrier height vs. discontinuity in local equilibrium

The local-equilibrium distribution as defined in Eq. 4.24 has a jump discontinuity at $x = 0$. Here, we show that higher barriers of the potential will reduce the discontinuity of the local-equilibrium distribution.

We begin by computing the limit of $p^{\text{leq}}(x; T_0, T_b)$ as x approaches 0. For x approaching 0 from the left, we have

$$p^{\text{leq}}(0^-) = \lim_{h \rightarrow 0} p^{\text{leq}}(-h; T_0, T_b) = \lim_{h \rightarrow 0} \int_{-\infty}^0 dx' \pi(x'; T_0) \left(\frac{\pi(-h; T_b)}{\int_{-\infty}^0 dx' \pi(x'; T_b)} \right). \quad (4.43)$$

For x approaching 0 from the right, we have

$$p^{\text{leq}}(0^+) = \lim_{h \rightarrow 0} p^{\text{leq}}(h; T_0, T_b) = \lim_{h \rightarrow 0} \int_0^{\infty} dx' \pi(x'; T_0) \left(\frac{\pi(h; T_b)}{\int_0^{\infty} dx' \pi(x'; T_b)} \right). \quad (4.44)$$

To find the discontinuity of $p^{\text{leq}}(x; T_0, T_b)$ at $x = 0$, we compute the difference between $p^{\text{leq}}(h^-)$ and $p^{\text{leq}}(h^+)$,

$$\begin{aligned} p^{\text{leq}}(0^-) - p^{\text{leq}}(0^+) &= \lim_{h \rightarrow 0} \int_{-\infty}^0 dx' \pi(x'; T_0) \left(\frac{\pi(-h; T_b)}{\int_{-\infty}^0 dx' \pi(x'; T_b)} \right) \\ &\quad - \lim_{h \rightarrow 0} \int_0^{\infty} dx' \pi(x'; T_0) \left(\frac{\pi(h; T_b)}{\int_0^{\infty} dx' \pi(x'; T_b)} \right), \\ &= \frac{\int_{-\infty}^0 dx' \pi(x'; T_0)}{\int_{-\infty}^0 dx' \pi(x'; T_b)} \times \lim_{h \rightarrow 0} \pi(-h; T_b) \\ &\quad - \frac{\int_0^{\infty} dx' \pi(x'; T_0)}{\int_0^{\infty} dx' \pi(x'; T_b)} \times \lim_{h \rightarrow 0} \pi(h; T_b). \end{aligned} \quad (4.45)$$

Since $\pi(x, T_b)$ is continuous at $x = 0$, $\lim_{h \rightarrow 0} \pi(-h; T_b) = \lim_{h \rightarrow 0} \pi(h; T_b) = \pi(0; T_b)$. Thus,

$$p^{\text{leq}}(0^-) - p^{\text{leq}}(0^+) = \pi(0; T_b) \left[\frac{\int_{-\infty}^0 dx' \pi(x'; T_0)}{\int_{-\infty}^0 dx' \pi(x'; T_b)} - \frac{\int_0^{\infty} dx' \pi(x'; T_0)}{\int_0^{\infty} dx' \pi(x'; T_b)} \right]. \quad (4.46)$$

The terms within the square brackets vanish when $T_0 = T_b$, which gives a trivial solution: $p^{\text{leq}} = \pi$, and there is no discontinuity at $x = 0$. When $T_0 \neq T_b$, the bracket is a constant that can be either positive or negative. Thus,

$$|p^{\text{leq}}(0^-) - p^{\text{leq}}(0^+)| \propto \pi(0; T_b) = e^{-\frac{E_b}{k_B T_b}}. \quad (4.47)$$

We conclude that increasing the barrier height E_b reduces the discontinuity at $x = 0$.

Chapter 5

Inverse Mpemba effect

In Chapter 4, we demonstrated how the Mpemba effect could be observed in a controlled setting in colloidal systems. In this chapter, we ask whether it is possible to observe a complementary “inverse” effect where an initially cold system heats up faster than an initially warm system, when coupled to a bath at high temperature. Recently, Lu and Raz first predicted the inverse Mpemba effect in the Ising model [186]. It was then also predicted in numerical studies of granular systems [43], spin glasses [45], inertial suspensions [47, 48], and molecular gases [46]. Analogous to the strong Mpemba effect discussed in Chapter 4 for the usual “forward” Mpemba effect, a *strong* inverse Mpemba effect was predicted by Klich et al. [253].

Although, to our knowledge, there has been no experimental evidence for the inverse Mpemba effect in any system, there does exist a well-known heating phenomenon, known as the *Leidenfrost effect*, that dates back to the 18th century [259]. The effect is characterized by a significant reduction in heat transfer from a heated body to liquids when the temperature of the body crosses a threshold temperature, known as the Leidenfrost Point (LP). This phenomenon occurs when liquid droplets are deposited on hot solid surfaces and a layer of vapor is formed in between the droplet and substrate. The high-pressure vapor layer prevents contact between the hot surface and the droplet. The layer thus reduces the heat transfer between them, allowing the droplets to survive much longer than normally expected. When the surface temperature is lower than the boiling point of the liquid, the droplets spread over the substrate to form a thin layer and evaporate slowly. Upon further increase in temperature, a maximum rate of evaporation is achieved at a critical temperature (also known as the Nukiyama temperature, T_N) corresponding to the minimum survival time of the droplets [260]. Beyond T_N , the survival time rapidly increases and reaches a maximum value at the LP temperature. Thus, the survival times of the liquid droplets are non-monotonic with the temperature of the surface [261, 262].

Although the effect is not the same as the inverse Mpemba effect, it is superficially similar: it shares the counterintuitive, non-monotonic temperature dependence on the time to reach the final state—a high-temperature bath for the Mpemba effect and a gas phase in

	Leidenfrost effect	Inverse Mpemba effect
Initial state	nonequilibrium state at a lower chemical potential	equilibrium state at a lower temperature
Reservoir	temperature and chemical potential reservoirs	temperature reservoir
Initial temperature	T_b (reservoir temperature)	$T_0 (< T_b)$
Final temperature	T_b	T_b
Mechanism	local heating of droplets	relaxation to equilibrium
Final state	equilibrium state at a higher chemical potential	equilibrium state at a higher temperature

Table 5.1: Comparison between the Leidenfrost and inverse Mpemba effects.

equilibrium with a low-temperature bath for the Leidenfrost effect. Both effects also involve anomalous heating. Differences between the two effects are listed in Table 5.1. Although the underlying mechanism for the Leidenfrost effect is well understood, the inverse Mpemba effect has only recently been predicted. In this chapter, based on the understanding gained from the usual forward Mpemba effect, we design an experiment that gives the first evidence for the inverse Mpemba effect.

The content of this chapter is available on [arxiv.org](https://arxiv.org/abs/263) [263].

5.1 Energy landscape for the inverse Mpemba effect

We place a one-dimensional potential asymmetrically in the domain $[x_{\min}, x_{\max}]$ as

$$U(x) \equiv \begin{cases} -F_{\max}x & x < x_{\min} \\ U_0(x) & x_{\min} \leq x \leq x_{\max} \\ F_{\max}x & x > x_{\max} , \end{cases} \quad (5.1)$$

where $U_0(x)$ is given by

$$U_0(x) = E_b \left[1 - 2 \left(\frac{x}{x_m} \right)^2 + \left(\frac{x}{x_m} \right)^4 - \frac{1}{2} \left(\frac{x}{x_m} \right) \right] , \quad (5.2)$$

with a very low barrier $E_b = 0.0002$ and $x_m = 40$ nm (Fig. 5.1). The steep walls at the domain boundaries corresponding to the maximum force F_{\max} applied by the optical tweezers define a box in which a particle relaxes. To create an instantaneous “heating quench”, we sample initial positions from the Boltzmann distribution $\pi(x; T_0) \propto \exp[-U(x)/k_B T_0]$. The initial positions are sampled assuming $U(x)$ to have infinite potential walls at the domain boundaries.

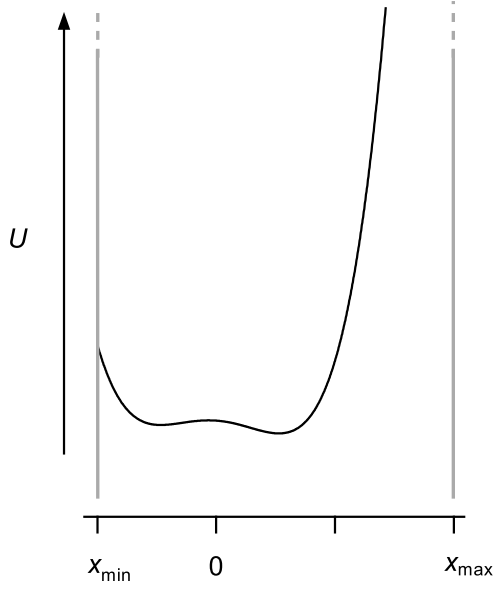


Figure 5.1: Schematic of the energy landscape $U(x)$ used to explore the inverse Mpemba effect, set asymmetrically ($\alpha = 2$) within a box $[x_{\min}, x_{\max}]$ with potential walls with finite slope at the domain boundaries.

5.2 Inverse Mpemba effect in an asymmetric potential

To determine how the inverse Mpemba effect depends on the initial temperature of the system, we perform a “heating quench” in a bath of fixed temperature and described by Eq. 5.1. After a particle is released in the bath at $t = 0$ at a low temperature T_0 , it explores all the possible macrostates and finally equilibrates with the bath, which is at temperature $T_b > T_0$. Figure 5.2A–C shows example time traces of evolution in the potential $U(x)$. Frequency estimates of the probability density function $p(x, t)$ that records the system states between the initial state $\pi(x; T_0)$ and $\pi(x; T_b)$ are calculated from the time traces. Figure 5.3A shows the measured times to reach equilibrium for systems that start at different initial temperatures. For $T_0/T_b > 1 \times 10^{-3}$, the equilibration time decreases monotonically as the initial temperature of the system approaches the bath temperature T_b , and follows normal heating ($t_c > t_w$). However, at a lower initial temperature range $1 \times 10^{-5} < T_0/T_b < 10^{-3}$, the equilibration time decreases as the initial state of the system gets colder and thus corresponds to anomalous heating ($t_c < t_w$). For lower temperatures ($T_0/T_b < 1 \times 10^{-5}$), the equilibration time increases again, exhibiting normal heating. Thus, we observe a sequence of normal, anomalous, and normal relaxations to thermal equilibrium. Figure 5.3B shows the measured $\Delta\mathcal{D}$ values as a function of initial temperature T_0 . The $\Delta\mathcal{D}$ values correlate with the measured equilibration times.

As described by Eq. 5.3, the variations in $U_0(x)$ across the domains are $\ll k_B T$, and the dynamics at the bath temperature are approximated by simple diffusion (Eq. 2.37). To make the experiment even simpler to analyze, we can consider a bath that has an effectively infinite temperature. The equilibrium state is then a uniform density between x_{\min} and x_{\max} , and the dynamics of the system are governed by the diffusion equation (Sec. 2.2.3). Although the approximation to infinite temperature is impractical for real objects, we use it to simplify the dynamical equation governing thermal relaxation. We will see later in this chapter that we can then calculate the eigenvalues and eigenfunctions of the FP operator analytically. Using the eigenfunction, we can then easily find an analytical expression for the a_2 coefficient as a function of initial temperature of the system.

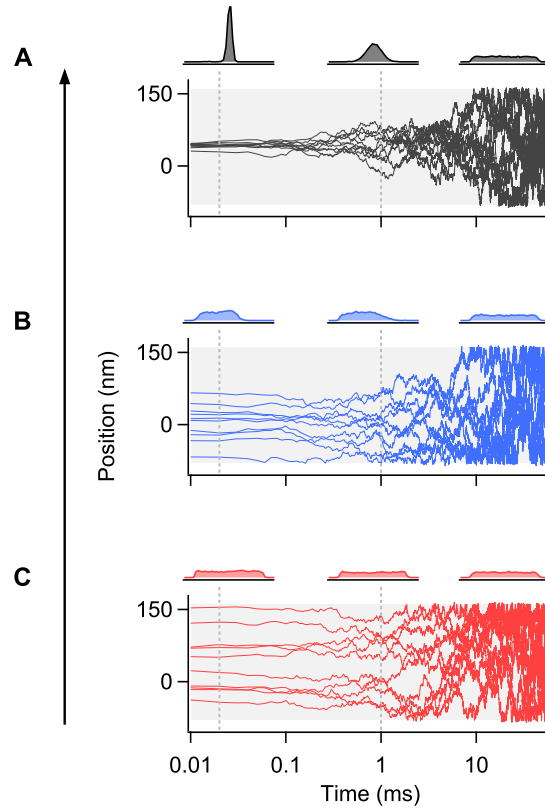


Figure 5.2: Dynamic trajectories relaxing to equilibrium at a hot temperature. Ten trajectories of a particle released from the equilibrium distribution at temperatures $T_0 = 4 \times 10^{-4} T_b$ (black, **A**), $4 \times 10^{-3} T_b$ (blue, **B**) and $T_b = 1$ (red, **C**) into the hot bath, with the evolving probability density $p(x, t)$ shown for three times (estimated based on 5000 trajectories) on a logarithmic time scale. The shaded gray region corresponds to a box size of $x_{\max} - x_{\min} = 240$ nm.

Figure 5.4**A** shows the distance curves $\mathcal{D}(t)$ for systems at different initial temperatures (red curves) relaxing to thermal equilibrium (black curve) in a flat potential bounded by very steep walls. For the region in Fig. 5.4**B** with a negative slope, an initially cold system

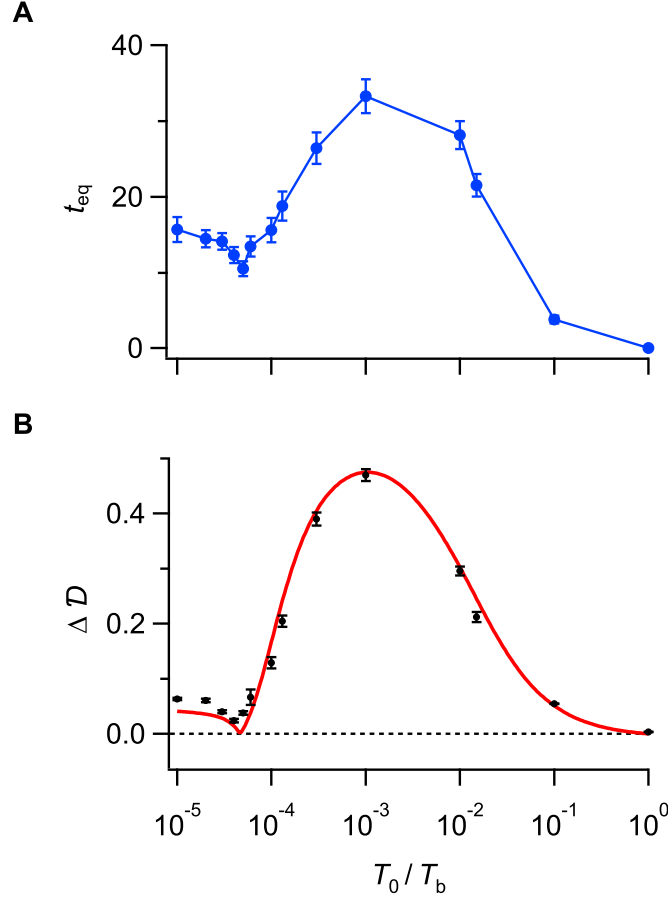


Figure 5.3: Equilibration time and $\mathcal{D}(t)$ as a function of initial system temperature for a quench in a bath at finite temperature. **A.** The equilibration times for systems at different initial temperatures. **B.** Markers are $\Delta \mathcal{D}$ measurements based on distance plots for different initial temperatures. The solid red line is based on $|\Delta \mathcal{D}|$ values calculated using the FPE.

starts at a larger distance from equilibrium than a warm system but eventually equilibrates first, illustrating again the inverse Mpemba effect.

5.3 Analysis based on eigenfunction expansion

When the bath temperature is effectively infinite, the quenched dynamics for $p(x, t)$ obey the ordinary diffusion equation. For free diffusion ($U = 0$), the evolution of the probability density $p(x, t)$ of particle positions is described by the Fokker-Planck equation as

$$\frac{\partial p}{\partial t} = \frac{k_B T_b}{\gamma} \frac{\partial^2 p}{\partial x^2} \equiv \mathcal{L}_{\text{free}} p, \quad (5.3)$$

where $\mathcal{L}_{\text{free}}$ is the Fokker-Planck operator for a freely diffusing particle. Unlike the Fokker-Planck operator \mathcal{L}_{FP} in Eq. 4.10, $\mathcal{L}_{\text{free}}$ is Hermitian, implying that the left eigenfunction

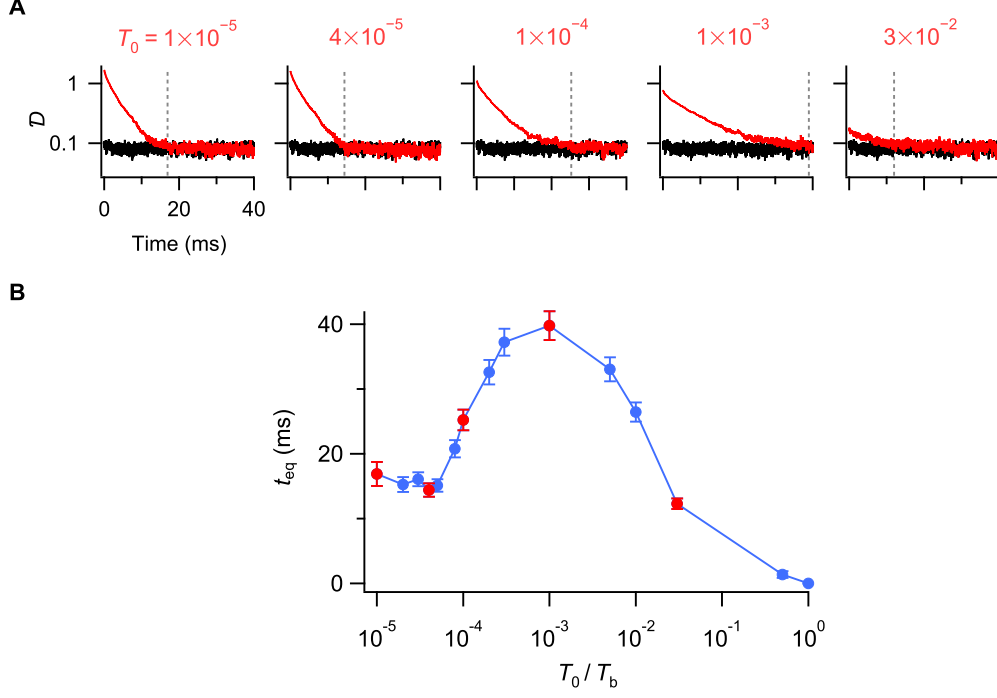


Figure 5.4: Equilibration time and distance $\mathcal{D}(t)$ as a function of initial system temperature for a quench in a bath at infinite temperature. **A.** L_1 distances for systems with initial temperature $T_c = 1 \times 10^{-5}, 4 \times 10^{-5}, 1 \times 10^{-4}, 1 \times 10^{-3}, 3 \times 10^{-2}$ that heat up in a bath at temperature $T_b = 1$. The thin vertical lines represent the times when systems starting with different initial temperatures reach the equilibrium. **B.** The equilibration times for systems at different initial temperatures. The red markers represent the temperatures for which $\mathcal{D}(t)$ has been plotted in A.

u_2 and the right eigenfunction v_2 are identical. Following the argument in Sec. 4.6, we can approximate the underlying probability density $p(x, t)$, at long times, as

$$p(x, t) \approx \pi(x; T_b) + a_2(\alpha, T_0) e^{-\lambda_2 t} v_2(x; \alpha, T_b). \quad (5.4)$$

Equation 5.3 has the same form as the heat equation discussed in Sec. 2.3 and can be solved analytically for its eigenfunctions. The boundary conditions discussed in Eqs. 2.29 and 2.33 are identical for a flat potential ($U = 0$):

$$\left. \frac{\partial p}{\partial x} \right|_{x=x_{\min}} = \left. \frac{\partial p}{\partial x} \right|_{x=x_{\max}} = 0. \quad (5.5)$$

Imposing the boundary condition described in Eq. 5.5, we find the eigenfunctions of $\mathcal{L}_{\text{free}}$ as

$$u_k = v_k = \frac{1}{Z'} \cos \left[\frac{(k-1)\pi}{L} (x - x_{\min}) \right], \quad (5.6)$$

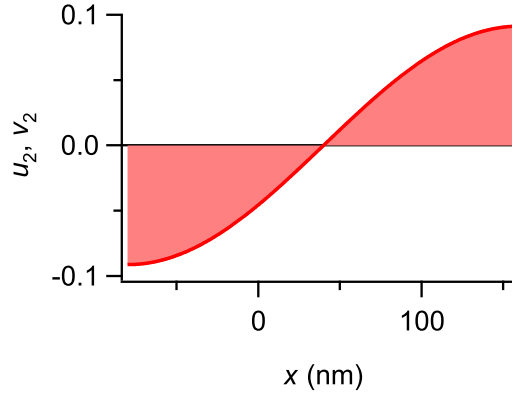


Figure 5.5: The second eigenfunction, which corresponds to the smallest non-zero eigenvalue of the Fokker-Planck operator.

where Z' is the normalization constant, defined such that $\langle u_k v_k \rangle = 1$, and where $L = x_{\max} - x_{\min}$ and $k = 2, 3, \dots$. Following the analysis done in Sec. 4.6.2, we measure $\Delta\mathcal{D}$ as a function of initial temperature from $\mathcal{D}(t)$. Figure 5.6 shows the non-monotonic temperature dependence of $\Delta\mathcal{D}$. To see the agreement of the measured values of $\Delta\mathcal{D}$ with theoretical predictions, we explicitly calculate a_2 coefficients using Eqs. 4.14 and 5.6. We fit the data with the predicted a_2 curve to measure the scaling factor V , as described in Eq. 4.17. The scaling factor from the fit, 1.561 ± 0.001 , agrees to $\approx 0.1\%$ with the numerical value ≈ 1.559 calculated using the numerically determined eigenfunctions.

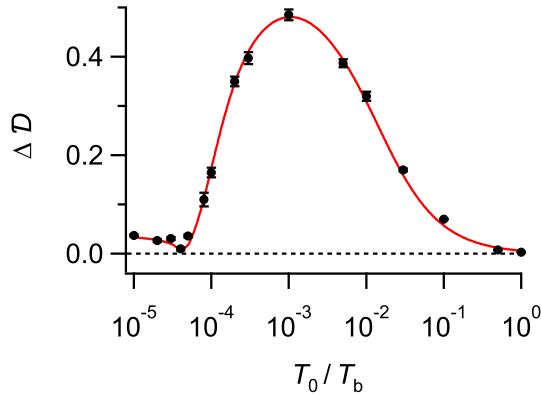


Figure 5.6: Measurements of $\Delta\mathcal{D}$ for a bath at an effectively infinite temperature. Markers are $\Delta\mathcal{D}$ measurements based on distance plots for different initial temperatures. The solid red line is based on the calculated $|\Delta\mathcal{D}|$ values using FPE. The error bars represent one standard deviation and are calculated from the fits.

For cases where $|a_2(T_0) \approx 0|$, the decay is dominated by λ_3 and represents an exponential speed-up of the heating process compared to decays at temperatures where $|a_2(T_0)| \neq 0$.

Such a situation corresponds to the *strong* inverse Mpemba effect. The transient decay at the time scale set by the eigenvalue $\lambda_2^{-1} \approx 16.66$ ms disappears, and the system quickly reaches equilibrium. To summarize our results, for $|a_2(\alpha, T_w)| > |a_2(\alpha, T_c)|$, the initially warm system lags the initially cold system, and the inverse Mpemba effect is observed. A similar conclusion can be drawn from the relationship between the difference in equilibration time of the cold and warm systems and the associated a_2 coefficients using Eq. 4.42.

5.4 Discussion

Our results give the first experimental evidence for the inverse Mpemba effect. The non-monotonic dependence of the equilibration time on the initial temperature of the system can be understood through the non-monotonicity of a_2 coefficients. We first observed the inverse Mpemba effect for a quench in a heat bath at finite temperature. To gain more insight and understand the underlying mechanism, we also showed that there is an anomalous heating effect for a bath at an effectively infinite temperature. The heating of a system to a heat bath at infinite temperature has the same qualitative features as the heating of a system to a bath at finite temperature. In this temperature limit, the relaxation dynamics are governed by a simple diffusion equation, and we calculated the analytical expression for the eigenfunctions and determined the a_2 coefficients as a function of initial temperature. For both finite- and infinite-temperature cases, we found evidence for the strong inverse Mpemba effect, where the systems heated up exponentially faster than those under typical conditions.

We can offer some insight as to why it was easier for us (and perhaps others) to observe the forward Mpemba effect compared to the inverse effect. When a system relaxes to a bath at temperature T_b , the time-scale separation between the decay curves corresponding to λ_3 and λ_2 depends on the ratio $\Lambda = \lambda_3/\lambda_2$. Consequently, the greater the value of Λ , the stronger will be the time-scale separation of the corresponding decay curves, and thus, easier to observe experimentally. Particularly, in order to measure the $\Delta\mathcal{D}$ ($\propto a_2$) values, we fit the part of the decay curve that corresponds to λ_2 . Thus, a clear separation between λ_2 and λ_3 is necessary to accurately measure the $\Delta\mathcal{D}$ values.

For the forward Mpemba effect, studied in Chapter 4, the system cools from a hot temperature to a cold temperature in a double-well potential, and the ratio Λ of eigenvalues λ_3 to λ_2 (i.e., $\Lambda_{\text{for}}^* \equiv \lambda_3/\lambda_2$) is ≈ 16.1 . However, for the inverse Mpemba effect, the ratio of eigenvalues is $\Lambda_{\text{inv}}^* \approx 4.03$. Thus, Λ_{inv}^* is about four times smaller in the case of heating.

A natural question arises whether these are general expectations for Λ_{for} and Λ_{inv} or are they just a feature of our potential. In Chapter 4, we observed that the dynamics of $a_2(t)$ correspond to hops over the barrier. We thus expect that the ratio of eigenvalues λ_3 to λ_2 depends on the barrier height E_b as $\Lambda_{\text{for}} \sim \exp[E_b/k_B T_b]$. As a result, for a bath at low temperature, Λ_{for} is controlled by the barrier-height of the potential and may be

even greater for a higher barrier (Fig. 5.7, red curve). However, for a bath at an effectively infinite temperature, $\Lambda_{\text{inv}} \approx 4$ and is independent of the shape of the potential, including its barrier-height (Fig. 5.7, blue curve). Thus, all systems at high temperature will have an approximately flat energy landscape, and one may expect low values of Λ for all such systems. Even at high temperatures where $E_b \ll 1$, we expect similarly small values of Λ_{for} . Thus, we generally expect $\Lambda_{\text{for}}/\Lambda_{\text{inv}} > 1$ for situations where the forward and inverse Mpemba effects are each observed.

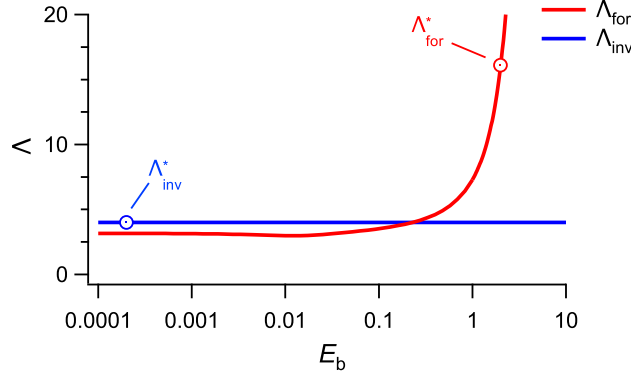


Figure 5.7: Ratio Λ of eigenvalues λ_3 to λ_2 of the Fokker-Planck operator as a function of barrier height E_b at the bath temperature $T_b = 1$. The red curve is for the double-well potential used in Chapter 4 for the forward Mpemba experiments, and the blue curve is for the flat potential used in the inverse Mpemba experiments. The hollow red marker denotes the ratio Λ_{for}^* used in the forward Mpemba experiments, that corresponds to $E_b \approx 2$. The hollow blue marker denotes the ratio Λ_{inv}^* for the flat potential ($E_b \approx 0$) used in the inverse Mpemba experiments.

The asymmetry of Λ_{for} vs. Λ_{inv} has experimental consequences. In general, as our experimental results confirm, it is easier to resolve the contribution of sums of exponentials when the exponents have significantly different values. Thus $\Lambda_{\text{for}}/\Lambda_{\text{inv}} > 1$ implies that a forward Mpemba effect will be easier to observe than an inverse effect. This asymmetry will be particularly important for potentials with metastable states separated by high barriers. Although we used $E_b \approx 2$ in our forward Mpemba experiments, larger barrier heights would further increase the separation in time scales. However, increasing the barrier height would increase the equilibration time exponentially and make large number of trials of the experiment inconvenient to obtain. Finally, note that for the forward Mpemba experiments, we used different initial temperatures and barrier-height of the potential. The red curve in Fig. 5.7 shows that a large value of $\Lambda_{\text{for}}^* \approx 16$ is obtained for the barrier $E_b \approx 2$. If the experiment were done in the potential $U(x)$ as described in Chapter 4 with a very small $E_b \approx 0.0002$, Λ_{for} would have been small, and it would have been difficult to observe the Mpemba effect.

Chapter 6

Higher-order Mpemba effect

In Chapters 4 and 5, we presented experimental evidence for anomalous cooling and heating in colloidal systems. Specifically, in Chapter 4, we gave an explanation as to why it was reasonable to see the Mpemba effect in a system with a tilted double-well potential. More fundamentally, one can ask what shapes of potentials and choices of temperatures can lead to the Mpemba effect. Based on the results shown in Chapter 4, one may speculate that asymmetry of the potential plays a role. In our experiment, the symmetry was broken by both the tilt in the double-well potential and the asymmetric placement of the potential in a domain. We showed explicitly in Chapter 4 that the Mpemba effect was not observed when the potential was placed symmetrically in a given domain. Thus, the results shown in Fig. 4.7 suggest that symmetry plays a key role for the effect. However, in this chapter, we will show that asymmetry is *not* necessary and that it is possible to observe the Mpemba effect in a symmetric potential in a symmetric domain, i.e., one where $U(x) = U(-x)$. Since the symmetry of the potential enforces a_2 coefficients to zero, we observe, as a consequence, a *higher-order* Mpemba effect.

6.1 Experiment

We construct a one-dimensional, symmetric, virtual, double-well potential using our feedback trap setup. The potential $U(x)$ is piecewise continuous: a double well joined by linear regions at the extremes. The symmetric double-well potential is given as

$$U_0(x) = E_b \left[1 - 2 \left(\frac{x}{x_m} \right)^2 + \left(\frac{x}{x_m} \right)^4 \right], \quad (6.1)$$

with $E_b = 2.5$ and $x_m = 40$ nm. Note that the tilt term $\sim \Delta E$ (c.f. Eq. 4.1) is not present. With a symmetric double-well potential U_0 in the middle, the overall potential energy landscape $U(x)$ within a box $[-x_{\max}, x_{\max}]$ is described by Eq. 4.2 (Fig. 6.1). To create an instantaneous quench, we sample initial positions from the Boltzmann distribu-

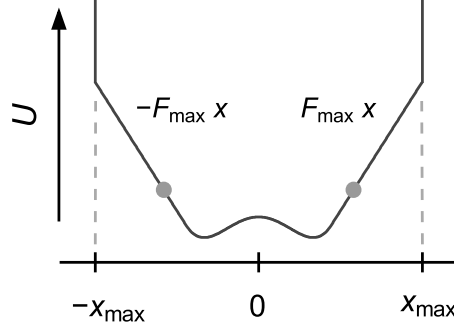


Figure 6.1: Schematic of the energy landscape for the Mpemba effect in a symmetric double-well potential. The gray markers denote positions $|x_1| = x_r \approx 56$ nm, where the slope of the potential corresponds to the maximum force exerted by the optical tweezers.

tion $\pi(x; T_0) \propto \exp[-U/k_B T_0]$ (Fig. 6.2A), assuming infinite potential walls at the domain boundaries (Fig. 6.1).

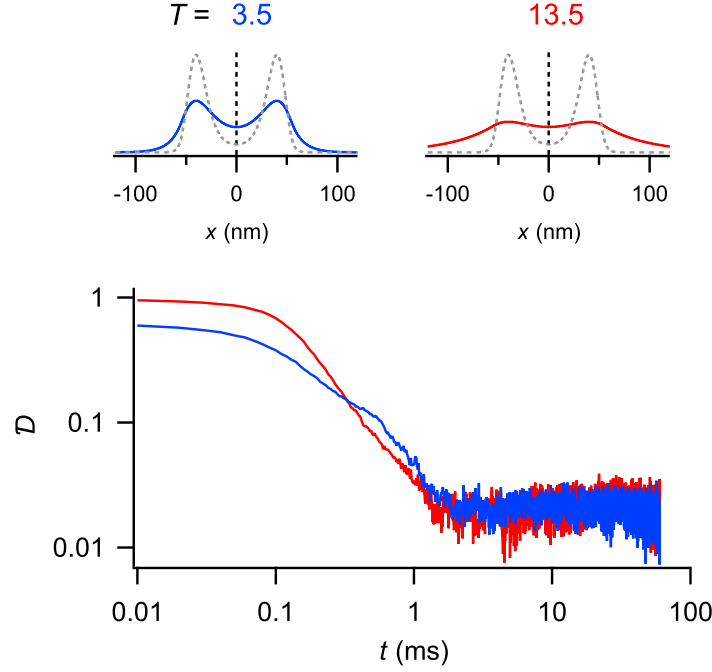


Figure 6.2: Equilibration in a symmetric potential. **A.** The solid blue and red lines represent the probability density $p(x, 0) = \pi(x; T_0)$ of systems initially at temperatures $T_0 = 3.5$ and 13.5 , respectively. The dashed gray line represents the equilibrium probability density at the bath temperature. **B.** The L_1 distances calculated for systems at two different temperatures ($T_h = 13.5$ and $T_w = 3.5$). The cold distance plot is a control experiment where the system prepared at the bath temperature T_b relaxes to the same temperature. The domain size is 240 nm.

After an instantaneous quench at $t = 0$, the particle relaxes (cools) in the imposed virtual potential $U(x)$ for 60 ms. We repeat this protocol 30,000 times to create a statistical ensemble from which the state of the system at each time step is estimated to measure the L_1 distance. Figure 6.2B shows the L_1 distances for systems initially prepared at temperatures $T_0 = \{1, 3.5, 13.5\}$. Although the initially hot system starts with a greater magnitude of $\mathcal{D}(t)$ than that of the initially warm system, the former reaches equilibrium first. The crossing between the corresponding $\mathcal{D}(t)$ curves and the monotonic decrease of the L_1 distance with time confirm the presence of the Mpemba effect in the symmetric potential.

6.2 Eigenfunction analysis

To understand the underlying mechanism behind anomalous cooling in a symmetric potential, we again look at the left and right eigenfunctions of the FPE. For a symmetric potential in a domain, the eigenfunctions alternate in index between having even and odd symmetry, with the ground state (Boltzmann distribution) being even, since $\pi(x; T_b) = Z^{-1} \exp[-U(x)/k_B T_b] = \pi(-x; T_b)$, given that $U(x) = U(-x)$ [264]. Thus, by symmetry, the even terms in the eigenfunction expansion of $p(x, t)$ should be odd functions. As a consequence, the calculation of all the even coefficients (i.e., a_k , where $k = 2, 4, 6, \dots$) of the Fokker-Planck involves integrating an even function $\pi(x; T_b)$ against odd eigenfunctions. Then, without doing any calculation, we can say that the a_2 coefficients should be zero in a symmetric double-well potential. To test this argument based on symmetry, we numerically calculated the second and third right eigenfunctions for the potential $U(x)$ (Fig. 6.3). We then explicitly confirmed that the a_2 coefficients are indeed zero in this case (Fig. 6.4, blue curve). As a result, at long times, the probability density is dominated by the first and *third*

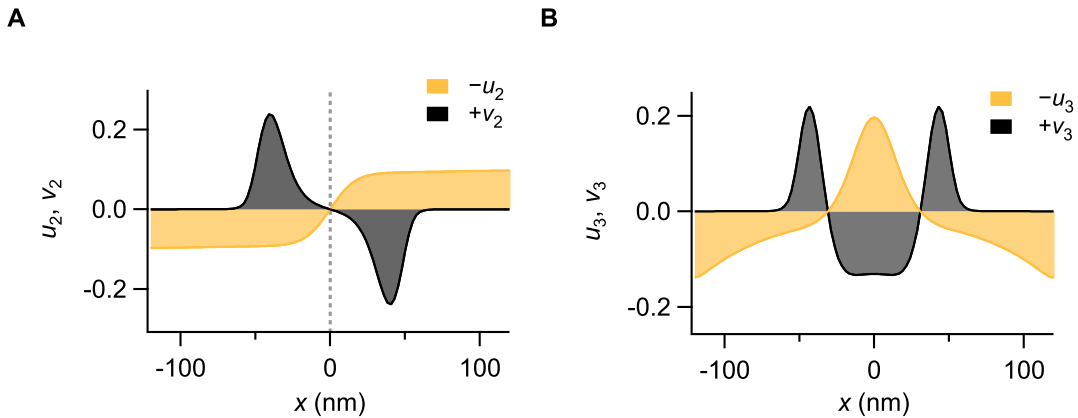


Figure 6.3: Eigenfunctions of the FP operator for a symmetric potential. **A.** $u_2(x)$ and $v_2(x)$ are the left and right eigenfunctions, respectively, and correspond to the second eigenvalue of the FP operator. **B.** $u_3(x)$ and $v_3(x)$ are the third left and right eigenfunctions, respectively for the same FP operator.

terms of Eq. 4.11:

$$p(x, t) \approx \pi(x; T_b) + a_3(\alpha, T_0) e^{-\lambda_3 t} v_3(x; \alpha, T_b). \quad (6.2)$$

Thus, we consider the next higher-order eigenfunction to check for non-monotonicity with respect to the initial temperature. The third left and right eigenfunctions are shown in Fig. 6.3B. The a_3 coefficients calculated numerically based on u_3 and v_3 indeed have a non-monotonic dependence on the initial temperature. Recalling that the Mpemba effect exists if $|a_3(T_h)| < |a_3(T_w)|$, we thus predict that the hotter system at T_h will reach equilibrium faster than the initially warm system at $T_w = 3.5$ for $T_h = [3.5, 60]$. We refer to anomalous relaxation where the decay rate is dominated by λ_3 as a *higher-order* Mpemba effect. For $T_0 \approx 13.5$, the system will relax to equilibrium as a single exponential as $|a_3(T_0)| \approx 0$. Thus, the decay rate will be dominated by λ_4 , illustrating the *strong* higher-order Mpemba effect in the symmetric double-well potential.

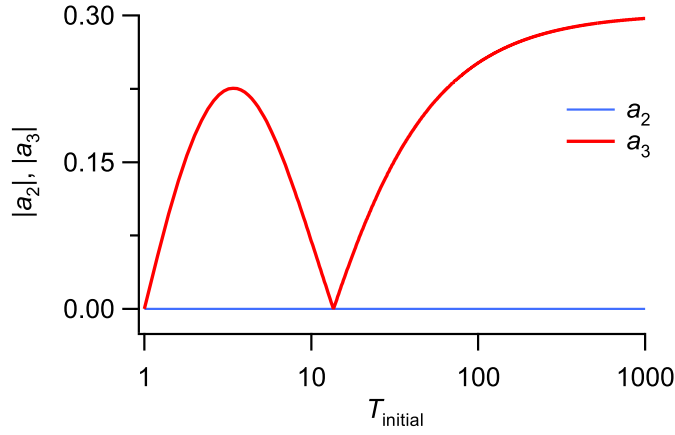


Figure 6.4: Relaxation in a symmetric potential. Solid red and blue lines are the numerically calculated $|a_2|$ and $|a_3|$ coefficients for different initial temperatures using the FPE.

6.3 Mpemba effect in a potential with one local minimum

The experimental observation and the predicted numerical results shown in Figs. 6.2 and 6.4 indicate that the Mpemba effect is present in the case of a symmetric potential. One can ask a closely related question: whether a double-well structure is necessary for the effect. The results based on the a_2 coefficients suggest that one should expect the Mpemba effect in the half domain $[0, x_{\max}]$ of the potential shown in Fig. 6.1. Note that this potential shape has only one local minimum (Fig. 6.5A). The a_2 coefficients are then non-zero, in general, as there is no longer a reflection symmetry in the shape of this potential. A numerical calculation based on the FP equation suggests that relaxation in this single-well potential is dominated by the $|a_2|$ values and indeed has non-monotonic dependence on the initial

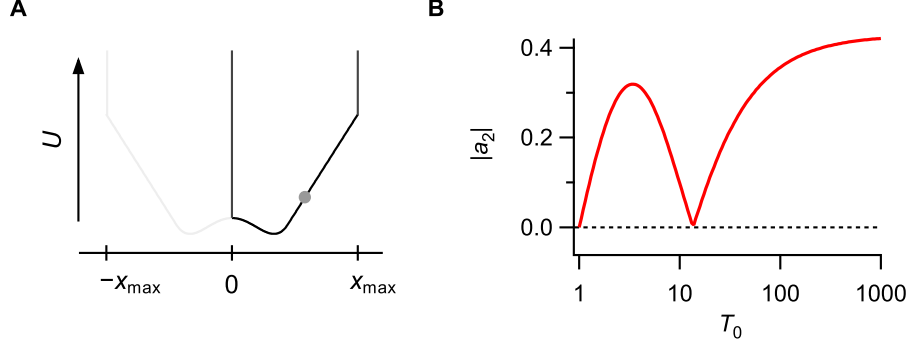


Figure 6.5: Mpemba effect in a potential with one local minimum. **A.** Schematic of the energy landscape. **B.** Decay coefficients $|a_2|$ as a function of initial temperature $T_0 > T_b$.

temperature of the system (Fig. 6.5B). Interestingly, for $T_0 \approx 14$, we predict a strong Mpemba effect corresponding to $|a_2| = 0$.

6.4 Discussion

In this chapter, we have explored relaxation in a symmetric potential. Intuitions based on the results in Chapter 4 suggested that the Mpemba effect could not be observed in a symmetric potential. Nonetheless, we did observe anomalous relaxations in this case. We realized that, for a symmetric potential, the a_2 coefficient always vanishes. Consequently, when released from a cold temperature to a bath at a high temperature, the particle dynamics are governed by a_3 coefficients. For these reasons, the Mpemba effect that we observe experimentally in a symmetric, double-well potential is necessarily a higher-order effect, linked to the a_3 coefficients. Thus, we can say that asymmetry is not a necessary condition for the Mpemba effect.

Based on our observation in a symmetric potential, we further predict that the Mpemba effect can also be present in a domain that is half the symmetric potential. Although we did not have time to test this prediction experimentally, we performed simulations of the Fokker-Planck equation that support the existence of the Mpemba effect in this potential, which has but one well. The effect, in this case, is particularly interesting because there is no coarse-grained second state. Thus, the predicted result dissociates the Mpemba effect from metastability and emphasizes that the effect is not limited to systems undergoing phase transitions. A more detailed analysis of the particle dynamics would be required to accurately explain the anomalous relaxation in this case. More experiments will need to be done to search for the predicted non-monotonicity in $\Delta\mathcal{D}$ values with initial temperature of the system and to test the detailed numerical predictions.

Chapter 7

Conclusions

The Mpemba effect refers to systems whose thermal relaxation time is a non-monotonic function of the initial temperature. Thus, a system that is initially hot cools to a bath temperature more quickly than the same system, initially warm. Originally observed in water, the Mpemba effect has also been studied both experimentally and numerically in a wide variety of systems. However, all of these systems—water especially—remain mysterious, as no consensus exists as to the underlying cause. The major drawbacks in previous experiments in water are that the results were hard to reproduce and were based on a small number of trials, which led to large scatter in the freezing times. Freezing is indeed a stochastic process and may depend on the details of the sample preparation. Thus, the definition of the Mpemba effect based on freezing times is ambiguous. In this thesis, we began by defining the Mpemba effect in terms of *equilibration times*—time elapsed between initial and final equilibrium states. Our definition remains independent of whether a system undergoes a phase transition or not. We have experimentally shown evidence for the Mpemba effect, the inverse Mpemba effect, and the higher-order Mpemba effect in systems that lacked phase transitions. Our study gives insight into a long-standing problem and represents the first case of this kind of anomalous relaxation where quantitative agreement between a predictive theory and experiment is observed.

7.1 Summary of the results obtained

I began my thesis work by building a feedback-based optical tweezers setup. Feedback traps are versatile tools that can create arbitrary energy landscapes. Although my focus was mainly to create one-dimensional potentials in this thesis, feedback traps can be extended in three dimensions to create more complex energy landscapes. I constructed virtual potential landscapes such as harmonic and double-well potentials to benchmark the performance and accuracy of the setup. These potentials were constructed on ≈ 100 nm length scales.

In the study of the Mpemba effect, I used the feedback traps to create a tilted double-well potential on nanometer length scales, with dynamical time scales on the order of millisec-

onds. The advantage of creating a potential on such a small scale with faster characteristic time was twofold. First, the system could equilibrate faster with the bath; and second, the fast equilibration times allowed the repetition of the cooling/heating protocol thousands of times. A direct way to observe the evolution of a system between two states at different temperatures is to measure the temperature at each time step. However, cooling/heating by quenching is a nonequilibrium process. As a result, the intermediate states of the system are not well described by a single temperature. Thus, we adopted the notion of distance functions that measure a dynamical state's distance from the state at thermal equilibrium. In our work, we used primarily the L_1 distance and occasionally the Kullback-Leibler divergence as proxies for temperature. We showed that the observation of the Mpemba effect was independent of the choice of distance functions, provided they obeyed certain temperature-like properties [186].

A key feature of the potential used in the Mpemba experiment is its asymmetry. The asymmetry was present in the form of tilt in the potential and its placement in an asymmetric domain. The two wells of the potential at different energy constituted two coarse-grained states. We referred to the well corresponding to the higher energy level as a metastable state and the well corresponding to the lower energy level as a stable state. After a system was quenched to the double well at the bath temperature, dynamics occurred in two stages: a fast relaxation to local equilibrium, followed by a slow equilibration of populations in each coarse-grained state. The time scales of the fast and slow relaxation stages were controlled by the slope of the potential near boundaries and the energy-barrier height, respectively, for a given domain size. The relaxation dynamics were understood through the eigenfunction expansion of the Fokker-Planck operator. Lu and Raz proposed that the projection of the initial state of system onto the slowest eigenfunction of the Fokker-Planck operator a_2 could be non-monotonic in temperature and thus might lead to the Mpemba effect. We experimentally measured the non-monotonic temperature dependence of the a_2 coefficient. We also found the condition for the strong Mpemba effect predicted by Klich et al., where $|a_2| = 0$ [253]. At such a point, the slowest relaxation dynamics is $\sim e^{-\lambda_3 t}$, implying an exponential speed-up over the generic relaxation dynamics, $\sim e^{-\lambda_2 t}$.

Perhaps the spectacular observation was the inverse Mpemba effect. This anomalous heating effect had been predicted by theory but never observed [43, 45–48, 186]. We showed the first experimental evidence for the inverse Mpemba effect in a colloidal system. Analogous to the forward Mpemba effect, the non-monotonic temperature dependence of the a_2 coefficients led to the anomalous heating effect. For heating in a bath at effectively infinite temperature, we could simplify the Fokker-Planck equation and derive simple analytical expressions for the eigenfunctions. We then calculated the a_2 coefficients as a function of temperature and observed agreement within 0.01% with the experimentally measured $\Delta\mathcal{D}$ ($\propto |a_2|$) values. We also found the strong inverse Mpemba effect where $|a_2| \approx 0$. Although our measurements were well aligned with predictions based on the Fokker-Planck equation,

we do not have a simple, geometric interpretation of the effect. However, one may look at the dynamic probability densities as the system evolves in the bath to understand the heating process.

Having observed the forward and the inverse Mpemba effects, one question that naturally arises is what kind of potentials can lead to a Mpemba effect. Is asymmetry a necessary condition for anomalous relaxation? To investigate this question, I designed a double-well potential (with no tilt) placed in a symmetric domain. Surprisingly, we could still observe the Mpemba effect. Since the a_2 coefficients vanish for symmetric potentials, the relaxation dynamics were controlled by a_3 , the projection of the initial state on the next (third) slowest eigenfunction. The non-monotonicity of a_3 coefficients with temperature, as predicted by the FP equation, were identified with a higher-order Mpemba effect. Inspired by the results for the symmetric potential, we predicted that the Mpemba effect could be observed in a potential with one local minimum only. The breaking of symmetry again restored the non-monotonicity of a_2 coefficients. We also predicted the existence of the strong Mpemba effect in this case. But we did not have time to complete experiments to test these last predictions.

7.2 Final remarks

The results presented in this thesis give insight into a long-standing problem of anomalous cooling. The significance of observing the Mpemba effect in a colloidal system is twofold: First, simplicity brings clarity. The agreement shown with a simple theory based on eigenfunction expansions of the FPE contrasts with the more complicated, yet inconclusive analyses of the ice-water system [19, 20, 23, 25–27, 29, 33, 34, 242, 243, 265, 266]. More constructively, the physical insights gained from the study of a simple system may guide future investigations of more complicated systems. For example, while many authors have asserted that freezing plays an essential role in the water experiments [243], there is no phase transition in the experiments reported here. Although the tilted double-well potential used in the forward Mpemba experiments may serve as a toy-model for water-ice phase transition, the predictions based on potential with no coarse-grained metastable state indicate that phase transition may not be a key requirement for the effect. It will be interesting to see such effects in an experiment, as it will add further evidence that the Mpemba effect need not be associated with a phase transition.

The second significant point of the colloidal experiments is to show that the ice-water system is not unique. The analysis used here constitutes a *general* mechanism for anomalous relaxation phenomena. The situation is analogous to that of phase transitions, where general physical theories (mean-field and Landau theories, renormalization group) [267] contrast with theories for specific cases such as the ice-water transition. Detailed theories for specific systems can account for important phenomena in a given system, for exam-

ple, how additives increase the attainable supercooling in water and help insects survive sub-freezing temperatures [268], while general theories such as we have applied suggest how similar behavior can arise in a wide variety of settings and materials. More broadly, thermal relaxation and heat removal remain important technological challenges. For example, they limit the performance of microprocessors and other integrated circuits [269]. Engineering Mpemba-like effects into technologically relevant materials might offer new and important strategies to rapidly remove heat from localized sources.

More sophisticated time-dependent protocols can also be envisioned that steer dynamical trajectories to desired outcome states. A recent theory by Gal and Raz along these lines shows that an initial cooling can actually speed up *heating times* exponentially [270]. Their theory predicts that such exponential heating can also be achieved in systems that do not exhibit the inverse Mpemba effect. The theory should be relevant for a wide range of systems. It will be an interesting project to see whether such a scenario can be observed using our setup.

Finally, while the findings of our study provide some insight into the anomalous behavior associated with both cooling and heating, they do not immediately explain the Mpemba effect in water. Whether due to supercooling of water below 0 °C, dissolved minerals or gases, or H-bond interaction, understanding the Mpemba effect in water still stands as an open problem. Philip Ball once wrote, “And even if the Mpemba effect is real—if hot water can sometimes freeze more quickly than cold—it is not clear whether the explanation would be trivial or illuminating” [271]. On this front, whatever the eventual explanation for the behavior in water, I am confident that it will belong to the classes of mechanisms explored in this thesis.

Bibliography

- [1] I. A. Campbell and C. Giovannella. *Relaxation in Complex Systems and Related Topics*. Vol. 222. Springer Science and Business Media, 2013.
- [2] H. M. Jaeger and S. R. Nagel. Physics of the granular state. *Science* **255**: (1992), 1523–1531.
- [3] A. Gurevich and H. Küpfer. Time scales of the flux creep in superconductors. *Phys. Rev. B* **48**: (1993), 6477.
- [4] K. Matan, R. B. Williams, T. A. Witten, and S. R. Nagel. Crumpling a thin sheet. *Phys. Rev. Lett.* **88**: (2002), 076101.
- [5] K. Büntemeyer, H. Lüthen, and M. Böttger. Auxin-induced changes in cell wall extensibility of maize roots. *Planta* **204**: (1998), 515–519.
- [6] O. Ben-David, S. M. Rubinstein, and J. Fineberg. Slip-stick and the evolution of frictional strength. *Nature* **463**: (2010), 76–79.
- [7] A. Amir, Y. Oreg, and Y. Imry. On relaxations and aging of various glasses. *Proc. Natl. Acad. Sci. USA* **109**: (2012), 1850–1855.
- [8] I. Iben et al. Glassy behavior of a protein. *Phys. Rev. Lett.* **62**: (1989), 1916–1919.
- [9] J. Phillips. Stretched exponential relaxation in molecular and electronic glasses. *Rep. Prog. Phys.* **59**: (1996), 1133.
- [10] Z. W. Wu, W. Kob, W.-H. Wang, and L. Xu. Stretched and compressed exponentials in the relaxation dynamics of a metallic glass-forming melt. *Nature Commun.* **9**: (2018), 1–7.
- [11] P. Philippe and D. Bideau. Compaction dynamics of a granular medium under vertical tapping. *Europhys. Lett.* **60**: (2002), 677.
- [12] E. B. Mpemba and D. G. Osborne. Cool? *Phys. Educ.* **4**: (1969), 172–175.
- [13] W. D. Ross. *Aristotle’s Metaphysics*. Clarendon Press, 1981.
- [14] M. Jeng. The Mpemba effect: When can hot water freeze faster than cold? *Am. J. Phys.* **74**: (2006), 514–522.
- [15] R. Bacon. *The Opus Majus of Roger Bacon*. Vol. 3. Williams and Norgate, 1900.
- [16] M. Clagett. *Giovanni Marliani and the Late Medieval Physics*. AMS Press, New York, 1967, 79.
- [17] F. Bacon. *Novum Organum*. Clarendon Press, 1878.
- [18] G. S. Kell. The freezing of hot and cold water. *Am. J. Phys.* **37**: (1969), 564–565.

- [19] M. Vynnycky and S. Mitchell. Evaporative cooling and the Mpemba effect. *Heat Mass Transfer* **46**: (2010), 881–890.
- [20] S. M. Mirabedin and F. Farhadi. Numerical investigation of solidification of single droplets with and without evaporation mechanism. *Int. J. Refrig.* **73**: (2017), 219–225.
- [21] M. Freeman. Cooler still-an answer? *Phys. Educ.* **14**: (1979), 417.
- [22] D. G. Osborne. Mind on ice. *Phys. Educ.* **14**: (1979), 414.
- [23] B. Wojciechowski, I. Owczarek, and G. Bednarz. Freezing of aqueous solutions containing gases. *Cryst. Res. Technol.* **23**: (1988), 843–848.
- [24] E. Deeson. Cooler-Lower Down. *Phys. Educ.* **6**: (1971), 42–44.
- [25] M. Vynnycky and S. Kimura. Can natural convection alone explain the Mpemba effect? *Int. J. Heat Mass Transfer* **80**: (2015), 243–255. ISSN: 0017-9310.
- [26] D. Auerbach. Supercooling and the Mpemba effect: When hot water freezes quicker than cold. *Am. J. Phys.* **63**: (1995), 882–885.
- [27] S. Esposito, R. De Risi, and L. Somma. Mpemba effect and phase transitions in the adiabatic cooling of water before freezing. *Phys. A Stat. Mech. Appl.* **387**: (2008), 757–763.
- [28] J. D. Brownridge. When does hot water freeze faster than cold water? A search for the Mpemba effect. *Am. J. Phys.* **79**: (2011), 78–84.
- [29] X. Zhang et al. Hydrogen-bond memory and water-skin supersolidity resolving the Mpemba paradox. *Phys. Chem. Chem. Phys.* **16**: (2014), 22995–23002.
- [30] X. Zhang et al. A common supersolid skin covering both water and ice. *Phys. Chem. Chem. Phys.* **16**: (2014), 22987–22994.
- [31] C. Q. Sun, X. Zhang, J. Zhou, Y. Huang, Y. Zhou, and W. Zheng. Density, elasticity, and stability anomalies of water molecules with fewer than four neighbors. *J. Phys. Chem. Lett.* **4**: (2013), 2565–2570.
- [32] C. Sun and Y. Sun. *The Attribute of Water: Single Notion, Multiple Myths*. Springer, 2016.
- [33] Y. Tao, W. Zou, J. Jia, W. Li, and D. Cremer. Different Ways of Hydrogen Bonding in Water—Why Does Warm Water Freeze Faster than Cold Water? *J. Chem. Theory Comput.* **13**: (2017), 55–76.
- [34] J. I. Katz. When hot water freezes before cold. *Am. J. Phys.* **77**: (2009), 27–29.
- [35] I. Firth. Cooler? *Phys. Educ.* **6**: (1971), 32–41.
- [36] P. Chaddah, S. Dash, K. Kumar, and A. Banerjee. Overtaking while approaching equilibrium. *arXiv:1011.3598* (2010).
- [37] P. M. Chaikin and T. C. Lubensky. *Principles of Condensed Matter Physics*. Cambridge University Press, 1995.
- [38] Y.-H. Ahn, H. Kang, D.-Y. Koh, and H. Lee. Experimental verifications of Mpemba-like behaviors of clathrate hydrates. *Korean J. Chem. Eng.* **33**: (2016), 1903–1907.
- [39] C. Hu et al. Conformation directed Mpemba effect on polylactide crystallization. *Cryst. Growth Des.* **18**: (2018), 5757–5762.

- [40] A. T. Lorenzo, M. L. Arnal, J. J. Sanchez, and A. J. Müller. Effect of annealing time on the self-nucleation behavior of semicrystalline polymers. *J. Polym. Sci. Part B: Polym. Phys.* **44**: (2006), 1738–1750.
- [41] H. C. Burridge and O. Hallstadius. Observing the Mpemba effect with minimal bias and the value of the Mpemba effect to scientific outreach and engagement. *Proc. R. Soc. A* **476**: (2020), 20190829.
- [42] P. A. Greaney, G. Lani, G. Cicero, and J. C. Grossman. Anomalous dissipation in single-walled carbon nanotube resonators. *Nano Lett.* **9**: (2009), 3699–3703.
- [43] A. Lasanta, F. V. Reyes, A. Prados, and A. Santos. When the hotter cools more quickly: Mpemba effect in granular fluids. *Phys. Rev. Lett.* **119**: (2017), 148001.
- [44] A. Torrente, M. A. López-Castaño, A. Lasanta, F. V. Reyes, A. Prados, and A. Santos. Large Mpemba-like effect in a gas of inelastic rough hard spheres. *Phys. Rev. E* **99**: (2019), 060901.
- [45] M. Baity-Jesi et al. The Mpemba effect in spin glasses is a persistent memory effect. *Proc. Natl. Acad. Sci. USA* **116**: (2019), 15350–15355.
- [46] A. Santos and A. Prados. Mpemba effect in molecular gases under nonlinear drag. *Phys. Fluids* **32**: (2020), 072010.
- [47] R. Gómez González, N. Khalil, and V. Garzó. Mpemba-like effect in driven binary mixtures. *arXiv:2010.14215* (2021).
- [48] S. Takada, H. Hayakawa, and A. Santos. Mpemba effect in inertial suspensions. *arXiv:2011.00812* (2020).
- [49] T. Keller, V. Torggler, S. B. Jäger, S. Schütz, H. Ritsch, and G. Morigi. Quenches across the self-organization transition in multimode cavities. *New J. Phys.* **20**: (2018), 025004.
- [50] A. Nava and M. Fabrizio. Lindblad dissipative dynamics in the presence of phase coexistence. *Phys. Rev. B* **100**: (2019), 125102.
- [51] A. Gijón, A. Lasanta, and E. Hernández. Paths towards equilibrium in molecular systems: the case of water. *Phys. Rev. E* **100**: (2019), 032103.
- [52] W. L. Jorgensen, J. Chandrasekhar, J. D. Madura, R. W. Impey, and M. L. Klein. Comparison of simple potential functions for simulating liquid water. *J. Chem. Phys.* **79**: (1983), 926–935.
- [53] K. C. Neuman, T. Lionnet, and J.-F. Allemand. Single-molecule micromanipulation techniques. *Annu. Rev. Mater. Res.* **37**: (2007), 33–67.
- [54] K. Dholakia and T. Čižmár. Shaping the future of manipulation. *Nat. Photonics* **5**: (2011), 335–342.
- [55] S. K. Mitra and S. Chakraborty. *Microfluidics and nanofluidics handbook: fabrication, implementation, and applications*. CRC Press, 2016.
- [56] J. Kepler. *De cometis libelli tres*. Augustae Vindelicorum: A. Apergerum, 1963.
- [57] J. H. Poynting. On the transfer of energy in the electromagnetic field. *Proc. R. Soc. Lond.* **36**: (1883), 186–187.
- [58] A. Ashkin. Acceleration and trapping of particles by radiation pressure. *Phys. Rev. Lett.* **24**: (1970), 156–159.

- [59] A. Ashkin, J. M. Dziedzic, J. Bjorkholm, and S. Chu. Observation of a single-beam gradient force optical trap for dielectric particles. *Opt. Lett.* **11**: (1986), 288–290.
- [60] S. Chu, J. Bjorkholm, A. Ashkin, and A. Cable. Experimental observation of optically trapped atoms. *Phys. Rev. Lett.* **57**: (1986), 314–317.
- [61] A. Ashkin and J. M. Dziedzic. Optical trapping and manipulation of viruses and bacteria. *Science* **235**: (1987), 1517–1520.
- [62] A. Ashkin, J. M. Dziedzic, and T. Yamane. Optical trapping and manipulation of single cells using infrared laser beams. *Nature* **330**: (1987), 769–771.
- [63] A. Ashkin and J. Dziedzic. Internal cell manipulation using infrared laser traps. *Proc. Natl. Acad. Sci. USA* **86**: (1989), 7914–7918.
- [64] S. Henderson, S. Mitchell, and P. Bartlett. Direct measurements of colloidal friction coefficients. *Phys. Rev. E* **64**: (2001), 061403.
- [65] J. Liphardt, S. Dumont, S. B. Smith, I. Tinoco, and C. Bustamante. Equilibrium information from nonequilibrium measurements in an experimental test of Jarzynski’s equality. *Science* **296**: (2002), 1832–1835.
- [66] G. Wang, E. M. Sevick, E. Mittag, D. J. Searles, and D. J. Evans. Experimental demonstration of violations of the second law of thermodynamics for small systems and short time scales. *Phys. Rev. Lett.* **89**: (2002), 050601.
- [67] A. Bérut, A. Arakelyan, A. Petrosyan, S. Ciliberto, R. Dillenschneider, and E. Lutz. Experimental verification of Landauer’s principle linking information and thermodynamics. *Nature* **483**: (2012), 187.
- [68] H. Yao, H. Ikeda, Y. Inoue, and N. Kitamura. Optical control of fusion of microparticles in solution and simultaneous spectrophotometric measurements. *Anal. Chem.* **68**: (1996), 4304–4307.
- [69] K. Ajito and K. Torimitsu. Single nanoparticle trapping using a Raman tweezers microscope. *Appl. Spectrosc* **56**: (2002), 541–544.
- [70] S. M. Block, L. S. Goldstein, and B. J. Schnapp. Bead movement by single kinesin molecules studied with optical tweezers. *Nature* **348**: (1990), 348–352.
- [71] M. D. Wang, H. Yin, R. Landick, J. Gelles, and S. M. Block. Stretching DNA with optical tweezers. *Biophys. J.* **72**: (1997), 1335–1346.
- [72] M. T. Woodside, P. C. Anthony, W. M. Behnke-Parks, K. Larizadeh, D. Herschlag, and S. M. Block. Direct measurement of the full, sequence-dependent folding landscape of a nucleic acid. *Science* **314**: (2006), 1001–1004.
- [73] M. Capitanio and F. S. Pavone. Interrogating biology with force: single molecule high-resolution measurements with optical tweezers. *Biophys. J.* **105**: (2013), 1293–1303.
- [74] M. Manosas, S. K. Perumal, V. Croquette, and S. J. Benkovic. Direct observation of stalled fork restart via fork regression in the T4 replication system. *Science* **338**: (2012), 1217–1220.
- [75] D. Min, K. Kim, C. Hyeon, Y. H. Cho, Y.-K. Shin, and T.-Y. Yoon. Mechanical unzipping and reziping of a single SNARE complex reveals hysteresis as a force-generating mechanism. *Nat. Commun.* **4**: (2013), 1–10.

- [76] R. J. Saphirstein et al. The focal adhesion: a regulated component of aortic stiffness. *PloS One* **8**: (2013), 62461.
- [77] F. Crick and A. Hughes. The physical properties of cytoplasm. *Exp. Cell Res.* **1**: (1950), 37–80.
- [78] S. B. Smith, L. Finzi, and C. Bustamante. Direct mechanical measurements of the elasticity of single DNA molecules by using magnetic beads. *Science* **258**: (1992), 1122–1126.
- [79] T. R. Strick, J.-F. Allemand, D. Bensimon, A. Bensimon, and V. Croquette. The elasticity of a single supercoiled DNA molecule. *Science* **271**: (1996), 1835–1837.
- [80] N. Ribeck and O. A. Saleh. Multiplexed single-molecule measurements with magnetic tweezers. *Rev. Sci. Instrum.* **79**: (2008), 094301.
- [81] I. De Vlaminck et al. Highly parallel magnetic tweezers by targeted DNA tethering. *Nano Lett.* **11**: (2011), 5489–5493.
- [82] A. Crut, D. A. Koster, R. Seidel, C. H. Wiggins, and N. H. Dekker. Fast dynamics of supercoiled DNA revealed by single-molecule experiments. *Proc. Natl. Acad. Sci. USA* **104**: (2007), 11957–11962.
- [83] I. De Vlaminck et al. Mechanism of homology recognition in DNA recombination from dual-molecule experiments. *Mol. Cell* **46**: (2012), 616–624.
- [84] H. You, R. Iino, R. Watanabe, and H. Noji. Winding single-molecule double-stranded DNA on a nanometer-sized reel. *Nucleic Acids Res.* **40**: (2012), e151–e151.
- [85] T. Ha. Single-molecule fluorescence resonance energy transfer. *Methods* **25**: (2001), 78–86.
- [86] T. Hugel et al. Experimental test of connector rotation during DNA packaging into bacteriophage ϕ 29 capsids. *PLoS Biol.* **5**: (2007), e59.
- [87] M. Lee, S. H. Kim, and S.-C. Hong. Minute negative superhelicity is sufficient to induce the BZ transition in the presence of low tension. *Proc. Nat. Acad. Sci. USA* **107**: (2010), 4985–4990.
- [88] J. S. Graham, R. C. Johnson, and J. F. Marko. Counting proteins bound to a single DNA molecule. *Biochem. Biophys. Res. Commun.* **415**: (2011), 131–134.
- [89] C. Gosse and V. Croquette. Magnetic tweezers: micromanipulation and force measurement at the molecular level. *Biophys. J.* **82**: (2002), 3314–3329.
- [90] K. C. Neuman and A. Nagy. Single-molecule force spectroscopy: optical tweezers, magnetic tweezers and atomic force microscopy. *Nature methods* **5**: (2008), 491–505.
- [91] E. R. Dufresne and D. G. Grier. Optical tweezer arrays and optical substrates created with diffractive optics. *Rev. Sci. Instrum.* **69**: (1998), 1974–1977.
- [92] E. R. Dufresne, G. C. Spalding, M. T. Dearing, S. A. Sheets, and D. G. Grier. Computer-generated holographic optical tweezer arrays. *Rev. Sci. Instrum.* **72**: (2001), 1810–1816.
- [93] D. G. Grier and Y. Roichman. Holographic optical trapping. *Appl. Opt.* **45**: (2006), 880–887.

- [94] G. Sinclair, P. Jordan, J. Courtial, M. Padgett, J. Cooper, and Z. J. Laczik. Assembly of 3-dimensional structures using programmable holographic optical tweezers. *Opt. Express* **12**: (2004), 5475–5480.
- [95] M. Reicherter, T. Haist, E. Wagemann, and H. J. Tiziani. Optical particle trapping with computer-generated holograms written on a liquid-crystal display. *Opt. Lett.* **24**: (1999), 608–610.
- [96] H. He, N. Heckenberg, and H. Rubinsztein-Dunlop. Optical particle trapping with higher-order doughnut beams produced using high efficiency computer generated holograms. *J. Mod. Opt.* **42**: (1995), 217–223.
- [97] P. Korda, G. C. Spalding, E. R. Dufresne, and D. G. Grier. Nanofabrication with holographic optical tweezers. *Rev. Sci. Instrum.* **73**: (2002), 1956–1957.
- [98] L. Lesem, P. Hirsch, and J. Jordan. The kinoform: a new wavefront reconstruction device. *IBM J. Res. Dev.* **13**: (1969), 150–155.
- [99] P. H. Jones, O. M. Maragò, and G. Volpe. *Optical tweezers: Principles and applications*. Cambridge University Press, 2015.
- [100] J. E. Curtis, B. A. Koss, and D. G. Grier. Dynamic holographic optical tweezers. *Opt. Commun.* **207**: (2002), 169–175.
- [101] G. R. Kirkham et al. Precision assembly of complex cellular microenvironments using holographic optical tweezers. *Sci. Rep.* **5**: (2015), 1–7.
- [102] Y. Roichman and D. G. Grier. Holographic assembly of quasicrystalline photonic heterostructures. *Opt. Express* **13**: (2005), 5434–5439.
- [103] D. Burnham and D. McGloin. Controlled aerosol manipulation using holographic optical tweezers. *Proc. SPIE* **6326**: (2006), 63261I.
- [104] N. Simpson, D. McGloin, K. Dholakia, L. Allen, and M. Padgett. Optical tweezers with increased axial trapping efficiency. *J. Mod. Opt.* **45**: (1998), 1943–1949.
- [105] C. Maurer, A. Jesacher, S. Fürhapter, S. Bernet, and M. Ritsch-Marte. Tailoring of arbitrary optical vector beams. *New J. Phys.* **9**: (2007), 78.
- [106] Y. Roichman and D. G. Grier. Projecting extended optical traps with shape-phase holography. *Opt. Lett.* **31**: (2006), 1675–1677.
- [107] G. T. Tietjen, Y. Kong, and R. Parthasarathy. An efficient method for the creation of tunable optical line traps via control of gradient and scattering forces. *Opt. Express* **16**: (2008), 10341–10348.
- [108] A. van der Horst and N. R. Forde. Calibration of dynamic holographic optical tweezers for force measurements on biomaterials. *Opt. Express* **16**: (2008), 20987–21003.
- [109] R. D. Hanes, M. C. Jenkins, and S. U. Egelhaaf. Combined holographic-mechanical optical tweezers: construction, optimization, and calibration. *Rev. Sci. Instrum.* **80**: (2009), 083703.
- [110] A. E. Cohen and W. E. Moerner. The anti-Brownian electrophoretic trap (ABEL trap): fabrication and software. *Imaging, Manipulation, and Analysis of Biomolecules and Cells: Fundamentals and Applications III*. Vol. 5699. International Society for Optics and Photonics. 2005, 296–305.

- [111] A. E. Cohen and W. E. Moerner. Method for trapping and manipulating nanoscale objects in solution. *Appl. Phys. Lett.* **86**: (2005), 093109.
- [112] R. Probst and B. Shapiro. Three-dimensional electrokinetic tweezing: device design, modeling, and control algorithms. *J. Micromech. Microeng.* **21**: (2011), 027004.
- [113] A. E. Cohen. “Trapping and manipulating single molecules in solution”. PhD thesis. Stanford University, 2006.
- [114] A. E. Cohen and W. Moerner. Suppressing Brownian motion of individual biomolecules in solution. *Proc. Natl. Acad. Sci. USA* **103**: (2006), 4362–4365.
- [115] A. P. Fields and A. E. Cohen. Electrokinetic trapping at the one nanometer limit. *Proc. Natl. Acad. Sci. USA* **108**: (2011), 8937–8942.
- [116] A. E. Cohen and W. Moerner. Controlling Brownian motion of single protein molecules and single fluorophores in aqueous buffer. *Opt. Express* **16**: (2008), 6941–6956.
- [117] A. E. Cohen. Control of nanoparticles with arbitrary two-dimensional force fields. *Phys. Rev. Lett.* **94**: (2005), 118102.
- [118] Y. Jun and J. Bechhoefer. Virtual potentials for feedback traps. *Phys. Rev. E* **86**: (2012), 061106.
- [119] Y. Jun, M. Gavrilov, and J. Bechhoefer. High-precision test of Landauer’s principle in a feedback trap. *Phys. Rev. Lett.* **113**: (2014), 190601.
- [120] R. Landauer. Irreversibility and heat generation in the computing process. *IBM J. Res. Dev.* **5**: (1961), 183–191.
- [121] J. K. King, B. K. Canfield, and L. M. Davis. Three-dimensional anti-Brownian electrokinetic trapping of a single nanoparticle in solution. *Appl. Phys. Lett.* **103**: (2013), 043102.
- [122] M. Kayci and A. Radenovic. Single florescent *[sic]* nanodiamond in a three dimensional ABEL trap. *Scientific reports* **5**: (2015), 16669.
- [123] M. Gavrilov, Y. Jun, and J. Bechhoefer. Real-time calibration of a feedback trap. *Rev. Sci. Instrum.* **85**: (2014), 095102.
- [124] V. Narayanamurthy, S. Nagarajan, F. Samsuri, T. Sridhar, et al. Microfluidic hydrodynamic trapping for single cell analysis: mechanisms, methods and applications. *Anal. Methods* **9**: (2017), 3751–3772.
- [125] W.-H. Tan and S. Takeuchi. A trap-and-release integrated microfluidic system for dynamic microarray applications. *Proc. Natl. Acad. Sci. USA* **104**: (2007), 1146–1151.
- [126] A. M. Skelley, O. Kirak, H. Suh, R. Jaenisch, and J. Voldman. Microfluidic control of cell pairing and fusion. *Nat. Methods* **6**: (2009), 147–152.
- [127] M. Tanyeri, E. M. Johnson-Chavarria, and C. M. Schroeder. Hydrodynamic trap for single particles and cells. *Appl. Phys. Lett.* **96**: (2010), 224101.
- [128] M. Tanyeri and C. M. Schroeder. Manipulation and confinement of single particles using fluid flow. *Nano Lett.* **13**: (2013), 2357–2364.
- [129] B. R. Lutz, J. Chen, and D. T. Schwartz. Hydrodynamic tweezers: 1. Noncontact trapping of single cells using steady streaming microeddies. *Anal. Chem.* **78**: (2006), 5429–5435.

- [130] E. M. Johnson-Chavarria, U. Agrawal, M. Tanyeri, T. E. Kuhlman, and C. M. Schroeder. Automated single cell microbio reactor for monitoring intracellular dynamics and cell growth in free solution. *Lab Chip* **14**: (2014), 2688–2697.
- [131] A. Lawrenz, F. Nason, and J. J. Cooper-White. Geometrical effects in microfluidic-based microarrays for rapid, efficient single-cell capture of mammalian stem cells and plant cells. *Biomicrofluidics* **6**: (2012), 024112.
- [132] A. A. Banaeiyan, D. Ahmadpour, C. B. Adiels, and M. Goksör. Hydrodynamic cell trapping for high throughput single-cell applications. *Micromachines* **4**: (2013), 414–430.
- [133] X. Xu, Z. Li, N. Kotagiri, P. Sarder, S. Achilefu, and A. Nehorai. Microfluidic microsphere-trap arrays for simultaneous detection of multiple targets. *Microfluidics, BioMEMS, and Medical Microsystems XI*. Vol. 8615. International Society for Optics and Photonics. 2013, 86151E.
- [134] J. Kim, J. Erath, A. Rodriguez, and C. Yang. A high-efficiency microfluidic device for size-selective trapping and sorting. *Lab Chip* **14**: (2014), 2480–2490.
- [135] D. Di Carlo, L. Y. Wu, and L. P. Lee. Dynamic single cell culture array. *Lab Chip* **6**: (2006), 1445–1449.
- [136] H. Chen, J. Sun, E. Wolvetang, and J. Cooper-White. High-throughput, deterministic single cell trapping and long-term clonal cell culture in microfluidic devices. *Lab Chip* **15**: (2015), 1072–1083.
- [137] J. Ryley and O. M. Pereira-Smith. Microfluidics device for single cell gene expression analysis in *Saccharomyces cerevisiae*. *Yeast* **23**: (2006), 1065–1073.
- [138] D. Wlodkowic, S. Faley, M. Zagnoni, J. P. Wikswo, and J. M. Cooper. Microfluidic single-cell array cytometry for the analysis of tumor apoptosis. *Anal. Chem.* **81**: (2009), 5517–5523.
- [139] T. Arakawa, M. Noguchi, K. Sumitomo, Y. Yamaguchi, and S. Shoji. High-throughput single-cell manipulation system for a large number of target cells. *Biomicrofluidics* **5**: (2011), 014114.
- [140] L. L. Bell, A. A. Seshia, E. D. Laue, and D. Lando. A microfluidic device for high density hydrodynamic cell trapping, growth and Super-Resolution imaging. *SENSORS*. IEEE. 2011, 304–307.
- [141] Y. Zhou et al. A microfluidic platform for trapping, releasing and super-resolution imaging of single cells. *Sens. Actuators B: Chem.* **232**: (2016), 680–691.
- [142] J. Friend and L. Y. Yeo. Microscale acoustofluidics: Microfluidics driven via acoustics and ultrasonics. *Rev. Mod. Phys.* **83**: (2011), 647.
- [143] J. Wu. Acoustical tweezers. *J. Acoust. Soc. Am.* **89**: (1991), 2140–2143.
- [144] A. Ozcelik et al. Acoustic tweezers for the life sciences. *Nat. Methods* **15**: (2018), 1021–1028.
- [145] L. Meng, F. Cai, F. Li, W. Zhou, L. Niu, and H. Zheng. Acoustic tweezers. *J. Phys. D: Appl. Phys.* **52**: (2019), 273001.
- [146] J. Shi, D. Ahmed, X. Mao, S.-C. S. Lin, A. Lawit, and T. J. Huang. Acoustic tweezers: patterning cells and microparticles using standing surface acoustic waves (SSAW). *Lab Chip* **9**: (2009), 2890–2895.

- [147] Y. Chen et al. Standing surface acoustic wave (SSAW)-based microfluidic cytometer. *Lab Chip* **14**: (2014), 916–923.
- [148] D. Baresch, J.-L. Thomas, and R. Marchiano. Observation of a single-beam gradient force acoustical trap for elastic particles: acoustical tweezers. *Phys. Rev. Lett.* **116**: (2016), 024301.
- [149] K. Melde, A. G. Mark, T. Qiu, and P. Fischer. Holograms for acoustics. *Nature* **537**: (2016), 518–522.
- [150] L. P. Gor’kov. On the forces acting on a small particle in an acoustical field in an ideal fluid. *Sov. Phys. Dokl.* **6**: (1962), 773–775.
- [151] S. Sadhal. Acoustofluidics 16: acoustics streaming near liquid–gas interfaces: drops and bubbles. *Lab Chip* **12**: (2012), 2771–2781.
- [152] S. Sadhal. Acoustofluidics 13: Analysis of acoustic streaming by perturbation methods. *Lab Chip* **12**: (2012), 2292–2300.
- [153] D. Ahmed et al. Rotational manipulation of single cells and organisms using acoustic waves. *Nat. Commun.* **7**: (2016), 1–11.
- [154] M. Saito, T. Daian, K. Hayashi, and S.-y. Izumida. Fabrication of a polymer composite with periodic structure by the use of ultrasonic waves. *J. Appl. Phys.* **83**: (1998), 3490–3494.
- [155] O. Manneberg, B. Vanherberghen, B. Önfelt, and M. Wiklund. Flow-free transport of cells in microchannels by frequency-modulated ultrasound. *Lab Chip* **9**: (2009), 833–837.
- [156] G. Simon et al. Particle separation in surface acoustic wave microfluidic devices using reprogrammable, pseudo-standing waves. *Appl. Phys. Lett.* **113**: (2018), 044101.
- [157] G. Destgeer, K. H. Lee, J. H. Jung, A. Alazzam, and H. J. Sung. Continuous separation of particles in a PDMS microfluidic channel via travelling surface acoustic waves (TSAW). *Lab Chip* **13**: (2013), 4210–4216.
- [158] G. Destgeer, B. H. Ha, J. H. Jung, and H. J. Sung. Submicron separation of microspheres via travelling surface acoustic waves. *Lab Chip* **14**: (2014), 4665–4672.
- [159] J. D. Adams, P. Thévoz, H. Bruus, and H. T. Soh. Integrated acoustic and magnetic separation in microfluidic channels. *Appl. Phys. Lett.* **95**: (2009), 254103.
- [160] G. Thalhammer, R. Steiger, M. Meinschad, M. Hill, S. Bernet, and M. Ritsch-Marte. Combined acoustic and optical trapping. *Biomed. Opt. Express* **2**: (2011), 2859–2870.
- [161] S. H. Kim, M. Antfolk, M. Kobayashi, S. Kaneda, T. Laurell, and T. Fujii. Highly efficient single cell arraying by integrating acoustophoretic cell pre-concentration and dielectrophoretic cell trapping. *Lab Chip* **15**: (2015), 4356–4363.
- [162] Y. Liu, D. Cheng, G. Sonek, M. Berns, C. Chapman, and B. Tromberg. Evidence for localized cell heating induced by infrared optical tweezers. *Biophys. J.* **68**: (1995), 2137–2144.
- [163] P. M. Celliers and J. Conia. Measurement of localized heating in the focus of an optical trap. *Appl. Opt.* **39**: (2000), 3396–3407.
- [164] B. Del Rosal et al. Heat in optical tweezers. *Optical Trapping and Optical Micro-manipulation X*. Vol. 8810. International Society for Optics and Photonics. 2013, 88102A.

- [165] E. J. Peterman, F. Gittes, and C. F. Schmidt. Laser-induced heating in optical traps. *Biophys. J.* **84**: (2003), 1308–1316.
- [166] L. Lin et al. Opto-thermoelectric nanotweezers. *Nat. Photonics* **12**: (2018), 195–201.
- [167] L. Lin et al. Light-directed reversible assembly of plasmonic nanoparticles using plasmon-enhanced thermophoresis. *ACS Nano* **10**: (2016), 9659–9668.
- [168] J. Zenteno-Hernandez, J. V. Lozano, J. Sarabia-Alonso, J. Ramírez-Ramírez, and R. Ramos-García. Optical trapping in the presence of laser-induced thermal effects. *Opt. Lett.* **45**: (2020), 3961–3964.
- [169] M.-C. Zhong, A.-Y. Liu, and F. Ji. Opto-thermal oscillation and trapping of light absorbing particles. *Opt. Express* **27**: (2019), 29730–29737.
- [170] K. Berg-Sørensen and H. Flyvbjerg. Power spectrum analysis for optical tweezers. *Rev. Sci. Instrum.* **75**: (2004), 594–612.
- [171] K. Visscher, G. Brakenhoff, and J. Krol. Micromanipulation by “multiple” optical traps created by a single fast scanning trap integrated with the bilateral confocal scanning laser microscope. *Cytometry A* **14**: (1993), 105–114.
- [172] R. Brown. XXVII. A brief account of microscopical observations made in the months of June, July and August 1827, on the particles contained in the pollen of plants; and on the general existence of active molecules in organic and inorganic bodies. *Philos. Mag.* **4**: (1828), 161–173.
- [173] A. Einstein. On the motion of small particles suspended in liquids at rest required by the molecular-kinetic theory of heat. *Ann. Phys.* **17**:549-560 (1905), 208.
- [174] D. S. Lemons and A. Gythiel. Paul Langevin’s 1908 paper “On the theory of Brownian motion” [“Sur la théorie du mouvement brownien,” C. R. Acad. Sci.(Paris) 146, 530–533 (1908)]. *Am. J. Phys.* **65**: (1997), 1079–1081.
- [175] A. D. Fokker. The mean energy of rotating electrical dipoles in the radiation field. *Ann. Phys.* **348**: (1914), 810–820.
- [176] M. Planck. About a theorem of statistical dynamics and its extension in quantum theory session. *Preuss. Akad. Wiss* **24**: (1917).
- [177] G. E. Uhlenbeck and L. S. Ornstein. On the theory of the Brownian motion. *Phys. Rev.* **36**: (1930), 823.
- [178] R. Kubo. The fluctuation-dissipation theorem. *Rep. Prog. Phys.* **29**: (1966), 255.
- [179] P. Langevin. CR Acad. Sci.(Paris) 146, 530; trans. Lemons, DS and Gythiel, A.(1997). *Am. J. Phys.* **65**: (1908), 1079–1081.
- [180] N. G. van Kampen. *Stochastic Processes in Physics and Chemistry*. 3rd edn. Elsevier, 2007.
- [181] M. C. Wang and G. E. Uhlenbeck. On the theory of the Brownian motion II. *Rev. Mod. Phys.* **17**: (1945), 323–342.
- [182] K. Svoboda and S. M. Block. Biological applications of optical forces. *Annu. Rev. Biophys. Biomol. Struct.* **23**: (1994), 247–285.
- [183] H. Risken. *The Fokker-Planck Equation: Methods of Solution and Applications*. 2nd edn. Springer, 1989.

- [184] M. Stone and P. Goldbart. *Mathematics for Physics: A Guided Tour for Graduate Students*. Cambridge University Press, 2009.
- [185] D. V. Widder. *The Heat Equation*. Vol. 67. Academic Press, 1976.
- [186] Z. Lu and O. Raz. Nonequilibrium thermodynamics of the Markovian Mpemba effect and its inverse. *Proc. Natl. Acad. Sci. USA* **114**: (2017), 5083–5088.
- [187] H. J. Weber and G. B. Arfken. *Essential Mathematical Methods for Physicists*. Elsevier Academic Press, 2003.
- [188] P. Jones, O. Maragó, and G. Volpe. *Optical Tweezers: Principles and Applications*. Cambridge Univ. Press, 2015.
- [189] Y. Z. Shi et al. Sculpting nanoparticle dynamics for single-bacteria-level screening and direct binding-efficiency measurement. *Nat. Commun.* **9**: (2018), 815.
- [190] Y. Shi et al. Nanometer-precision linear sorting with synchronized optofluidic dual barriers. *Sci. Adv.* **4**: (2018), 773.
- [191] M. Righini, A. S. Zelenina, C. Girard, and R. Quidant. Parallel and selective trapping in a patterned plasmonic landscape. *Nat. Phys.* **3**: (2007), 477.
- [192] D. Gao et al. Optical manipulation from the microscale to the nanoscale: fundamentals, advances and prospects. *Light Sci. Appl* **6**: (2017), 17039.
- [193] M. D. Armani, S. V. Chaudhary, R. Probst, and B. Shapiro. Using feedback control of microflows to independently steer multiple particles. *J. Microelectromech. S.* **15**: (2006), 945–956.
- [194] Q. Wang and W. E. Moerner. An adaptive anti-Brownian electrokinetic trap with real-time information on single-molecule diffusivity and mobility. *ACS Nano* **5**: (2011), 5792–5799.
- [195] A. E. Cohen. Control of nanoparticles with arbitrary two-dimensional force fields. *Phys. Rev. Lett.* **94**: (2005), 118102.
- [196] M. Gavrilov and J. Bechhoefer. Erasure without work in an asymmetric double-well potential. *Phys. Rev. Lett.* **117**: (2016), 200601.
- [197] M. Gavrilov, R. Chétrite, and J. Bechhoefer. Direct measurement of nonequilibrium system entropy is consistent with Gibbs-Shannon form. *Proc. Natl. Acad. Sci. USA* **114**: (2017), 11097–11102.
- [198] R. M. Simmons, J. T. Finer, S. Chu, and J. A. Spudich. Quantitative measurements of force and displacement using an optical trap. *Biophys. J.* **70**: (1996), 1813–1822.
- [199] A. Ranaweera and B. Bamieh. Modelling, identification, and control of a spherical particle trapped in an optical tweezer. *Int. J. Robust Nonlin.* **15**: (2005), 747–768.
- [200] A. E. Wallin, H. Ojala, E. Hægström, and R. Tuma. Stiffer optical tweezers through real-time feedback control. *App. Phys. Lett.* **92**: (2008), 224104.
- [201] J. A. Albay, G. Paneru, H. K. Pak, and Y. Jun. Optical tweezers as a mathematically driven spatio-temporal potential generator. *Opt. Express* **26**: (2018), 29906–29915.
- [202] A. Kumar and J. Bechhoefer. Optical feedback tweezers. *Proc. SPIE* **10723**: (2018).
- [203] A. Kumar and J. Bechhoefer. Nanoscale virtual potentials using optical tweezers. *Appl. Phys. Lett.* **113**: (2018), 183702.

- [204] A. Kumar and J. Bechhoefer. Shaping arbitrary energy landscapes with feedback. *Phys. in Canada* **75**: (2019).
- [205] A. Ashkin. Forces of a single-beam gradient laser trap on a dielectric sphere in the ray optics regime. *Biophys. J.* **61**: (1992), 569–582.
- [206] Y. Harada and T. Asakura. Radiation forces on a dielectric sphere in the Rayleigh scattering regime. *Opt. Commun.* **124**: (1996), 529–541.
- [207] A. B. Stilgoe, T. A. Nieminen, G. Knöner, N. R. Heckenberg, and H. Rubinsztein-Dunlop. The effect of Mie resonances on trapping in optical tweezers. *Opt. Express* **16**: (2008), 15039–15051.
- [208] G. Gouesbet, G. Gréhan, and B. Maheu. Scattering of a Gaussian beam by a Mie scatter center using a Bromwich formalism. *J. Optics* **16**: (1985), 83.
- [209] G. Gouesbet, B. Maheu, and G. Gréhan. Light scattering from a sphere arbitrarily located in a Gaussian beam, using a Bromwich formulation. *J. Opt. Soc. Am. A* **5**: (1988), 1427–1443.
- [210] B. Maheu, G. Gouesbet, and G. Gréhan. A concise presentation of the generalized Lorenz-Mie theory for arbitrary location of the scatterer in an arbitrary incident profile. *J. Optics* **19**: (1988), 59.
- [211] T. A. Nieminen et al. Optical tweezers computational toolbox. *J. Opt. A: Pure Appl. Opt.* **9**: (2007), S196.
- [212] T. A. Nieminen, H. Rubinsztein-Dunlop, N. R. Heckenberg, and A. Bishop. Numerical modelling of optical trapping. *Comp. Phys. Commun.* **142**: (2001), 468–471.
- [213] S. Perrone, G. Volpe, and D. Petrov. 10-fold detection range increase in quadrant-photodiode position sensing for photonic force microscope. *Rev. Sci. Instrum.* **79**: (2008), 106101.
- [214] I. A. Martínez and D. Petrov. Back-focal-plane position detection with extended linear range for photonic force microscopy. *Appl. Opt.* **51**: (2012), 5973–5977.
- [215] F. Gittes and C. F. Schmidt. Interference model for back-focal-plane displacement detection in optical tweezers. *Opt. Lett.* **23**: (1998), 7–9.
- [216] F. L. Pedrotti, L. M. Pedrotti, and L. S. Pedrotti. *Introduction to optics*. Cambridge University Press, 2017.
- [217] N. A. Loiko and A. Samson. Nonlinear dynamics of laser systems with a delay. *Quantum Electronics* **24**: (1994), 657.
- [218] F. Isnin, M. K. Abdullah, V. Sinivasagam, Teyo Tuan Chin, and H. B. Ahmad. Back reflection and pump instability effects on a fiber laser system. *ICSE'98. 1998 IEEE International Conference on Semiconductor Electronics. Proceedings (Cat. No.98EX187)*. 1998, 112–116.
- [219] K. C. Neuman and S. M. Block. Optical trapping. *Rev. Sci. Instrum.* **75**: (2004), 2787–2809.
- [220] M. S. Woody, M. Capitanio, E. M. Ostap, and Y. E. Goldman. Electro-optic deflectors deliver advantages over acousto-optical deflectors in a high resolution, ultra-fast force-clamp optical trap. *Opt. Express* **26**: (2018), 11181–11193.

- [221] M. T. Valentine, N. R. Gwydosh, B. Gutiérrez-Medina, A. N. Fehr, J. O. Andreasson, and S. M. Block. Precision steering of an optical trap by electro-optic deflection. *Opt. Lett.* **33**: (2008), 599–601.
- [222] N. Kehtarnavaz and S. Mahotra. *Digital Signal Processing Laboratory: LabVIEW-Based FPGA Implementation*. Universal-Publishers, 2010.
- [223] S. Kilts. *Advanced FPGA Design: Architecture, Implementation, and Optimization*. John Wiley & Sons, 2007.
- [224] P. Ponce-Cruz, A. Molina, and B. MacCleery. *Fuzzy Logic Type 1 and Type 2 Based on LabVIEW™ FPGA*. Springer, 2016.
- [225] S. F. Nørrelykke and H. Flyvbjerg. Power spectrum analysis with least-squares fitting: amplitude bias and its elimination, with application to optical tweezers and atomic force microscope cantilevers. *Rev. Sci. Instrum.* **81**: (2010), 075103.
- [226] L. Boltzmann. *Lectures on Gas Theory*. University of California Press, Berkeley, 1964. Translation of *Vorlesungen über Gastheorie* by Stephen G. Brush.
- [227] K. Visscher and S. M. Block. Versatile optical traps with feedback control. *Methods Enzymol.* **298**: (1998), 460–489.
- [228] S. F. Tolić-Nørrelykke, E. Schäffer, J. Howard, F. S. Pavone, F. Jülicher, and H. Flyvbjerg. Calibration of optical tweezers with positional detection in the back focal plane. *Rev. Sci. Instrum.* **77**: (2006), 103101.
- [229] L. D. Landau and E. M. Lifshitz. *Fluid Mechanics*. 2nd edn. Pergamon, 1987.
- [230] H. Faxén. The motion of a rigid ball along the axis of a pipe filled with viscous liquid. *Arkiv for Matematik Astronomi och Fysik* **17**: (1923), 1–28.
- [231] Y. Jun and J. Bechhoefer. Virtual potentials for feedback traps. *Phys. Rev. E* **86**: (2012), 061106.
- [232] P. Hänggi. Reaction-rate theory: fifty years after Kramers. *Rev. Mod. Phys.* **62**: (1990), 251–341.
- [233] J. K. Dreyer, K. Berg-Sørensen, and L. Oddershede. Improved axial position detection in optical tweezers measurements. *Appl. Opt.* **43**: (2004), 1991–1995.
- [234] C. Deufel and M. D. Wang. Detection of forces and displacements along the axial direction in an optical trap. *Biophys. J* **90**: (2006), 657–667.
- [235] Y. Shechtman, S. J. Sahl, A. S. Back, and W. E. Moerner. Optimal point spread function design for 3D imaging. *Phys. Rev. Lett.* **113**: (2014), 133902.
- [236] K. Neupane, A. P. Manuel, and M. T. Woodside. Protein folding trajectories can be described quantitatively by one-dimensional diffusion over measured energy landscapes. *Nat. Physics* **12**: (2016), 700–704.
- [237] W. E. Thomas, E. Trintchina, M. Forero, V. Vogel, and E. V. Sokurenko. Bacterial adhesion to target cells enhanced by shear force. *Cell* **109**: (2002), 913–923.
- [238] G. Young et al. Quantitative mass imaging of single biological macromolecules. *Science* **360**: (2018), 423–427.
- [239] A. H. Squires, A. A. Lavania, P. D. Dahlberg, and W. Moerner. Interferometric scattering enables fluorescence-free electrokinetic trapping of single nanoparticles in free solution. *Nano Lett.* **19**: (2019), 4112–4117.

- [240] E. Aurell, K. Gawedzki, C. Mejía-Monasterio, R. Mohayaee, and P. Muratore-Ginanneschi. Refined second law of thermodynamics for fast random processes. *J. Stat. Phys* **147**: (2012), 487–505.
- [241] P. R. Zulkowski and M. R. DeWeese. Optimal finite-time erasure of a classical bit. *Phys. Rev. E* **89**: (2014), 052140.
- [242] H. C. Burridge and P. F. Linden. Questioning the Mpemba effect: hot water does not cool more quickly than cold. *Sci. Rep.* **6**: (2016), 37665.
- [243] J. I. Katz. Reply to Burridge and Linden: Hot water may freeze sooner than cold. *arXiv:1701.03219* (2017).
- [244] A. Kumar and J. Bechhoefer. Exponentially faster cooling in a colloidal system. *Nature* **584**: (2020), 64–68.
- [245] R. Chétrite, A. Kumar, and J. Bechhoefer. The Metastable Mpemba Effect Corresponds to a Non-monotonic Temperature Dependence of Extractable Work. *Front. Phys.* **9**: (2021), 141.
- [246] L. Zhang. “Cooling dynamics of a Brownian particle and the Markovian Mpemba effect”. MA thesis. Simon Fraser Univ., 2019.
- [247] W. H. Press, B. P. Flannery, S. A. Teukolsky, and W. T. Vetterling. *Numerical Recipes: The Art of Scientific Computing*. 3rd edn. Cambridge, UK: Cambridge Univ. Press, 2007.
- [248] J. L. Lebowitz and P. G. Bergmann. Irreversible Gibbsian ensembles. *Ann. Phys.* **1**: (1957), 1–23.
- [249] J. G. Skellam. The frequency distribution of the difference between two Poisson variates belonging to different populations. *J. R. Stat. Soc. A* **109**: (1946), 296–296.
- [250] T. Cover and J. Thomas. *Elements of Information Theory*. 2nd edn. New York: John Wiley & Sons, Inc., 2006.
- [251] N. Shiraishi and K. Saito. Information-theoretical bound of the irreversibility in thermal relaxation processes. *Phys. Rev. Lett.* **123**:11 (2019), 110603.
- [252] E. T. Jaynes. *Probability Theory: The Logic of Science*. Cambridge University Press, 2003.
- [253] I. Klich, O. Raz, O. Hirschberg, and M. Vucelja. Mpemba index and anomalous relaxation. *Phys. Rev. X* **9**: (2019), 021060.
- [254] C. W. Gardiner. *Stochastic Methods: A Handbook for the Natural and Social Sciences*. 4th edn. Springer, 2009.
- [255] H. A. Kramers. Brownian motion in a field of force and the diffusion model of chemical reactions. *Physica A* **7**: (1940), 284–304.
- [256] N. Berglund. Kramers’ law: Validity, derivations and generalisations. *Markov Processes Relat. Fields* **19**: (2013), 459–490.
- [257] J. M. R. Parrondo, J. M. Horowitz, and T. Sagawa. Thermodynamics of information. *Nature Phys.* **11**: (2015), 131–139.
- [258] R. Shaw. *The Dripping Faucet as a Model Chaotic System*. Aerial Press, 1984.

- [259] J. G. Leidenfrost. *De Aquae Communis Nonnullis Qualitatibus Tractatus*. Ovenius, 1756. English translation, A Tract About Some Qualities of Common Water by C. Wares in *Int. J. Heat Mass Transfer* **9**: (1966), 1153.
- [260] S. Nukiyama. The maximum and minimum values of the heat Q transmitted from metal to boiling water under atmospheric pressure. *Int. J. Heat Mass Transfer* **9**: (1966), 1419–1433. Translation from S.Nukiyama. *J. Soc. Mech. Eng. Japan* **31**: (1934), 361.
- [261] J. G. Walker. *Boiling and the Leidenfrost Effect*. In *Fundamentals of Physics* by D. Halliday and R. Resnick (Wiley, New York, 1988, 3rd edn.), E10–1-5.
- [262] J. Bernardin and I. Mudawar. The Leidenfrost point: experimental study and assessment of existing models. *J. Heat Transfer* **121**: (1999), 894–903.
- [263] A. Kumar, R. Chétrite, and J. Bechhoefer. Anomalous heating in a colloidal system. *arXiv:2104.12899* (2021).
- [264] J. Elliott and P. Dawber. *Symmetry in Physics: Principles and Simple Applications*. Vol. 222. Macmillan, 1979.
- [265] M. Vynnycky and N. Maeno. Axisymmetric natural convection-driven evaporation of hot water and the Mpemba effect. *Int. J. Heat Mass Transfer* **55**: (2012), 7297–7311.
- [266] J. Jin and W. A. Goddard III. Mechanisms underlying the Mpemba effect in water from molecular dynamics simulations. *J. Phys. Chem. C* **119**: (2015), 2622–2629.
- [267] N. Goldenfeld. *Lectures on Phase Transitions and the Renormalization Group*. Addison-Wesley, 1992.
- [268] P. G. Debenedetti. *Metastable Liquids: Concepts and Principles*. Princeton Univ. Press, 1997.
- [269] A. L. Moore and L. Shi. Emerging challenges and materials for thermal management of electronics. *Mat. Today* **17**: (2014), 163–174.
- [270] A. Gal and O. Raz. Precooling strategy allows exponentially faster heating. *Phys. Rev. Lett.* **124**: (2020).
- [271] P. Ball. Does hot water freeze first? *Phys. World* **19**: (2006), 19.